A NUMERICAL INVESTIGATION OF TURBULENCE-DRIVEN AND FORCED GENERATION OF INTERNAL GRAVITY WAVES IN STRATIFIED MID-WATER

A Dissertation

Presented to the Faculty of the Graduate School

of Cornell University

in Partial Fulfillment of the Requirements for the Degree of

Doctor of Philosophy

by

Ammar Mohammed Abdilghanie

January 2011

A NUMERICAL INVESTIGATION OF TURBULENCE-DRIVEN AND FORCED GENERATION OF INTERNAL GRAVITY WAVES IN STRATIFIED MID-WATER

Ammar Mohammed Abdilghanie, Ph.D.

Cornell University 2011

Natural and externally-forced excitation of internal gravity waves in a uniformly stratified fluid have been thoroughly investigated by means of highly resolved large eddy simulations. The first part of the thesis focuses on the generation of high frequency internal gravity waves by the turbulent wake of a towed sphere in a uniformly stratified fluid. We have used continuous wavelet transforms to quantify relevant wavelength and frequencies and their spatial and temporal dependence in the near field of the wake. The dependence on Reynolds number and Froude number of the internal wave field wavelengths, frequencies and isopycnal displacements are reported for the first time. The initial wavelengths and decay rates show a dependence on both parameters that can not be explained on the basis of impulsive mass source models. The results also clearly identify Reynolds number as the main driver for the observed selection of a narrow range of wave phase- line-tilt-angles and shed some light on the coupling of the waves and turbulent wake region at high Reynolds number. Finally, the potential for nonlinear interactions, instability and breaking of the waves increases with both Reynolds and Froude numbers. The results of this part of the thesis motivate future theoretical investigations into the underlying generation mechanisms and improved parametrization of the role of small scale processes, such as high frequency internal gravity waves, in large scale circulation models in the ocean and atmosphere.

In the second half of the thesis, we have focused on the generation of an internal gravity wavepacket by a vertically localized transient forcing. We have found that the unique combination of strong vertical localization and large wave amplitude, typically not considered in the literature, lead to the formation of strong horizontal mean flow inside the wave forcing region that nonlinearly grows at the expense of a depleted and structurally modified emerging internal wave packet. A novel theoretical analysis is developed which can explain the underlying mechanism for the formation of the mean flow. By appealing to scaling arguments, based on a one way wave-mean flow interaction, we quantify the mean flow dependence on the input parameters. By means of a phase averaging procedure, we offer additional insight on mean flow reduction through horizontal localization of a wavepacket. Finally, mean flow containment techniques that allow the generation of a well-defined wavepacket that preserves its structure near the source and during the propagation towards a remote interaction region are proposed and tested. The efficiency of the techniques is tested in a simulation of internal gravity wave-shear flow interaction near a critical level. The simulations qualitatively agree with previous numerical investigations of such flow.

BIOGRAPHICAL SKETCH

Ammar Abdilghanie received his BSc (2000) and MSc (2004) from the department of Mechanical Power Engineering at Cairo University, Giza, Egypt. In August 2004 he joined the department of Aerospace Engineering at the University of Michigan at Ann Arbor, USA, where he worked under the supervision of the late Professor Gerard Faeth on the dynamics of chemically passive fire suppressants in normal and reduced gravity environments. In December of 2005 he graduated with a ME degree and shortly thereafter joined the Sibley School of Mechanical and Aerospace Engineering at Cornell University for doctoral studies in fluid mechanics. He has been working under the supervision of Prof. Peter Diamessis on understanding the intriguing dynamics of stratified fluids through highly accurate numerical simulations. He obtained a minor in computational science and engineering working under the supervision of Prof. David Caughey and Prof. Lance Collins on the the comparison of turbulence modelling techniques for the simulation of indoor flows. He took a big joy in working in such intellectually stimulating and open-minded learning environments. He is looking forward to join the University of Washington as a post doctoral research associate working under the supervision of Prof. James Riley on Petascale simulations of the atmospheric boundary layer and turbulent reactive flows.

On Giving

You give but little when you give of your possessions.

It is when you give of yourself that you truly give.

There are those who give with joy, and that joy is their reward.

And there are those who give with pain, and that pain is their baptism.

And there are those who give and know not pain in giving, nor do they seek joy, nor give with mindfulness of virtue;

They give as in yonder valley the myrtle breathes its fragrance into space.

Through the hands of such as these God speaks, and from behind their eyes He smiles upon the earth.

Gibran, *The Prophet*

To my Wife, my Son, my Mother

and in memory of my Dad

ACKNOWLEDGEMENTS

It is a pleasure to thank those who made this thesis possible. First and foremost, I would like to thank my supervisor, Prof. Peter Diamessis, whose encouragement, guidance, patience and support from the initial to the final level has been the key driver for my success throughout the formidable Ph.D. program at Cornell University. He has made available his support in a number of ways. His expertise and profound physical understanding of stratified turbulent flows and computational fluid mechanics has significantly impacted my own understanding and prepared me to tackle even more challenging problems in the future. He has also helped me overcome daily anxiety when I first embarked on research in stratified flows. He spared no effort, energy or time in serving as a thesis advisor, a coach, a counselor, and above all a close friend with a common Mediterranean heritage. I thoroughly enjoyed and benefited from all the teaching, advice, encouragement and admonishment.

I am also honored to have prof. David Caughey and Lance Collins serve on my thesis committee and to get the opportunity to work under their supervision on my minor project in computational science and engineering. I can not thank them enough for all their help and for significantly improving my understanding of the physics and numerical simulation of indoor air flows. I am grateful to both of them for teaching me how to think about, extract, and understand the statistics of turbulent flows and how to connect the statistics to the evolution and dynamics of the underlying flow.

I like to devote a special thank you to Prof. Geoff. Spedding at USC for generously taking time to respond to my many lengthy and often unclear emails about the wavelet transforms and their applications in fluid mechanics and for

giving me the privilege to use his wavelet codes. The rigor and precision of his responses have inspired me to emulate him in my own scientific communication. I also like to thank Prof. Bruce Sutherland at U-Alberta, Prof. James Rottman at UCSD, Prof. Kraig Winters at UCSD, Prof. Larry Redekopp at USC, Prof. Donald Slinn at UFL, and Prof. Edwin Cowen at Cornell University for many useful suggestions and comments about the forcing-generated internal waves.

I would also like to acknowledge the financial support of the Office of Naval Research through grant N00014-08-1-0235 administered by Dr. Ronald Joslin.

I have been blessed with wonderful professors, colleagues and friends at Michigan and Cornell who provided a lot of support at so many levels. From the U of M, I would like to thank Prof. Wei Shyy, Prof. Werner Dahm, Prof. James Driscoll, Prof. Luis Bernal, Prof. Ian Boyd, Prof. Van Leer, and Prof. Elaine Oran, for their great shoulders. They have offered tremendous help, compassion and support during the difficult time of the passing of my advisor; Prof. Gerard Faeth. Also from the U of M, I would like to thank Dr. Khaled Sallam, Mohamed Shalaby, Karim Hamza, Omer Baghdady, Hatem Orban, Mohamed Tanani, Alaa Matar, Ayman Khafagy, Mohamed Elgendy, Ramy El-rubi, Binoy Philip, Shreyas Sirsi, Ajdin Kavara, Omer Abdo, Ihab Ismail, Farzad Ismail, and Bill Hall for being such wonderful companions during my M.ENG.

My Ph.D. at Cornell University would have been very difficult without the smiles, laughs, lunches (and ice creams!) I shared with Jorge Escobar, Alexandra King, Yong Sung Park, Blair Johnson, Erika Johnson, Paul Richter, Seth Schweitzer, Rafael Tinoco, Peter Rusello, Chen Pey, Chan I Chi, Themistoklis Stefanakis, Mike Schwendeman, Atif Chaudhry, Juan Salazar, Juan Isaza, Raju

Kusumanchi, Shi Jin, Yang Liu, Yanjun Xia, David Korda, and Ray Baidurja.

This acknowledgement would not be complete without mentioning the help of my family. I would like to thank my father (may God rest his soul) and my mother for their endless sacrifices and tireless efforts and for always believing in me. They have provided me with a lot of love, encouragement, and support, and have worked very hard to ensure a bright future for me. I am sure my father would have been so proud of me!

I would like to express my gratitude to my uncle, Prof. Ali Elnaiem, my role model in life and science, for his persistent encouragement during my undergraduate studies in Cairo and for instilling in me endless love/passion for, excitement about and obsession with science . . . Thank You!

My warmest, heartfelt thanks goes to my loving wife, Rania Ammar, for all the great shoulders and for the sacrifices throughout the Ph.D. program. She has patiently tolerated so many sleepless nights I had where I stayed up working on homework or finals, or just purely obsessing over my research. Finally, I would like to thank the little new arrival, Eyad Abdilghanie, for providing a lot of emotional uplifting during the final stretch of my Ph.D.!

TABLE OF CONTENTS

Biographical Sketch . . . iii
Dedication . . . iv
Acknowledgements . . . v
Table of Contents . . . viii
List of Tables . . . x
List of Figures . . . xi

1 Introduction **1**
1.1 Basics of stratified fluids . . . 1
1.2 Nature of turbulence in geophysical flows . . . 3
1.3 Buoyancy control in stratified turbulent flows . . . 5
1.4 Internal gravity waves . . . 11
1.4.1 Background and motivation . . . 11
1.4.2 Properties of internal waves . . . 13
1.4.3 Instability mechanisms . . . 16
1.5 Experimental generation of internal gravity waves . . . 19
1.6 Numerical generation of internal gravity waves . . . 21
1.7 Remote interactions of internal gravity wave packets . . . 22
1.8 Nonlinearity and dispersion of internal gravity waves . . . 23
1.9 Generation of internal gravity waves by turbulence . . . 25
1.10 Wake generated internal gravity waves . . . 29

2 Scope and objectives of the thesis **35**
2.1 Working hypotheses . . . 35
2.2 Open questions: Wake-generated internal gravity waves . . . 36
2.3 Open questions: Numerically forced internal gravity waves . . . 38
2.4 Specific objectives: Wake-generated internal waves . . . 39
2.5 Specific objectives: Numerically forced internal gravity waves . . . 41

3 Spectral multidomain penalty solver basics **43**
3.1 Governing Equations . . . 43
3.2 Temporal discretization scheme . . . 45
3.3 Spatial discretization scheme . . . 47
3.4 Stabilization methods: spectral filtering and penalty techniques . . . 50

4 On the continuous wavelet transform and its use in fluid mechanics **53**
4.1 Spectral versus physical representation of signals . . . 53
4.2 Fundamentals of the 1-D continuous wavelet transform . . . 55
4.3 2-D continuous wavelet transforms . . . 60
4.4 Applications in fluid mechanics . . . 65

5 Internal wave emission by a stratified turbulent wake **69**
5.1 Problem setup . . . 69
5.2 Initialization . . . 71
5.3 Summary of numerical simulations . . . 72
5.4 Wave sponge layers . . . 77
5.5 Results . . . 79
5.5.1 Visualization of the wave field structure . . . 79
5.5.2 Spectral characteristics of the internal gravity wave field . 88
5.5.3 Degree of nonlinearity . . . 102
5.6 Discussion . . . 104

6 Numerical generation and evolution of large amplitude internal waves **110**
6.1 Problem description . . . 110
6.2 Numerical simulations summary . . . 111
6.3 Results . . . 114
6.3.1 Horizontally periodic and vertically compact wave packet 114
6.3.2 Effect of horizontal localization . . . 117
6.4 Model for wave packet deformation . . . 121
6.4.1 Mean flow evolution equation and scaling . . . 121
6.4.2 Approximate solution at early times . . . 124
6.4.3 Mean flow structure at later times . . . 126
6.4.4 Mean flow reduction due to horizontal localization . . . 130
6.4.5 Residual mean flow containment techniques . . . 133
6.4.6 Critical level interaction . . . 137
6.5 Discussion . . . 141
6.5.1 Mature wave-packet: generation via mechanical forcing vs. impulsive introduction . . . 141
6.5.2 Generation of an internal wave train . . . 142
6.5.3 Additional connections with the laboratory and nature . . 143

7 Conclusions and future work **145**
7.1 Concluding remarks . . . 145
7.1.1 Wake-generated internal gravity waves . . . 145
7.1.2 Numerically forced internal gravity waves . . . 148
7.2 Future work . . . 152

A Testing the continuous wavelet transform code **155**

B Directional data statistics **162**

LIST OF TABLES

5.1 Summary of the band averaged power law fit coefficients from the Arc wavelet transforms ($\lambda_H/D = \alpha N t^{\beta}$) 92
5.2 Summary of the azimuth angles and the band averaged power law fit coefficients from the *Morlet2D*wavelet transforms (ϕ , $\lambda_H/D = \alpha N t^{\beta}$) 96
5.3 Summary of the band averaged power law fit coefficients for the tangent of the polar angles ($tan(\theta) = \alpha N t^{\beta}$). 101
5.4 Summary of the band averaged power law fit coefficients for the normalized vertical length scales ($\lambda_z/D = \alpha N t^{\beta}$). 101

6.1 Parameter values used in the base-case simulation 113
6.2 Values for additional parameters relevant to critical level simulation: Unless otherwise listed, all other parameters have the same value as in the baseline case described in table 6.1. 138

LIST OF FIGURES

1.1 Schematic of internal wave rays radiated away from a vertically oscillating horizontal cylinder in a uniformly stratified fluid. . . 14

3.1 Exploded view of the wake core region of an Oxz section of the numerical grid employed in the simulations of a stratified turbulent wake at (a) $Re = 5 \times 10^3$ (where $M = 7$ subdomains of order of approximation $\hat{N} = 24$, with subdomain origins located at $z/D = -6, -3.17, -1.67, -0.5, 0.5, 1.67$ and 3.17) (b) $Re = 10^5$ (where $M = 13$ subdomains of order of approximation $\hat{N} = 40$, with subdomain origins located at $z/D = -6, -3.67, -2.33, -1.33, -0.8, -0.4, -0.13, 0.13, 0.4, 0.8, 1.33, 2.33,$ and 3.67). 48

3.2 Exponential filter functions $\sigma(k/k_C)$ for the four different filter orders $p =$ 6,8, 10, and 20 used in this study. In Legendre space, k and k_C represent the mode number and total number of available modes, respectively. In Fourier space, k and k_C represent the two-dimensional wavenumber vector magnitude and the corresponding maximum value over all resolved horizontal wavenumbers, respectively 51

4.1 Examples of mother wavelets. (a) Gaussian wave (first derivative of a Gaussian). (b) Mexican hat (second derivative of a Gaussian. (3) Haar. (4) Morlet (real part) 56

4.2 Basic manipulations of a Morlet mother wavelet. (a) Mother wavelet. (b) Translated wavelet. (c) Rescaled (dilated) wavelet. (d) Translated and rescaled wavelet. 57

4.3 *Morlet2D* wavelet at $\alpha = 45°$(a) Fourier transform (b) Real part in physical space (c) Imaginary part in physical space 62

4.4 Arc wavelet: (a) Fourier transform (b) Real part in physical space (b) Imaginary part in physical space 63

4.5 Frequency doubling: (a) time domain (b) 2D contours of the CWT modulus in the wavelet space (contour levels are arbitrary) 64

5.1 Computational domain for the simulation of a stratified turbulent wake with non-zero net momentum. 70

5.2 Rayleigh damping layer profile in the wall normal direction η . . 80

5.3 Two dimensional contours of the Rayleigh damping layer coefficient $R(y, z)$ 80

5.4 Two dimensional contour plot of $\mathbf{\Delta}_z/N$ at different times on horizontal xy planes at z/D=1.5, 2.3, 3.4 for (a) R5F4, (b) R5F16, (c) R5F64. The sphere travels from left to right. The min./max. ranges for the colorbars of $\mathbf{\Delta}_z/N$ are (a) [-0.025,0.025], (b)[-0.04,0.04] , and (c) [-0.05,0.05]. 83

5.5 Two dimensional contour plot of $\mathbf{\Delta}_z/N$ at different times through $15 < Nt < 50$ on horizontal xy planes at z/D=1.5, 2.3, for (a) R100F4, (b) R100F16. The min./max. ranges for the colorbars of $\mathbf{\Delta}_z/N$ are (a) [-0.05,0.05], (b)[-0.075,0.075]. 85
5.6 Two dimensional contour plot of $\mathbf{\Delta}_z/N$ at different times through $60 < Nt < 100$ on horizontal xy planes at z/D=1.5, 2.3, for (a) R100F4, (b) R100F16. The min./max. ranges for the colorbars of $\mathbf{\Delta}_z/N$ are (a) [-0.05,0.05], (b)[-0.075,0.075]. 86
5.7 Two dimensional contour plot of $\mathbf{\Delta}_z/N$ at different times through $15 < Nt < 50$ on a vertical xz planes at y/D=1.5 for (a) R5F4, (b) R100F4. The min./max. ranges for the colorbars of $\mathbf{\Delta}_z/N$ are (a) [-0.025,0.025], (b)[-0.05,0.05]. 87
5.8 Three dimensional isosurface plot of the modulus of the Arc wavelet transform of an xy plane for $R5F4$ at $Nt = 30$. The horizontal axes are the physical space axes x and y. The vertical axis is the horizontal wavelength (normalized by the sphere diameter) corresponding to the wavelet scale. 88
5.9 The normalized horizontal divergence field on a horizontal xy plane at $z/D = 1.5$ for $R5F4$ at $Nt = 30$. The min./max. ranges for the colorbars are [-0.04,0.04] 91
5.10 A vertical transect through the modulus transform cube (Fig. 5.8) at $y/D = 2.5$. 91
5.11 The evolution of the normalized horizontal wavelength obtained from the Arc wavelet transform of the horizontal divergence field on a horizontal xy planes at $z/D = 1.5, 2.3, 3.4$ for $R5F4$, $R5F16$, $R5F64$, respectively. Color coding is as follows: red for $Fr = 4$, blue for $Fr = 16$, black for $Fr = 64$. Circles and squares represent data at $y/D = 1.5, 2.5$ for $Fr = 4, 16$ and $y/D = 2.5, 4.5$ for $Fr = 64$, respectively. Solid lines are band-averaged power law fits. 93
5.12 The evolution of the normalized horizontal wavelength obtained from the Arc wavelet transform of the horizontal divergence field on a horizontal xy planes at $z/D = 1.5, 2.3$ for $R100F4$, $R100F16$, respectively. Legend as in Fig. 5.11. 93
5.13 Fr scaling of the normalized horizontal wavelength obtained from the Arc wavelet transform of the horizontal divergence field on a horizontal xy planes at $z/D = 1.5, 2.3, 3.4$ for $R5F4$, $R5F16$, $R5F64$, respectively. Legend as in Fig. 5.11 94
5.14 Fr scaling of the normalized horizontal wavelength obtained from the Arc wavelet transform of the horizontal divergence field on a horizontal xy planes at $z/D = 1.5, 2.3$ for $R100F4$, $R100F16$, respectively. Legend as in Fig. 5.11. 94

5.15 Scatter plot for the horizontal length scales obtained from the Arc and *Morlet2D* wavelet transforms for the five different simulations. Legend as in Fig. 5.11 with filled symbols for $Re = 10^5$ data and open symbols for $Re = 5 \times 10^3$. The black solid line is the identity line. 96
5.16 Streamwise-time ($x - t$) diagram of the normalized horizontal divergence field at $y/D = 1.5$, $z/D = 1.5$ for $R5F4$.The min./max. ranges for the colorbars of $\mathbf{\Delta}_z/N$ are [-0.025,0.025]. 99
5.17 Streamwise-time ($x-t$) diagram of the normalized horizontal divergence field at $y/D = 1.5$, $z/D = 1.5$ for $R100F4$.The min./max. ranges for the colorbars of $\mathbf{\Delta}_z/N$ are [-0.05,0.05]. 99
5.18 Evolution of the phase line tilt/polar angle obtained from the one dimensional wavelet transforms. Legend as in Fig. 5.11 with filled symbols for $Re = 10^5$ data and open symbols for $Re = 5 \times 10^3$. 100
5.19 Evolution of the vertical group velocity obtained from the five simulations. Legend as in Fig. 5.11 with filled symbols for $Re = 10^5$ data and open symbols for $Re = 5 \times 10^3$. 102
5.20 Fr scaling of the vertical group velocity obtained from the five simulations. Legend as in Fig. 5.11 with filled symbols for $Re = 10^5$ data and open symbols for $Re = 5 \times 10^3$. 103
5.21 Evolution of the internal wave field steepness from the five simulations. Color coding is as in Fig. 5.11 with filled symbols for $Re = 10^5$ data and open symbols for $Re = 5 \times 10^3$. 105
5.22 Comparison of the maximum wave steepness in all five simulations to the internal wave instability limits, plotted against the phase line tilt angle θ. Symbols' color coding is as in Fig. 5.11 with filled symbols for $Re = 10^5$ data and open symbols for $Re = 5 \times 10^3$. Black solid line represents the self acceleration limit while the blue solid line indicates the overturning limit. Finally, the red solid line represents the convective breaking limit. 105

6.1 Schematic of problem setup: a vertically localized IGW is generated in the forcing region and allowed to freely propagate downward. In the critical level simulation, a Gaussian background shear flow is positioned near the bottom of the computational domain. 112
6.2 Two-dimensional contours of the horizontal velocity field at $t = 5T_w$ in a fully nonlinear simulation of a horizontally periodic, vertically localized wave packet, for $Ri = 1$ (contours are normalized by the horizontal velocity amplitude $A_u = AU_o m/k$ at $t = T_w$). 116
6.3 Vertical profile of the instantaneous horizontal velocity at $x = L_x/2$ at $t = T_w$and $5T_w$ in a fully nonlinear simulation of a horizontally periodic, vertically localized wave packet, for $Ri = 1$. . . 116

6.4 Comparison of the analytical and numerical solutions of the mean flow evolution during the wave generation phase in a fully nonlinear simulation of a horizontally periodic, vertically localized wave packet, for $Ri = 1$. 117
6.5 Vertical profile of the instantaneous horizontal velocity at $x = L_x/2$ compared at $t = T_w$ and $5\,T_w$ in a fully nonlinear simulation of a horizontally periodic, vertically localized wave packet, for $Ri = 16$. 118
6.6 Two-dimensional contours of the horizontal velocity field at $t = 5T_w$ in a fully nonlinear simulation of a both vertically and horizontally localized wave packet,, for $Ri = 1$. 120
6.7 Vertical profile of the instantaneous horizontal velocity at the instantaneous wave packet center, x_c, compared at $t = T_w$ and $5\,T_w$ in a fully nonlinear simulation of a both vertically and horizontally localized wave packet, for $Ri = 1$. 120
6.8 Richardson number-rescaled mean flow profiles in fully nonlinear simulations of a horizontally periodic, vertically localized wave packet at $Ri = 1$ and 16. 123
6.9 Comparison of the mean horizontal flow profile and the wave pseudomomentum , $M(z)$, in a fully nonlinear simulation of a horizontally periodic, vertically compact wave packet at $t = T_w$ and $5\,T_w$, for (a) $Ri = 1$ (b) $Ri = 16$. 127
6.10 Comparison of the mean horizontal flow profiles at $t = 10T_w$ and $15\,T_w$, in a fully nonlinear simulation of a horizontally periodic, vertically compact wave packet in a domain with height $L_z = 6\lambda_x$, for $Ri = 16$. 128
6.11 Vertical profiles of the sum of all the r.h.s. terms of equation (18) $(I + II + III)/(A_u/T_w)$ and the second term $II/(A_u/T_w)$, in a fully nonlinear simulation of a horizontally as well as vertically localized wave packet at $t = T_w$, for $Ri = 1$. 132
6.12 Comparison of the numerical computed horizontal mean flow for a horizontally periodic and a horizontally localized IGW packet at $t = T_w$, for $Ri = 1$. 134
6.13 Comparison of the mean horizontal flow in a fully nonlinear simulation and linear simulations, along with simulations in which either the zero Fourier mode is removed or the proposed mean flow absorbing term is used, for a horizontally periodic vertically localized wave packet at $t = 5T_w$, with $Ri = 1$ (note that the mean flow is zero everwhere in both the linear simulation and that with the zero Fourier mode removed). 136
6.14 Vertical profile of the instantaneous horizontal velocity at $x = L_x/2$, compared at $t = T_w$ and $5\,T_w$ in a fully nonlinear simulation of a horizontally periodic vertically localized wave packet in which the mean flow absorbing term is used, for $Ri = 1$. 137

6.15 Mean flow evolution during the wave-shear flow interaction for the critical level simulation . . . 139
6.16 Two dimensional contours of the vorticity field for the critical level simulation (a) $Nt = 52$ (b) $Nt = 55$. The min/max range for the colorbar for the two snapshots is symmetric about $\omega_y = 0$ to $\pm(|\omega_y^{max}| + |\omega_y^{min}|)/2$ at $Nt = 50$ (i.e. close to the onset of the shear instability). . . . 140

A.1 A chirp signal: (a) time domain (b) wavelet domain . . . 156
A.2 Same frequency at two different times: (a) time domain (b) wavelet domain . . . 156
A.3 Two different frequencies at two different times: (a) time domain (b) wavelet domain . . . 157
A.4 (a) A 2D spatial test signal composed of one wave number/length scale (b) Plane averaged modulus of the 2D Arc wavelet transform. . . . 158
A.5 CARRÉ test signal . . . 159
A.6 CARRÉ test signal: (a) Modulus of the 2D Arc wavelet transform at $x = 50$, $y = 50, 180$ (b) Modulus of the 2D Arc wavelet transform at $x = 50$ and $a = 5, 10$ . . . 159
A.7 (a) A 2D spatial test signal composed of one wave number oriented at 45° to the x axis. (b) Plane averaged modulus of the *Morlet2D* wavelet transform at multiple interrogation angles . . . 161

B.1 Rose diagrams of resonance angles obtained at multiple spanwise locations y/D on the right half xy plane at $z/D = 1.5$ for the $R5Fr4$ simulation over $10 < Nt < 50$ . . . 164

CHAPTER 1

INTRODUCTION

1.1 Basics of stratified fluids

Stratified fluids are characterized by variations of their mean densities with height/depth as a result of corresponding change in temperature or salinity or a combination thereof. The rate of change of density in a stably stratified fluid, i.e. a fluid in which the mean density decreases with height, is related to its so called buoyancy/Brunt-V*äisälä* frequency N through

$$N^2 = -\frac{g}{\rho_o}\frac{d\overline{\rho}}{dz}, \tag{1.1}$$

where g is the gravitational acceleration, ρ_o is a constant reference density, $\overline{\rho}(z)$ is the mean/background density of the fluid and z is vertically upward. Precisely, the buoyancy frequency is the frequency of natural/unforced oscillations of a fluid parcel, vertically displaced from its equilibrium position, and is the highest frequency that buoyancy-driven motion can have (Baines, 1995; Sutherland, 2005). Typical values of N in the ocean and atmosphere are about $10^{-2}s^{-1}$ and, accordingly, the time scales of buoyancy driven motions are on the order of tens of minutes (Sutherland, 2005).

Stably stratified fluids are ubiquitous in nature. Examples include the stratosphere which is the part of the atmosphere between 10 and 50 kms; the bulk of the ocean interior; and the interior of stars (Staquet, 2005). Temperature inversions in Los Angeles basin are a major source of trapping of pollutants from traffic and factories in the boundary layer near the ground surface. In such a layer stable stratification is set up either by cooling at night upon ex-

change of heat with the ground or by cold air blowing onshore after passing over cold ocean water. The temperature inversion layer acts as a lid and prevents the dispersion of pollutants until it breaks up by changing weather conditions (Aguado & Burt, 2003).

Prominent examples of engineering applications of stably stratified fluids include solar ponds and nuclear reactors' cooling circuits (Staquet, 2005). In solar ponds the bottom of a pond is made dark and very salty so that upon heating by the sun it does not get convected upwards (as it remains heavier than the layer above). By retaining a warm bottom, the pond can be used to warm the water inside pipes that cross the pond at its lowest part (Staquet, 2005).

Air sear interactions such as wind forcing and storms lead to the generation of turbulence that mixes up the region immediately below the sea surface. Below the surface mixed layer, the density increases with depth in a layer known as the "pycnocline", usually a result of temperature decrease. The density continues to increase with depth below the pycnocline, however, at much smaller rates. Near the seabed, turbulence generated by flows over topography leads to mixing of the bottom boundary layer (also referred to as the "benthic" boundary layer).

As discussed in §1.4, stable stratification, in the presence of buoyancy forces, supports internal gravity waves. The breaking of such waves has been suggested as a major source of mixing in the interior of the ocean (Munk & Wunsch, 1998). Accordingly, it is important to study the properties of these waves and understand the dynamics of their breaking and the resulting turbulence. On the other hand, and as detailed in §1.9, turbulent regions are known to radi-

ate internal gravity waves that propagate over long distances away from their sources. As internal gravity waves extract energy from turbulence, they can modify the energy budget and the dynamics of the turbulent source regions. As internal gravity waves move vertically through the ocean, they provide a distinct signature that can lead to the remote detection of their turbulent sources. Accordingly, understanding turbulence in the ocean is essential for the study of internal gravity waves.

1.2 Nature of turbulence in geophysical flows

Much of our current understanding of turbulent flows is based on invoking three major assumptions employed by Kolmogorov: namely, stationarity, homogeneity, and isotropy (Smyth & Moum, 2001). Stationarity means that the statistics of the flow are independent of time while homogeneity implies that the statistics are invariant under spatial translation of the axes. Finally, isotropy refers to invariance of the statistics under rotation and reflection of the axes (Pope, 2000).

Geophysical flows are often complicated by the presence of background shear flows such as large scale currents in the ocean and jet streams in the atmosphere. Large scale turbulent eddies are deformed by the shear leading to both inhomogeneity and anisotropy. As a result, Reynolds stresses are produced; a mechanism by which turbulent eddies exchange momentum with the background shear that would not be possible if the turbulence were isotropic (Smyth & Moum, 2001, 2000).

As fluids comply to the boundary conditions appropriate to their bounding surfaces such as the no-slip and no-flux conditions at the ocean floor and the more flexible conditions at the ocean surface (e.g. stress-free, wind forcing..etc), homogeneity and isotropy are again violated. The compliance of the fluids to such boundary conditons lead to a variety of interesting phenomena such as turbulent bottom boundary layers which are sites of intense mixing and transport and the formation of surface waves and Langmuir cells near the ocean surface (Smyth & Moum, 2001).

Turbulence is typically generated in geophysical flows by spatially localized sources such as breaking internal waves, local shear instabilities and flows behind finite sized obstacles and moving objects (Lelong & Dunkerton, 1998; Lombard & Riley, 1996; Orlanski & Bryan, 1969; Turner, 1980; Lin & Pao, 1979; Diamessis, Domaradzki & Hesthaven, 2005). The resulting turbulence is dramatically different from the highly idealized space-filling homogeneous turbulence. Additionally, the presence of finite-sized, buoyancy-controlled, localized turbulent events inside a stratified fluid, naturally capable of supporting the propagation of internal gravity waves, enables a new sink of turbulent kinetic energy (in the form of internal gravity waves radiated away from the localized turbulent region) that does not have a counterpart in homogeneous fluids. Finally, the often episodic nature of turbulent events in the ocean and atmosphere precludes stationarity of the underlying turbulence on account of the transitory nature of the turbulence-generating source/forcing.

1.3 Buoyancy control in stratified turbulent flows

Buoyancy can have a significant impact on the evolution of turbulence in stratified fluids. Specifically, stratification in the presence of a gravity force field is another source for breaking the symmetry of turbulent flows by imposing constraints on the motion of fluid particles oriented along the gravity vector. Riley, Metcalfe & Weissman (1981) performed one of the earliest direct numerical simulations of homogeneous turbulence in density stratified fluid, as a simple extension to turbulence in homogeneous fluids that provided insight into the basic characteristics of turbulence in stratified flows. They found that stratification leads to exchange from (and to) kinetic to (and from) potential energies, and the development of counter-gradient buoyancy flux leading to the generation of wave motion. They also found that stratification enhances the growth of horizontal scales while inhibiting the growth of vertical scales. Finally, the dissipation of the turbulent kinetic energy was smaller in two cases with different stratification levels relative to a case with zero background density gradient.

Arguably, stable stratification inhibits vertical motion by setting a threshold on the minimum kinetic energy that overturning turbulent eddies at a given scale have to have in order to exist (Spedding, 2002*a*). According to Riley & Lelong (2000) physical arguments and dimensional analysis were used independently by Dougherty (1961), Ozmidov (1965), and Lumley (1964) to derive the overturning/Ozmidov scale ℓ_o as

$$\ell_o = (\epsilon/N^3)^{1/2}, \tag{1.2}$$

where ϵ is the dissipation rate of turbulent kinetic energy. As Ozmidov scale provides an estimate for the largest turbulent eddies at which overturning can occur, one of the approaches to understanding the influence of stratification on

turbulence is to compare the evolution of some characteristic of the overturning turbulent motion vertical scale to the Ozmidov scale (Itsweire, Koseff, Briggs & Ferziger, 1993).

By means of numerical simulations of a homogeneous stratified shear flow Itsweire, Koseff, Briggs & Ferziger (1993) found, in agreement with the laboratory experiments (Itsweire, Helland & Van Atta, 1986), that the onset of buoyancy control, where significant fraction of the large scale eddies are dominated by stratification, occurred when the Ozmidov scale was nearly equal to the vertical scale of the density fluctuations and that stratification eventually controlled all scales of motion when Ozmidov scale was about an order of magnitude larger than the Kolmogorov scale. The first transition point marks the end of what Gibson (1980, 1986) refers to as "active" turbulence and the beginning of the buoyancy affected regime which he refers to as "active+fossil". The second transition point represents the begining of the "fossil" turbulence regime where buoyancy controls the flow at all scales.

While Gibson's ideas are useful in explaining some aspects of turbulence in stratified flows, they do not explain some of the features of laboratory experiments, numerical simulations and geophysical data (Riley & Lelong, 2000). An example for such experiments is that performed by Lin & Pao (1979) in which they towed an axisymmetric object horizontally in a density stratified tank. They found that the near wake dynamics are similar to the classical wake dynamics in homogeneous fluids. However in the far field they found that the stratification has considerably affected the behavior of the wake. They also found that the late wake consists of quasi-horizontal motions (they referred to as "pancake street") with complex vertical structure along with an internal

gravity wave field.

For stratified turbulent flows, a local Froude number can be defined as

$$F = u'/N\ell, \tag{1.3}$$

where u' is a measure of the horizontal fluctuating/turbulent velcity and ℓ is a characteristic length scale of the energy containing eddies (such as the horizontal or vertical scale of the pancakes). It is thus a measure of the relative importance of the buoyancy compared to inertial forces. As turbulence decays u' decreases and ℓ tends to increase until the local Froude number becomes $O(1)$ and the buoyancy forces start to dominate the flow. This argument has motivated the development of asymptotic theories for the $F = 0$ limit (Riley, Metcalfe & Weissman, 1981). One of the essential features of the low Froude numer based theories (Riley, Metcalfe & Weissman, 1981; Embid & Majda, 1998) is the ability to clearly differentiate and hence isolate the propagating (internal gravity waves with their associated fast time scales) and the non-propagating slowly varying components of the flow (Riley & Lelong (2000) refers to this as the "PV" component of the flow, as it carries all the potential vorticity of the flow, while Lilly *et al.* (1998) calls it "stratified turbulence").

Multiple experimental investigations of the dynamics of the stratified turbulent wake of a towed sphere, as a canonical localized turbulent flow with shear and stratification, were performed by Spedding and co-workers (Spedding, Browand & Fincham, 1996*a*,*b*; Spedding, 1997*a*,*b*, 2001, 2002*a*,*b*). Particle Image Velocimetry (PIV) was used to obtain accurate two-dimensional measurements of the velocity field across horizontal and vertical transects through the mid-to-late time wake. A broad range of internal Froude numbers, $Fr \equiv 2U/(ND) \in [4, 240]$ was considered, where U, D and N are the tow speed,

sphere diameter and buoyancy frequency, respectively. The maximum body-based Reynolds number, $Re = UD/\nu$, value attained in these experiments was $Re = 2\times10^4$. For a minimum value of $Re \approx 5\times10^3$, scaling arguments (Spedding, Browand & Fincham, 1996*a*) and subsequent experiments (Spedding, Browand & Fincham, 1996*b*) found that the minimum Froude number value necessary to obtain a fully three-dimensional turbulent near wake was equal to $Fr \approx 4$, in agreement with the value proposed by Chomaz *et al.* (1993). For the above Fr range and values of Re exceeding the indicated minimum, Spedding (1997*a*) demonstrated that all wakes have self-similar scaling behavior. The underlying cause for the self-similar scaling is that the decrease in local wake velocities is accompanied by an increase in local length scales. As a result, a local Froude number based on these scales will decrease until it becomes of $O(1)$. Thus, regardless of the initial Froude number/level of stratification, the late stages of a stratified wake will eventually be fully controlled by buoyancy.

Based on studying the variation of the exponents of the power laws associated with the self-similar scaling of the mean defect velocity profile and physical arguments, Spedding (1997*a*) identified three dynamical regimes in stratified wake evolution. At early times, *three-dimensional (3-D)* non-stratified turbulent axisymmetric wake structure and dynamics govern the flow. Experiments (Browand, Guyomar & Yoon, 1987), numerical simulations (Itsweire, Koseff, Briggs & Ferziger, 1993) and theoretical analysis (Gibson, 1980; Riley & Lelong, 2000) of decaying stratified turbulent flows conducted prior to Spedding (1997*a*) indicate that buoyancy forces begin to influence the larger scales of the flow around $Nt \approx 1$. The corresponding manifestation of the onset of buoyancy control in experiments on stratified wakes of self-propelled slender bodies was a suspension of the growth of the wake height at $Nt = 2$ (Lin & Pao, 1979) (Nt is defined as $2\pi t/T_b$ where $T_b = 2\pi/N$, thus $Nt = 2\pi$ corresponds to one

buoyancy period).

At $Nt \approx 2$, the wake dynamics transition into the non-equilibrium (NEQ) regime which is characterized by reduced decay rates of the horizontal mean velocity. Spedding (1997*a*) conjectured that this deceleration of mean defect velocity decay can be attributed to the conversion of available potential to kinetic energy near the wake center through restratification effects. The wake width continues to grow exactly like its unstratified counterpart (Tennekes & Lumley, 1972). In contrast, the wake height remains approximately constant throughout NEQ and was found to scale approximately as $Fr^{0.6}$ (Spedding, 2002*a*). Two other key features of NEQ are the gradual suppression of vertical velocities and transport inside the wake core (Spedding, 2001) and the radiation of high-frequency internal waves from the wake into the ambient. It is during the NEQ regime that coherent patches of vertical vorticity with low aspect ratio (the "pancake" vortices in Lin & Pao (1979)) emerge, growing both by merging and diffusion (Spedding, 1997*a*).

A steeper decay rate of the mean defect velocity, with is then observed at a transition time of $Nt \approx 50$, leading into the quasi two-dimensional regime (Q2D) that persists for all measurable times up to $Nt \approx 2,000$ (Spedding, 1997*a*). A $(x/D)^{1/3}$ power law continues to characterize wake-width growth. The wake height transitions into a diffusively-driven growth. Once the Q2D regime has been established, almost all remaining kinetic energy in the flow resides within the pancake vortices, as vertical velocities are near-negligible. The horizontal structure of the wake consists of quasi-two-dimensional countersigned vortices resembling a two-dimensional wake but with a vertical structure (Riley & Lelong, 2000). The flow field nonetheless is not purely two-dimensional and

the mean flow does not follow the decay laws of plane wakes (Tennekes & Lumley, 1972). Horizontal vorticity field on a vertical plane indicates pairs of opposite-signed stable and highly diffuse inclined vertical shear layers (Spedding, 2002*a*). Each shear layer pair is inferred to be a cross section through a vertically coherent pancake eddy, with the maximum shear occuring at the pancake edges. Viscous diffusion provides a means of vertical coupling across shear layers and is responsible for their thickening and eventual merging.

Fincham, Maxworthy & Spedding (1996) found that the vertical derivative of the horizontal velocities contributes 80% towards the kinetic energy dissipation rate and thus the horizontal derivatives contribution is very little. Hence as Spedding (2002*a*) comments: although the vertical vorticity structure on horizontal planes is the most prominent feature observable in the laboratory, it is the vertical variation (i.e. the vertical shear) in these motions and at the upper and lower wake boundaries that is most intense. Lilly, Bassett, Droegemeier & Bartello (1998) suggested that at sufficiently high Reynolds numbers the flow in adjacent horizontal layers would tend to decouple, leading to shear instabilities and small-scale secondary turbulent events. The secondary turbulent events at high Reynolds numbers can have significant impact on the late time wake dynamics. Diamessis, Spedding & Domaradzki (2010*b*) found that the increased shearing along with the secondary turbulent events lead to prolongation of the Non-equilibrium regime as manifested in the persistence of the slower decay rates of the mean wake kinetic energy. They also found that these intermittent turbulent events possess significant vertical kinetic energy leading to overturning at times where, based on their results, buoyancy is believed to have completely suppressed the original turbulence. They suggest a reexamination of the commonly perceived life-cycle of a localized stratified turbulent

patch and a possible reconsideration of the existing parametrization of stratified turbulence and mixing in the ocean and atmosphere.

As internal waves are radiated by the wake during the NEQ regime, it is reasonable to expect that intense internal wave radiation will continue over much longer time at high *Re*, on account of the prolongation of the NEQ regime.

1.4 Internal gravity waves

1.4.1 Background and motivation

In the presence of a continuously varying stable background density gradient ($d\overline{\rho}/dz < 0$), a perturbed dense fluid parcel moving upward towards a less dense level will , by virtue of gravity, experience a net downward force that tends to restore the parcel to its equilibrium position. The resulting oscillatory motion is generically referred to as an "internal gravity wave". Unlike the interface-trapped horizontally-moving surface waves that form at large density discontinuities such as the air-water interface at the ocean surface, the existence of a continuously varying density gradient adds the possibility of vertically propagating internal waves in the form of beams or rays that cross the constant density surfaces (isopycnals) transporting energy through the ocean/atmosphere away from their sources (Thorpe, 2005).

Upon successive reflections of internal wave beams in a finite depth water, horizontally moving internal waves with a characteristic vertical structure (vertical wave modes) can be produced (Garrett & Kunze, 2006). Solitons; horizontally

moving long-wave pulse or train of pulses that maintain their shape during propagation, are also another common form of internal waves that are often generated through the interaction of the barotropic tide with topographic features on and along the shelf break (Diamessis & Redekopp, 2006).

"Vertically propagating" internal waves occur throughout the atmosphere and ocean on scales as small as meters and as large as thousands of kilometers (Sutherland, 2005). Internal wave beams having the internal tide period are often detected near topographic features in the ocean (Thorpe, 2005). Mountain waves are another example for internal wave radiation resulting from the disturbances created by the rising air over a topographic barrier or strong winds blowing down the mountain along its lee slope (Durran, 1990). In mid-water internal wave beams are radiated away from regions of active turbulent mixing and during the collapse of a mixed region of decaying turbulence (Maxworthy, 1980; Thorpe, 2005). As the focus of this thesis is on vertically propagating internal waves we will refer to them hereafter as just internal gravity waves (IGWs) without the vertical propagation qualifier.

Small scale turbulence leading to mixing in mid-air/water typically results from the breaking of IGWs (Munk & Wunsch, 1998). This process is accounted for in large-scale circulation models through a turbulent diffusivity. Waves also deposit momentum into the local mean flow at the breaking level, a process that is usually modelled through a transport coefficient (Staquet, 2005). A robust understanding of these small scale processes is necessary for the development of accurate subgrid scale models that faithfully represent the effect of the small scale unresolved motions on the large resolved ones.

We now examine the spatial structure of IGWs and explore the relationships

between the various spectral characteristics of an internal wave beam (wave lengths, frequencies, phase and group velocities). Simple analytical relations between the wave properties can be derived under the assumption of small displacement amplitude. The relations thus obtained, although they hold only for low to moderate amplitude waves, provide a useful physical insight into the intriguing properties of these waves.

1.4.2 Properties of internal waves

Sutherland (2005) demonstrated the basic properties of IGWs through the use of parcel arguments and solutions to the linearized Navier Stokes equations under simplifying assumptions. Most notably, the dispersion relation for IGWs is derived based on the assumption of small parcel displacements and constant background density gradient. In essence this relation shows that fluid motions at an angle to the vertical occurs with frequency (ω), given by

$$\omega = N cos(\theta), \tag{1.4}$$

where θ is the angle that the 3D wave number vector $K = (\kappa, \ell, m)$ forms with the horizontal direction. This angle can be expressed in terms of K and its horizontal component $K_H = (\kappa, \ell)$ through

$$cos(\theta) = |K_H|/|K| = \sqrt{\frac{\kappa^2 + \ell^2}{\kappa^2 + \ell^2 + m^2}}. \tag{1.5}$$

The phase velocity vector; the vector whose direction is perpendicular to the constant phase lines and whose magnitude is the speed of the motion of crests along that direction follows from the dispersion relation:

$$C_p = \frac{\omega}{|K|}\frac{\vec{K}}{|K|} = \frac{N}{|K|} cos(\theta)\left[cos(\phi)cos(\theta), sin(\phi)cos(\theta), sin(\theta)\right], \tag{1.6}$$

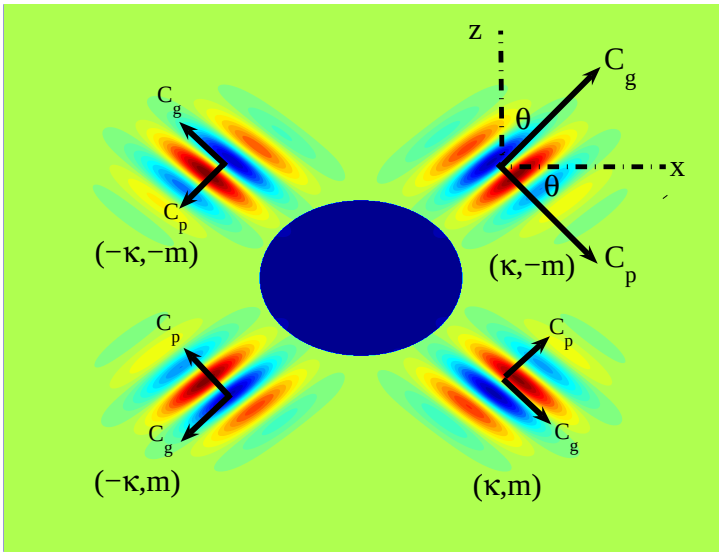

Figure 1.1: Schematic of internal wave rays radiated away from a vertically oscillating horizontal cylinder in a uniformly stratified fluid.

where $tan(\phi) = \ell/\kappa$. Finally, the group velocity; the velocity at which the energy is transported by the waves:

$$C_g = \nabla_K \omega = \left(\frac{\partial \omega}{\partial \kappa}, \frac{\partial \omega}{\partial \ell}, \frac{\partial \omega}{\partial m}\right) = \frac{N}{|K|} sin(\theta)\left[cos(\phi)sin(\theta), sin(\phi)sin(\theta), -cos(\theta)\right]. \quad (1.7)$$

An intriguing consequence of the above relations is that the group and phase velocities are perpendicular to each other and that if the wave transports energy upwards, then the phase lines move downwards and *vice versa* (Sutherland, 2005). Another interesting result is that the vertical component of the group velocity vanishes for waves with $\theta = 0$ and $\theta = 90^\circ$ and that the maximum group velocity is associated with waves having $\theta = 35^\circ$ (Sutherland, 2005). The above-mentioned properties of these waves are illustrated in Fig. 1.1 which rep-

resents a schematic of an internal wave beam pattern that mimics that which is generated experimentally by vertically oscillating a horizontal cylinder in a uniformly stratified fluid at a frequency ω. Mowbray & Rarity (1967) used this set up to verify the theoretically predicted phase line configuration and the wave dispersion relation.

The relations among the basic state fields (velocity components, density and pressure) for a small amplitude plane/infinitely periodic IGW, aka "polarization relations" were also derived by Sutherland (2005). Two important estimates that follow from these relations are the wave momentum transport:

$$\langle u'w' \rangle = \frac{1}{4} N^2 sin(2\theta) |A_\zeta^2|, \tag{1.8}$$

where A_ζ is the vertical displacement amplitude defined through $A_\rho = -\frac{d\overline{\rho}}{dz} A_\zeta$ where A_ρ is the amplitude of the density perturbation field associated with the IGW. Consequently waves with $\theta = 0$ and $\theta = 90^\circ$ do not transport horizontal momentum vertically. Also for waves having the same vertical displacement, A_ζ, those with $\theta = 45^\circ$ transport the maximum momentum (Sutherland, 2005).

As turbulence generates IGWs (see §1.9), it is important to emphasize some of the important differences between the properties of internal waves. Apart from the ability of IGWs to transport energy far from their generation sites and their limited range of spatiotemporal scales close to their generation sites compared to turbulence, the ability to clearly distinguish and separate internal gravity waves from turbulence is a fundamental issue in stratified turbulent flow that can potentially lead to improved understanding and subsequent computational data analysis of these flows. Jacobitz, Rogers & Ferziger (2002) summarize some of the subtle differences between turbulence and IGWs, namely:

- Wave motion satisfies linear equations, whereas turbulence is inherently nonlinear, However, when both waves and turbulence are present the motions are coupled nonlinearly and it is unclear how to extract the wave component of the flow.
- In turbulence, energy is advected at the speed of the motion, whereas waves transport energy via pressure-velocity correlations, usually at a group velocity that is greater than the particle velocity.
- Except when they break, waves do not produce mixing. Although they can transport momentum, they cannot transport scalars. Thus the scalar flux $\langle w'\rho' \rangle$, should be large in regions dominated by turbulence and small where waves predominate.
- The relative phase of vertical velocity fuctuations w' and density fuctuations ρ' is different for waves and turbulence. For stably stratified flows, in-phase motion between w' and ρ'corresponds to down-gradient turbulent transport, while 180° out-of-phase motion is associated with countergradient turbulent transport. For wave motions, w' and ρ' have a phase difference of 90° and there is no mean correlation between them.

1.4.3 Instability mechanisms

Internal gravity waves are prone to various types of wave instabilities that determine their fate as they propagate away from their generation sites. It is thus of naval as well as geophysical interest to assess the potential for wave breaking, the generation of small scale turbulence and the associated mixing of the water column.

Wave instabilities and breaking in mid-air/water redistribute the overall wave field energy into a wide range of space and time scales leading to a nearly universal spectrum. Such a spectrum was empirically determined by Garrett & Munk (1972, 1975) who relied on the linear theory to represent the structure and dispersion of the waves (Thorpe, 2005). As Sutherland (2006*a*) argues, nonlinear wave interactions far from their generation sites crucially determine how energy from various sources is transferred to such a wide and statistically stationary spectral range.

Breaking of IGWs in the ocean and atmosphere is often attributed to the presence of "critical levels" which are depths/altitudes at which the horizontal wave phase speed matches the velocity of a background shear flow (Bretherton, 1966; Booker & Bretherton, 1967; Winters & D'Asaro, 1989, 1994). The highly nonlinear interaction leads to intensification of the wave shear and overturning of the isopycnal surfaces until the waves eventually break via convective instability (Winters & D'Asaro, 1994). Even in the absence of background shear monochromatic, undamped IGWs can break when they become saturated (Jones & Houghton, 1971). Saturation occurs when IGWs move upward in a decreasing background density gradient where their amplitude has to increase to conserve their vertical flux of momentum (Eliassen & Palm, 1961). The continual increase of the waves' amplitude eventually leads to their breaking.

In the absence of shear and saturation, a plane periodic IGW is unstable due to parametric instability even at infinitesimally small amplitudes provided the time scale of the instability is smaller than the diffusive time scale of the waves (Sutherland, 2001). For the parametric instability, secondary waves of half the primary wave frequency grow in amplitude through resonant interac-

tions with the primary wave until they ultimately break (Drazin, 1977; Lombard & Riley, 1996). Sutherland (2005) argues that the parametric instabilities are not relevant to realistic situations, as their growth rates are too small to the extent that they may not grow sufficiently during the life-time of a typical IGW. He also argues that in most geophysical circumstances IGWs are not perfectly monochromatic and hence finite amplitude waves disperse as they propagate (Sutherland, 2005).

Through fully nonlinear numerical simulations, Sutherland (2001) showed that weakly nonlinear interactions between the waves and their wave-induced mean horizontal flow dominate the dynamics of large amplitude quasi-plane IGWs. Resonant interactions between the waves and their induced mean flow, known as "self-acceleration" occur when the waves are of such large amplitude that their wave-induced mean flow is at least as large as their horizontal group velocity (Sutherland, 2001). Sutherland (2001) derived the critical wave amplitude at which resonant interactions occur, namely

$$A_{SA} = \frac{1}{2\pi\sqrt{2}} sin(2\theta), \tag{1.9}$$

where $A_{SA} = A_\zeta/\lambda_x$ is referred to as the wave steepness, a quantity that measures how large is the wave displacement relative to its horizontal wavelength. Waves satisfying the self-acceleration condition, i.e. $A > A_{SA}$ evolve until they become convectively unstable and eventually break. Sutherland (2001) has also derived two analytical conditions for the critical wave steepness for overturning (static instability) A_{OT} and breaking (via convective instability) A_{CV}, namely

$$A_{OT} = \frac{1}{2\pi} cot(\theta), \tag{1.10}$$

$$A_{CV} = \frac{1}{2\pi} cot(\theta)(1 + cos^2(\theta)). \tag{1.11}$$

Waves satisfying the overturning condition (1.10) are statically unstable which means they are susceptible to convective instabilities and breaking. For breaking to happen, the time scale for the growth of the convective instability has to be much shorter than the wave period, otherwise the periodic wave motion will restore the statically unstable regions before breaking happens (Sutherland, 2001). The convective breaking condition however ensures that the convective instability has time to grow substantially before one wave period.

1.5 Experimental generation of internal gravity waves

It is important to review the experimental methods for IGW generation in the laboratory. The insight gained from such simple and controlled experiments, where IGW beams are generated by an oscillatory source, can help improve the reader's understanding of how IGWs propagate in a stratified fluid, how their properties are related to one another and to the source characteristics (size and frequency).

In their classical laboratory experiment, Mowbray & Rarity (1967) have oscillated a horizontal cylinder vertically in a stratified salt solution with constant buoyancy frequency N. As depicted in Fig. 1.1, four beams forming the so called "St. Andrew's cross" pattern emanate from the cylinder making an angle with the horizontal, in agreement with the dispersion relation based on the frequency of oscillation of the cylinder and the background frequency, and having a wavelength comparable to the cylinder diameter. If the cylinder oscillation stops a growing gap appears between the cylinder and the rays which continue to propagate now as "wave packets" (Thorpe, 2005).

Towing sinusoidal corrugated false floors, cylindrical or Gaussian shaped bumps horizontally inside a density stratified tank is another method by which internal gravity waves are usually generated in the laboratory (Thorpe, 1981; Koop, 1981; Koop & McGee, 1986). The waves thus generated are steady in a frame of reference moving with the object. In the laboratory frame, however, the waves propagate at the towing speed. The shape of the floor corrugation is dependent on the desired characteristics of the wave field. The sinusoidal corrugation is used to generate IGWs that can be approximated as monochromatic whereas the Gaussian/cylindrical objects are used when the desired wave field is broad-band and spatially compact (Koop, 1981).

More recently Gostiaux, Didelle, Mercier & Dauxois (2007) designed a novel wave generator that consists of a vertical stack of plates through which two camshafts go in order to control their relative positions. At rest the plates are shifted sinusoidally and the rotation of the camshafts apply the required periodic motion to the plates. The collective action of the plates is such that a unidirectional IGW is generated. The wave moves upward/downward for clockwise/anticlockwise rotation of the camshafts. The generated wave is nearly monochromatic both spatially and temporally and can have any complex wave form (e.g. sinusoidal, Gaussian..etc) by appropriately modifying the camshaft eccentricity.

1.6 Numerical generation of internal gravity waves

Two approaches are used to produce the initial IGW field in numerical process studies: One strategy designates an initial condition as a prescribed perturbation of the density and velocity fields or velocity stream functions in the form of an exact solution of the linearized internal wave equations (Winters & D'Asaro, 1989; Sutherland, 2006*a*; Lin, Ferziger, Koseff & Monismith, 1993). An alternative approach consists of introducing into the governing equations appropriately specified mechanical forcing (body force) terms, operative within a prescribed generation region (Slinn & Riley, 1998*a*; Dohan & Sutherland, 2005; Campbell & Maslow, 2003). The forcing can either have finite duration (Fritts, 1982) or persist throughout the entire simulation (Slinn & Riley, 1998*a*; Dohan & Sutherland, 2005; Zikanov & Slinn, 2001) generating either a localized packet or a continuous wave-train, respectively. The mechanical forcing approach is preferred as it allows greater control over the time-scale of energy injection into the IGW field and enables a closer comparison with laboratory experiments, as the structure of the forcing terms can be modeled after that of experimental IGW generators (such as the novel wave generator described by Gostiaux, Didelle, Mercier & Dauxois (2007)). Furthermore, the mechanical forcing has the advantage of allowing the initial IGW to develop more "naturally", i.e. within the constraints of the Navier-Stokes equation, which is particularly suitable for higher-order accuracy element-based flow solvers, such as the one used in this thesis (Diamessis, Domaradzki & Hesthaven, 2005). High-order accuracy numerical codes can be particularly sensitive to initial/boundary conditions and forcing that are not exact solutions of the governing equations (Boyd, 2001), as persistent and disruptive transients develop (Diamessis, Spedding & Domaradzki, 2010*b*).

1.7 Remote interactions of internal gravity wave packets

Once far from their generation site, internal gravity waves are capable of transporting energy over very long distances before depositing it remotely through localized breaking events in mid-water/air or near boundaries (Thorpe, 2005). In the study of IGW breaking, it is commonly assumed that the IGW under consideration is space-filling and of persistent duration. However, because of the transience in their generation, previously encountered nonlinear interactions in mid-water/air and the finite dimension of their source, IGWs often propagate as relatively short packets or groups of finite extent in one or more spatial dimensions. This limited extent can bear significant implications in characterizing the transmission, reflection and dissipation of an IGW interacting with a critical layer, sloping boundary or caustic (Thorpe, 2001). Important insight into the highly nonlinear physics of such interactions has been obtained through numerical process studies based on Direct Numerical or Large Eddy Simulations (DNS or LES) (Winters & D'Asaro, 1989; Javam & Redekopp, 1998; Slinn & Riley, 1998*a*; Javam, Imberger & Armfield, 2000; Campbell & Maslow, 2003).

Transmission/reflection phenomena and the additional turbulence/mixing due to breaking that accompany the interaction of an IGW with current shear, sloping topography or variable background stratification are sensitive to large wave steepness. The sensitivity of IGW dynamics is strongest the closer the initial wave steepness is to the breaking limit (Sutherland, 2001). Therefore, it is imperative that a DNS/LES study of IGW propagation and breaking be equipped with a wave generation mechanism that minimizes transients and allows maximum flexibility in choice of wave steepness without altering the

externally prescribed wave structure, vertical extent and characteristic properties (amplitude, primary frequency/wavelength and group/phase velocity predicted by linear theory). In particular, when a vertically localized IGW packet is required, it must remain robust both near the source but also during its subsequent propagation away from the source, prior to its arrival at the interaction region.

1.8 Nonlinearity and dispersion of internal gravity waves

The requirement of a wave packet with a finite spatial extent poses its own set of numerical challenges in terms of sustaining a packet structure that is robust and well-defined both as the packet leaves the source region and also as it propagates towards a remote interaction region. The efficient design of mechanical wave forcing has been examined by Slinn & Riley (1998*a*). By analyzing the *linearized* equations of motion augmented with forcing, they found that for the envelope of the emerging signal to be steady and uniform in shape, the vertical extent of the forcing region has to be larger than one vertical wavelength. When the forcing region is narrower than a vertical wavelength, the emitted signal is modulated by an irregular, non-constant envelope. Additional challenges for maintaining a robust spatial structure are brought about when large wave amplitudes are required due to the resulting enhanced wave dispersion with respect to a small amplitude wave Winters & D'Asaro (1989).

As we will illustrate in chapter (6), by means of residual mean flow generation and its subsequent interaction with the propagating wave, highly nonlinear effects can also produce significant distortion and weakening of a large-

amplitude wave packet that is strongly localized in the vertical. Such effects are highly undesirable when large wave amplitude is a necessary condition for IGW breaking to occur in any of the interaction scenarios described in section (1.7).

The formation of residual mean flow in the generation region of numerically simulated IGWs has been observed (although not reported) by Slinn and Riley who focused on the study of the reflection of IGWs off a sloping boundary and used forcing terms identical to those we consider in this thesis Slinn & Riley (1998*a*,*b*). A rotated coordinate system was employed to allow for periodic discretization of the up-slope direction. A Rayleigh damping/sponge layer aligned with the top boundary of the domain enabled the absorption of the residual mean flow which was oriented in the along-slope direction, normal to the gravity vector (D.N. Slinn, personal communication). Although sponge layers can potentially remove the mean flow, they are computationally expensive as they tend to be rather thick and consume a large number of grid points (e.g. $O(10\%)$ of the grid points in the slope-normal direction Slinn & Riley (1998*a*)).

Issues of residual mean flow generation were later reported by Zikanov & Slinn (2001) for a similar flow configuration but with three-dimensional forcing introduced to reproduce the oblique incidence of IGWs on a sloping boundary thereby allowing the formation of an along-slope current. During the initial transient adjustment phase of the simulations, before the wave reached the bottom slope, a mean flow, transitory in nature, was observed in the along-slope direction at the propagating front of the wave and explained on the basis of the local transient change in Reynolds stress in front of the wave. Another along-slope mean flow, non-propagating in nature (i.e. residual flow), was also gener-

ated in the forcing region in a direction opposite to that produced at the wave front and was attributed to the Reynolds stress gradient in the slope-normal direction which is caused by the growth of the wave as it passes through the forcing region. This residual mean flow component appeared to resist further downward propagation of the wave and thus had to be removed.

1.9 Generation of internal gravity waves by turbulence

The radiation of IGWs from turbulent mixed layers into a surrounding stably stratified fluid (e.g. IGWs emitted from the boundary layer on the earth's surface to the atmosphere) has been identified as a potential source of IGW generation in the ocean and atmosphere since the early work of Townsend (1959, 1965, 1968). More recently, Wijesekera & Dillon (1991) observed IGWs propagating down through the pycnocline in the equatorial Pacific after sunset, presumably caused by convective overturning turbulent motions in the surface mixed layer resulting from a variety of sources such as surface cooling, wind forcing, and storms. There are, however, insufficient systematic observations of the spectral characteristics or the energy flux associated with such waves (Thorpe, 2005). Reliable estimates of the energy flux associated with small scale IGWs can provide insight into the significance of their role in mixing the ocean interior and their impact on large scale circulation models in the atmosphere.

Shear flow instabilities leading to transition and turbulence have also been suggested as a source of the observed internal waves at high altitudes in the mesosphere and upper stratosphere (Davis & Peltier, 1979; Holton, Haynes, McIntyre, Douglas, Rood & Pfister, 1995; Sutherland, Caulfield & Peltier,

1994). Moum, Hebert, Paulson & Caldwell (1992) also suggest that the equatorial undercurrent is a main source of internal waves that drive mixing in the thermocline.

Laboratory scale experiments with grid generated turbulence in uniformly stratified fluids played a key role in improving our understanding of the process of internal wave radiation by stratified turbulent flows and the spectrum of the radiated waves. Linden (1975) experimentally studied the deepening of a turbulent region set up by the vertical oscillation of a horizontal grid at the top of a tank containing a uniformly stratified fluid. IGWs were radiated from the base of the mixed layer towards the underlying linearly stratified region, with typical phase line angles to the vertical around 35°. He estimated that significant energy was lost to wave radiation that the rate of deepening of the mixed layer was significantly reduced. To the contrary of this result, by performing similar experiments on a uniformly stratified fluid and a two layer fluid (two initially unmixed homogeneous fluid layers with different densities where IGWs are not supported), Xue-Quan & Hopfinger (1986) found that the entrainment rate was not affected by the wave radiation.

Sutherland and collaborators (Sutherland & Linden, 1998; Sutherland, Dalziel, Hughes & Linden, 99; Dohan & Sutherland, 2003; Flynn & Sutherland, 2004; Dohan & Sutherland, 2005; Aguilar & Sutherland, 2006; Aguilar, Sutherland & Muraki, 2006; Munroe & Sutherland, 2008) used a novel synthetic schlieren technique (Dalziel, Hughes & Sutherland, 1998; Sutherland, Dalziel, Hughes & Linden, 99; Dalziel, Hughes & Sutherland, 2000) to visualize and measure the local amplitude of IGWs generated by turbulence on two dimensional vertical planes and record its evolution over time. The technique relies on the variation

of the index of refraction of light as a result of local variations in the density gradient field caused by the local stretching and compressing of the isopycnal surfaces by the propagating waves.

Sutherland & Linden (1998) examined the shear excitation of IGWs by performing experiments in which an unstable shear layer in a nearly mixed top region flowed over a thin vertical barrier in the center of a tank. Instabilities in the lee of the barrier and small scale turbulence led to excitation of IGWs from the base of the mixed region down towards a strongly stratified region. The phase tilt of the waves with respect to the vertical θ was found to be in the $45 - 60^\circ$ range. They estimated that the wave momentum transported by the waves lead to deceleration of the mean flow by approximately 7% of its characteristic flow speed, a result that was nearly consistent with a two dimensional numerical simulation they used to complement their experimental results. Based on the prevalence of waves in the $45 - 60^\circ$ range and the results of their numerical simulations in which they observed significant changes in the dynamics of the mixed region when strong wave radiation occurred, they suggested that IGW excitation is a result of highly nonlinear feedback between the waves and the mixed region. Accordingly, the selection of waves in a narrow propagation angle range around 45° is based on the capability of such waves to strongly modify the mixed region and causing the maximum drag on the mean flow.

Dohan & Sutherland (2003, 2005) performed experiments and numerical simulation to study IGW excitation from a stationary turbulent mixed region (i.e. turbulence with no mean flow) at the top of a uniformly stratified region.The turbulence was created by the vertical oscillation of a horizontal grid. As the observed waves were predominantly in a very narrow angle range ($45 \pm 5^\circ$), the

angle at which the waves would carry the maximum horizontal momentum away from the turbulent region, they suggested that wave excitation is a result of a highly nonlinear wave-turbulence interaction. Interestingly, Aguilar, Sutherland & Muraki (2006); Munroe & Sutherland (2008) performed similar experiments, however, with a moving source of turbulence created by dragging a wooden object with a square wave form at the top of a uniformly stratified region. The separated flow and the eddies shed in the lee of the steep square-shaped wave form were found to excite IGWs that propagate down towards the stratified region in an angle range close to 45° which leads them to conclude that the properties of turbulence generated IGWs are universal, i.e. independent of the forcing mechanism.

Using large eddy simulation (LES) Taylor & Sarkar (2007) simulated IGW excitation by a turbulent bottom Ekman layer underlying a uniformly stratified outer layer. Turbulence in the boundary layer lead to the excitation of horizontally moving IGWs inside the pycnoline that forms above the turbulent mixed region during the simulation. Vertically propagating IGWs were also radiated towards the outer layer with angles in the $(35-60^{\circ})$ range. They propose a viscous-decay-based model to explain the prevalence of a relatively narrow wave frequency peak in about eight boundary layer thickness distance through the outer layer. The model is sensitive to the initial distribution of amplitudes of the wave component frequencies but nevertheless is capable of capturing the prevalence of wave angles bigger than 26° in agreement with the angles predicted from the simulations. By vertically integrating the evolution equation for the turbulent kinetic energy they found that the vertical energy flux carried by the waves, although it represents only a few percent relative to the dissipation rate, is comparable to the average buoyancy flux.

Finally, Pham, Sarkar & Brucker (2009) performed direct numerical simulations (DNS) of an unstable shear layer in a weakly stratified region overlying a strongly stratified region. Strong amplitude IGWs were initially excited by the Kelvin-Helmholtz (KH) rollers with propagation angles that agreed with linear theory arguments based on a Doppler-shifted KH mode frequency. Weaker waves with relatively broad spectrum near their generation region were subsequently excited by small-scale turbulence; however, far from their generation sites the propagation angle were concentrated around 45°. They finally show that momentum flux carried by the waves can be as large as 10% of the initial shear layer momentum and that the vertical flux of energy extracted from the shear layer by the propagating waves can be as large as 17% of the turbulent production and 75% of the buoyancy flux and hence the dynamics of the shear layer can be significantly affected by IGW radiation.

1.10 Wake generated internal gravity waves

Stably stratified turbulent wakes are another fundamental fluid flow of relevance to environmental and ocean engineering applications where emission of IGWs by turbulence is observed. Geophysical examples include the oceanic wakes of islands (Tomczak, 1988), headlands (Pawlak, MacCready, Edwards & McCabe, 2003) and seamounts (Gibson, Nabatov & Ozmidov, 1993) and the atmospheric wakes of mountains (Rotunno, Grubisic & Smolarkiewicz, 1999). Such wakes are potent agents of across and along-isopycnal transport and mixing of energy, heat and biogeochemical constituents not only near the wake source but also over significant distances away from it (Diamessis, Spedding

& Domaradzki, 2010*b*). From an ocean engineering perspective, underwater vehicles operate most efficiently in the pycnocline of the open or littoral ocean.

The ambient stratification, however, has a unique effect on the vehicle wake through the formation of distinct late-time, large aspect ratio quasi-horizontal/pancake vortices and the radiation of internal waves both by the vehicle and its turbulent wake (Schooley & Stewart, 1963; Lin & Pao, 1979; Gilreath & Brandt, 1985; Hopfinger, Flor, Chomaz & Bonneton, 1991; Lin, Lindberg, Boyer & Fernando, 1992; Bonneton, Chomaz & Hopfinger, 1993). Thus, the wake may establish a distinct late-time signature that may potentially be traced directly to the generating body. Internal gravity waves generated by a turbulent wake inside or below the pycnocline, can propagate towards the surface and leave a signature that can be detected by satellite optical imagery from space, such as the sea surface brightness anomalies reported in Keeler *et al.* (2005), that were detected far from a submerged turbulence source (a buoyant municipal outfall wastewater field) in the Sand Island, Honolulu. Unlike internal waves generated by turbulence in a well-mixed region (see §1.9), waves generated by a turbulent wake in a uniformly stratified fluid provides a unique physical setting where turbulence and buoyancy forces, caused by the stable stratification, are directly interacting.

Theoretical moving point source models by Miles (1971) and Lighthill (1978) developed specifically for the body generated waves proved successful in qualitatively predicting the phase line geometry downstream of an obstacle and outside its wake region (Peat & Stevenson, 1975; Chashechkin, 1989). The wake generated IGW field, however, was first investigated by Gilreath & Brandt (1985) who conducted one of the earliest experiments that analyzed in detail

the properties of the random wave field behind a self-propelled body inside a stably stratified fluid. They observed three types of waves in the wake of the body. The first type is a deterministic (in the sense of being repeatable in detail) body-generated lee wave, the second type is generated by the swirling motion of the propeller and is also deterministic, however transient, in nature. The third type was a random like field of waves that occurred during what they called "the collapse" of the wake under the influence of buoyancy forces.

Using a series of shadowgraph images they estimated the r.m.s. of the heights of turbulent puffs/bursts at the convoluted wake boundary and showed that, under the influence of buoyancy, they "collapse", in the sense of reaching a nearly constant value, upon initial violent growth in the near field. They further hypothesized that the turbulent kinetic energy is transferred back to potential energy and hence to the observed random internal wave field when a local turbulent Froude number (based on the r.m.s. turbulent velocity and the turbulent integral scale) approaches unity. In an attempt to isolate the different components of the wave field, they found that the linear theory successfully predicted the body-generated/lee waves but failed to accurately predict the two other components. They remarked that the process of IGWs generation in the wake of the body is inherently nonlinear although the subsequent propagation of the waves may possibly be represented by linear theory. Accordingly, they concluded that a fully nonlinear numerical simulation is needed to accurately resolve the complex process of generation and emission of the random component of the wave field.

Using a novel laser induced fluorescence technique (see Hopfinger *et al.*, 1991) to measure the dispalacement of isopycnal surfaces in a horizontal plane out-

side the turbulent region caused by the passing of IGWs , Bonneton, Chomaz & Hopfinger (1993) found that the observed IGW field transitions from a lee-wave ($Fr \lesssim 4.5$) to a random-wave dominated field ($Fr \gtrsim 4.5$), independently of Reynolds number, at least in the range covered by their experiments ($380 < Re < 30,000$). By tracking the evolution of the wave field on a horizontal plane below the center line, it was clear that the wave emission persisted for much longer for an experiment where Reynolds number was increased by a factor of 10 at the same Froude number. They suggested that the wave motion at high Reynolds number possesses more energy than at low Reynolds numbers.

The vertical displacement amplitude of the lee waves measured by Bonneton *et al.* (1993) decayed like $1/F$, in agreement with the linear theory, whereas the random wave field's amplitude grew according to a purely empirical $\sim Fr^2$ law with a cross-over of the amplitude of the two types of waves, where the random wave field starts to dominate the measured wave field, occurring at $Fr \approx 4.5$. As Re in their experiment (where the velocity of the sphere is the only parameter that is varied between different experiments) is proportional to Fr through $Re = Re(1)\, Fr$ where $Re(1)$ is the Reynolds number corresponding to $Fr = 1$; the effects of Fr and Re are not isolated. They nevertheless argue that Re dependence should be weak as it should be proportional to the scale of the energy containing eddies at the onset of collapse that is Re independent.

Finally, with a large scatter in the measured horizontal wavelengths, they show that the wavelength of the random wave field, in agreement with the impulsive wave source theory, decays roughly as $1/Nt$ which somehow appears to overestimate a dominant inferable decay rate regardless of the large scatter found in

their data. The waves that arrived first at the measurement plane had a wavelength $\lambda_H = 4R$ and the angle that isophase lines made with the vertical θ was $= 55^\circ$; that is the angle that maximizes the displacement amplitude according to Lighthill's theory for internal waves generated by a point disturbance Lighthill (1978) and Zavol'Skii & Zaitsev (1984). By plotting the energy spectrum of the vertical velocity at a fixed downstream location, they further show there is a dominant frequency corresponding to a Strouhal number, close to that of the spiral mode of the wake, $St = 0.17$, at which the random waves are emitted, presumably by periodically generated turbulent bursts.

For a non-uniformly stratified fluid, Robey (1997) performed experiments to investigate the internal wave field generated by a sphere towed below a thermocline. In agreement with Bonneton *et al.* (1993), where the stratification was uniform, he determined a similar transition Froude number $Fr = 4$ between the lee wave and the random wave dominated regimes. In addition to the experiments, he developed a numerical model based on the linearized equations of motion by including a distribution of sources and sinks which requires knowledge of the source geometry (diameter and length) and its speed for its initialization. For the wake generated random waves, he assumed the source to be a large scale turbulent eddy. He estimated the eddy length, diameter and velocity scales based on resonance arguments ($Fr_{eddy} = 2\pi\, U_{eddy}/NL_{eddy} = 1$).

Specifically, he assumed a Strouhal number $St = 0.2$ along with unstratified wake scaling to estimate the characteristic eddy diameter and velocity. He found that the resonant eddies are actually located in the near field justifying the use of unstratified wake scaling laws. It is perhaps perplexing and self-contradictory that the resonant eddies can be claimed to occur in the near wake

were the turbulence is presumably active at all scales especially at high enough Re and Fr which is the case in many of his reported experiments. By initializing the numerical model using the characteristics of the resonant eddies, he found that the numerically calculated wave amplitudes are in reasonable agreement with the experimentally determined amplitudes. Unlike the Fr^2 scaling for the random wave field obtained by Bonneton *et al.* (1993) he found that the slope was indeed closer to linear than a quadratic.

CHAPTER 2

SCOPE AND OBJECTIVES OF THE THESIS

2.1 Working hypotheses

The research work for this thesis is motivated by the more general need for understanding the dynamics of generation, propagation and breakdown of IGWs in the ocean and atmosphere. The dynamics of these processes often exhibit highly nonlinear and complex wave-wave, wave-shear flow, wave-turbulence interactions in the presence of non-uniform stratification. Accordingly, fully nonlinear controlled numerical simulations of the governing equations over as broad range of scales as possible become a must. The notion of a controlled numerical simulation derives from the additional advantage that numerical simulations offer over experimentation, that is the ability to easily vary certain parameters independent of each other; isolate the effects of certain parameters or individual processes that often coexist in the laboratory; and lessen the impact of undesirable processes on the main phenomena being studied.

The specific context in which we seek to understand these dynamics is the random wave field generated in the stratified turbulent wake of moving vehicles (such as submarines) in the ocean or bottom topography (seamounts). It constitutes half of the research work presented in this thesis. The robust understanding of the highly nonlinear processes leading to the generation of these waves, at operationally and oceanographically relevant conditions, and the accurate characterization of their properties (space and time scales; group velocities, amplitudes and potential for breaking) can bear significant implications on the detectability of these vehicles. From an oceanography point of view,

understanding internal wave generation by turbulence and accurate quantification of the energy flux associated with these waves enables assessment of their role in the evolution of the turbulence itself and also their impact on large scale circulation models.

2.2 Open questions: Wake-generated internal gravity waves

The first half of this thesis is thus mainly concerned with the numerical simulation of the IGWs that are generated by the turbulent wake of a towed body in a stratified fluid and the accurate characterization of their properties. Section (1.10) has already shed some light on the shortcomings of the few available, mainly experimental, studies that focuses on the random wave field component of the wake generated waves, namely:

- Interpretation of the results often relies on the use of simplified models such as the impulsive wave theory and the linearized source sink type models that are often initialized using ad-hoc assumptions about the underlying structure and dynamics of the wave generating source.
- The absence of a systematic study that isolates the effects of Re and Fr. Usually the two parameters are related in the laboratory experiments as they rely on varying either the characteristic length scale or the velocity of the towed body which changes both parameters at the same time.
- The need for pushing the envelope with the maximum attainable Re and Fr is often dictated by the available laboratory space. Specifically there is a need to test the hypothesis that wave emission at high Re can be stronger and more prolonged relative to a lower Re experiment, as a result of the

establishment of a prolonged highly energetic NEQ regime that was recently confirmed by the numerical simulations of Diamessis *et al.* (2010*b*).

- Since the IGW field emitted by the turbulence is random-like it comprises many wavepackets with different sizes, component wavelengths, amplitudes and orientations that constantly interfere with one another leading to changes in their amplitudes, scales, two issues have to be addressed that do not seem to have been adequately addressed by the limited body of literature that focuses on these waves:

    1. Characterizing the random-wave field should be based on the statistics of the desired quantities that are derived from a representative ensemble that is sampled over as large a part of the domain as possible. Hence reporting the wave properties at one spatial location/time is meaningless as it does not ensure repeatability over identical realizations of the flow of the reported quantities.

    2. Only energetically dominant wavepackets need to be sampled. Weak waves will quickly decay close to their generation sites and hence do not represent the characteristics of the waves which will eventually be radiated into the surrounding medium.

- Fourier transforms have been extensively used in many of the studies reviewed in section (1.10,1.9) to breakdown the measured signal into its Fourier components. Since the Fourier transform is based on globally defined trigonometric basis functions, it is implied that the measured signal can at least be approximated as quasi-periodic in both space and time. Periodicity of the signal in turn implies that the wave source is infinitely large in size and is persistent over time; two conditions that are clearly violated especially for wake generated waves, as the turbulence

(i.e. the source of the waves) is localized in space and is decaying over time (The transitory nature of the forcing is even more so at the low *Re* where wave radiation occurs only during a fraction of the relatively short NEQ regime). Continuous wavelet transform (CWT) is the most suitable candidate tool for the analysis of localized signals as they are naturally based on localized basis functions (Addison, 2002).

2.3 Open questions: Numerically forced internal gravity waves

The second half of the thesis focuses on understanding the intricate dynamics of IGW interactions with their environment. Specifically, wave steepening and breakdown near a critical level was the original motivation for this investigation. The first natural step towards achieving this ultimate goal is to implement a numerical wave forcing that will generate a large amplitude IGW packet with well-defined characteristics (wavelength, frequency, group velocity..etc) that preserve its structure and amplitude both near its generation site and during its propagation towards the interaction region. The mechanical forcing approach (Slinn & Riley, 1998*a*) seems to be one of the best possible candidate techniques that is especially suitable for high-order spectral element based codes such as the one used in this thesis.

As we are going to demonstrate in chapter (6), we found that the generated IGW packet gets progressively distorted near its rear end and its amplitude gets weaker through the generation of a localized residual horizontal mean flow component in the forcing region that non-linearly interacts with the prop-

agating wave packet and leads to modulations of its structure and decay of its amplitude. This phenomenon has only been recently reported by Zikanov & Slinn (2001) who did not give clear explanation for its underlying cause as it was not the focus of their study. It remained unclear as to why the formation of residual mean flow component appears to have been overlooked by the existing body of literature on the dynamics of IGWs. We argue that:

1. As most of the previous theoretical studies focused on either plane or quasi-plane IGWs, it is reasonable to assume that the main driver for the generation of a localized mean flow component is the strong vertical localization.
2. The reason why it is hard to observe such a mean flow in the laboratory is because wave tanks often have lateral boundaries and thus the formation and sustenance of a mean horizontal flow is not possible.
3. Another potential reason for the lack of experimental evidence is that waves generated in the laboratory are localized in the horizontal as well as in the vertical whereas the forcing we are focused on is horizontally periodic. For a localized wavepacket a mean flow can only exist over the horizontally limited extent of the wavepacket and hence the effects of horizontal localization on the formation of a residual mean flow need to be investigated.

2.4 Specific objectives: Wake-generated internal waves

The first half of the thesis focuses on the wake-generated IGWs. The primary objective of the study is to investigate the generation and evolution of the IGW

field emitted by the turbulent wake of a towed sphere in a uniformly stratified fluid and the possible connection between the wake evolution during the NEQ and the Q2D regimes and the observed characteristics of the emitted waves during the respective stages. Specifically, we aim to determine the characteristics of the wake emitted IGWs (length scales, frequencies, vertical group velocities and amplitudes) in the near field of the turbulent wake. We will use the two dimensional Arc and *Morlet2D* CWT techniques discussed in chapter 4 and capitalize on their inherent capabilities of optimally revealing simultaneous space-scale information to understand the spatial distribution of waves at different scales and the temporal distribution of the frequencies/propagation angles of such waves. The study is mainly driven by the following fundamental questions that have not been systematically studied in previously reported experiments and numerical simulations, namely:

- What is the effect of Re and Fr on the observed characteristics of the waves? Specifically, how are the initial wave length scales and frequencies and their subsequent decay rates depend on both parameters? In addressing this question, it is of interest to cover a broad range of Re and Fr which enable conservative extrapolation of the results to navally relevant operating conditions of under water vehicles and to be able to vary one parameter independent of the other.
- Will the prolongation of the NEQ regime and the occurrence of instabilities and intermittent turbulent events in the late Q2D regime at high Re (recently verified, numerically, by Diamessis *et al.* (2010*b*)) lead to a concomitant prolonged wave emission relative to a low Re simulation?
- Are there preferred propagation angles? If indeed there are preferred directions, how could their selection be explained? and how do they de-

pend on Fr and Re?

- What is the potential for breaking of the emitted waves and how dependent is it on Re and Fr?

2.5 Specific objectives: Numerically forced internal gravity waves

In this study, we focus on the second main theme of the thesis; the forced numerical generation of internal gravity waves with predefined characteristics. So far, no systematic study has been published, which is aimed towards understanding the underlying cause of residual mean flow formation associated with generation of large amplitude IGW packet that is strongly localized in the vertical, its impact on the long-time evolution of the wave field and the identification of possible mean flow containment mechanisms. Most previous numerical studies have focused on the interactions between wave and wave-induced mean flow for quasi-plane moderate to large amplitude IGW packets introduced as initial conditions (Sutherland, 2001, 2006*a*,*b*). Thus, our fundamental working hypothesis is that additional nonlinear effects may emerge when combining strong vertical localization, large wave amplitude and possibly finite duration forcing all of which may force strong adjustment of the solution of the fully nonlinear governing equations away from their linear counterpart and, as a result, may non-trivially alter the subsequent evolution of the wave field.

We first examine the near-source distortion of a forcing-generated vertically localized IGW packet as a function of stratification strength and degree of hor-

izontal localization. Motivated by the insight originally offered by Zikanov & Slinn (2001), we then use scaling arguments to identify the dependence of the magnitude of the associated mean flow on wave steepness, degree of vertical localization and degree of wave hydrostaticity. The understanding gained enables the design of efficient mean flow-containment techniques which allow the mechanical forcing-driven numerical generation of a well-defined IGW packet which can propagate robustly towards a nearby interaction region. The effectiveness of the proposed techniques is demonstrated through their application to the simulation of the critical level interaction of an IGW packet.

Since mechanical forcing is directly generalizable to the generation of continuously forced IGW trains, the relevance of our findings to continuously forced numerical simulations and the laboratory is also discussed. Finally, the question is posed whether a robust large-amplitude, vertically localized IGW packet can indeed be generated and, moreover, propagate sufficiently far from its origin in the atmosphere or ocean while maintaining its original structure and amplitude.

CHAPTER 3

SPECTRAL MULTIDOMAIN PENALTY SOLVER BASICS

3.1 Governing Equations

We are primarily interested in examining the dynamics of generation, evolution and propagation of IGWs in a uniform stably stratified fluid. The excitation of the waves will be studied in two contexts:

1. "Natural" excitation through what is believed to be resonance between the turbulent eddies and the stratified medium in which they exist (Gilreath & Brandt, 1985; Robey, 1997).
2. "Forced" excitation where a modelled wave generator imparts a periodic force to the medium.

The governing equations in both contexts are the Navier-Stokes equations under the Boussinesq approximation :

$$\frac{\partial \mathbf{u}}{\partial t} = \underbrace{-\frac{1}{2}[\mathbf{u}\cdot\nabla\mathbf{u} + \nabla(\mathbf{u}\,\mathbf{u})] + \mathbf{F}_g}_{\mathbf{N(u)}} - \frac{1}{\rho_0}\nabla p' + \nu\underbrace{\nabla^2\mathbf{u}}_{\mathbf{L(u)}} \quad , \tag{3.1}$$

$$\frac{\partial \rho'}{\partial t} = -\nabla\cdot(\mathbf{u}(\rho' + \overline{\rho}(z))) + \kappa\nabla^2(\rho' + \overline{\rho}(z)) \quad , \tag{3.2}$$

$$\nabla\cdot\mathbf{u} = 0, \tag{3.3}$$

$$\text{where} \qquad \mathbf{F}_g = -g\frac{\rho'}{\rho_0}\hat{\mathbf{k}}. \tag{3.4}$$

The non-linear term ($\mathbf{N(u)}$ in 3.1) is written in the skew-symmetric form to minimize aliasing effects in the numerical solution (Boyd, 2001). The quantities p'

and ρ' are the perturbations of the pressure and the density from their respective (mean) reference values, which are in hydrostatic balance (see Diamessis *et al.* (2005)). In the first context, the governing equations are not modified and the wave generation occurs during the evolution of the solution from a set of initial conditions representing a turbulent wake flow behind a towed sphere (see chapter 5 for details). In the second context, the right hand side of the momentum and density equations are supplemented by wave generating forcing terms $F_{\mathbf{u}}, F_\rho$.

As a result of the Fourier spatial discretization in the horizontal direction(s), the boundary conditions are limited to periodic velocity and density fields; an assumption that will be justified and elaborated on in the context of the individual simulations being discussed. Mathematically this is expressed as (assuming a three dimensional rectangular computational domain):

$$(u, v, w, p', \rho'))(x, y, z, t) = (u, v, w, p', \rho')(x + L_x, y, z, t), \tag{3.5}$$

$$(u, v, w, p', \rho'))(x, y, z, t) = (u, v, w, p', \rho')(x, y + L_y, z, t), \tag{3.6}$$

where L_x and L_y are the dimensions of the rectangular computational domain in the (horizontal) x, y directions, respectively. Also, in all the simulations reported in this thesis, the bottom boundary is a solid wall with a no-slip boundary condition:

$$u(x, y, 0, t) = 0, \quad v(x, y, 0, t) = 0, \quad w(x, y, 0, t) = 0 \ , \tag{3.7}$$

whereas the top boundary is a free-slip (stress-free) non-deformable surface:

$$\left.\frac{\partial u}{\partial z}\right|_{(x,y,L_z,t)} = 0 \ , \quad w(x, y, L_z, t) = 0 \ , \tag{3.8}$$

(L_z being the domain height) and finally the density perturbations are assumed to vanish at both vertical boundaries:

$$\rho'(x,y,0,t) = \rho'(x,y,L_z,t) = 0 \ . \tag{3.9}$$

In the next section we review the basics of the numerical solver used in the study. We first discuss the splittng algorithm for solving the system of governing equations. We then elaborate on the spatial and temporal discretization and then summarize the stabilization techniques employed by the solver to deal with the typically under-resolved simulations of high Reyonlds number flows.

3.2 Temporal discretization scheme

For the temporal discretization of eqs. (3.1)-(3.3), a high-accuracy pressure projection scheme is used (Karniadakis, Israeli & Orszag, 1991). According to this scheme, if one integrates eqs. (3.1)-(3.3) in time from level t_n to t_{n+1} the following semi-discrete equations, decomposed into three fractional steps for $\tilde{\mathbf{u}}$, are obtained (Diamessis, Domaradzki & Hesthaven, 2005):

$$\frac{\hat{\mathbf{u}} - \sum_{q=0}^{J_i-1} \alpha_q \mathbf{u}^{n-q}}{\Delta t} = \sum_{q=0}^{J_e-1} \beta_q \mathbf{N}(\mathbf{u}^{n-q}) \ , \tag{3.10}$$

$$\frac{\hat{\tilde{\mathbf{u}}} - \hat{\mathbf{u}}}{\Delta t} = -\nabla \phi^{n+1} \ , \tag{3.11}$$

$$\frac{\gamma_0 \mathbf{u}^{n+1} - \hat{\tilde{\mathbf{u}}}}{\Delta t} = \nu \mathbf{L}(\mathbf{u}^{n+1}) \ . \tag{3.12}$$

The values of the coefficients α_q, β_q and γ_0 for the 3rd order backward differentiation-stiffly stable (BDF3-SS3) scheme of equations (3.10)-(3.12) may

be found in Karniadakis *et al.* (1991). The quantity ϕ^{n+1}:

$$\int_{t_n}^{t_{n+1}} \nabla p' dt = \Delta t \nabla \phi^{n+1} \quad . \tag{3.13}$$

is an intermediate scalar field that ensures that the final velocity $\mathbf{u}^{n+1}$ is incompressible. In eq. (3.11), it is assumed $\nabla \cdot \hat{\hat{u}} = 0$ and the Poisson equation is solved for the pressure:

$$\nabla^2 \phi^{n+1} = \nabla \cdot \left(\frac{\hat{\mathbf{u}}}{\Delta t} \right) \ . \tag{3.14}$$

The boundary conditions for $\tilde{\mathbf{u}}$ (3.7)-(3.8) are enforced in eq. (3.12). Equation (3.14) utilizes the high-order accuracy dynamic boundary condition (Karniadakis, Israeli & Orszag, 1991):

$$\left. \frac{\partial \phi^{n+1}}{\partial z} \right|_b = \left. \sum_{q=0}^{J_e-1} \beta_q \mathbf{N}(w^{n-q}) \right|_b - \left. \sum_{q=0}^{J_e-1} \beta_q [\nu \nabla \times (\nabla \times w)]^{n-q} \right|_b \ . \tag{3.15}$$

where $|_b$ denotes $z = 0, H$ and the coefficients β_q have the same value as in the SS3 scheme of eqs. (3.10)-(3.12).

The splitting procedure for ρ' consists of two steps analogous to eqs. (3.10) and (3.12). The boundary conditions (3.9) are enforced in the corresponding diffusive step.

This splitting approach combines third-order stiffly stable and backward-differentiation schemes with a dynamic high-order boundary condition for the pressure. Thus, $O(\Delta t^2)$ is ensured for the velocity and the pressure (Guermond & Shen, 2003) and the maximum possible value of stable timestep is attainable (Karniadakis, Israeli & Orszag, 1991).

For a given simulation, the initial computational timestep Δt is chosen as such

that the CFL stability criterion is obeyed in all three spatial directions for a 3rd order stiffly stable scheme. The following requirements are imposed:

$$\Delta t\frac{u_{max}}{\Delta x} < 0.18, \quad \Delta t\frac{v_{max}}{\Delta y} < 0.18, \quad 0.7 < \Delta t\left[\frac{w}{\Delta z}\right]_{max} < 0.9 \ . \tag{3.16}$$

The particular choice of the initial time step depends on the minimum relevant physical time scale for the problem under consideration. For the towed sphere simulations reported in chapter 5, the initial time step is taken to be $\sim 3-4\%$ of the advection time scale D/U. The adaptive timestepping scheme is activated whenever the timestep reaches the lower or upper bound of the vertical CFL criterion and the timestep is increased or decreased by a factor of 1.25, respectively. In all of the problems considered in this thesis, the buoyancy period of the stratified medium is the maximum characteristic time scale and we thus set the maximum allowable timestep to be $\Delta t_{max} = 2\pi/(60N)$ to adequately resolve it.

3.3 Spatial discretization scheme

In the periodic horizontal direction, Fourier spectral discretization is used with $\hat{N}_x$ and $\hat{N}_y$ Fourier modes in the longitudinal and spanwise direction, respectively. In the vertical direction, the computational domain is partitioned into M subdomains of variable height H_k ($k = 1, \ldots M$) and fixed order of polynomial approximation $\hat{N}$ (see Fig. 3.1(a) and (b)). The total number of vertical grid points is $\hat{N}_z = M(\hat{N} + 1) + 1$. Within each subdomain, a Legendre spectral collocation scheme (Boyd, 2001) is used. Subdomains communicate with their neighbors via a simple patching condition (Diamessis, Domaradzki & Hesthaven, 2005). The multidomain scheme allows for increased resolution of vertically localized dynamic regions such as the core of the turbulent wake or

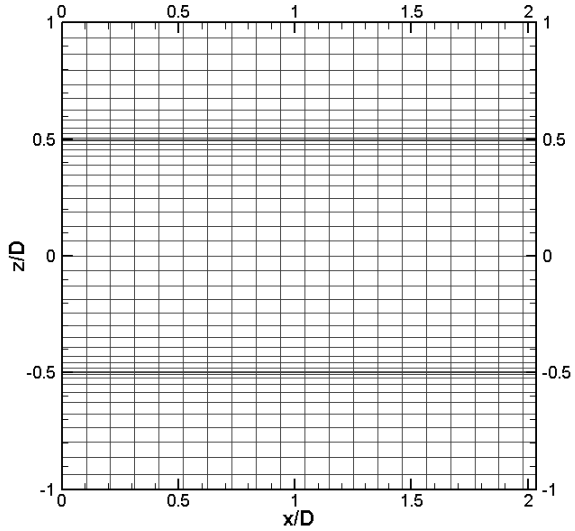

(a)

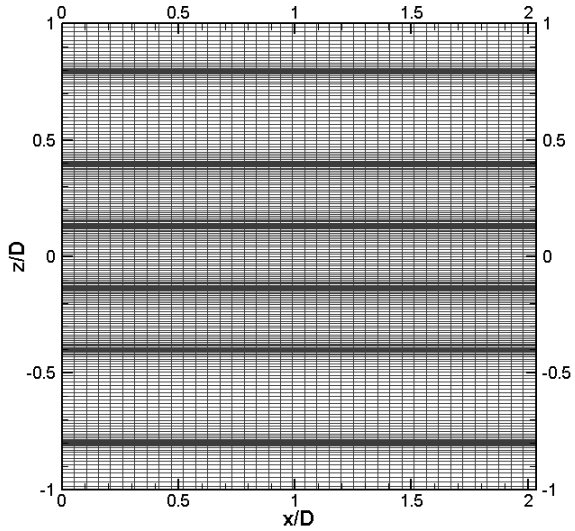

(b)

Figure 3.1: Exploded view of the wake core region of an Oxz section of the numerical grid employed in the simulations of a stratified turbulent wake at (a) $Re = 5 \times 10^3$ (where $M = 7$ subdomains of order of approximation $\hat{N} = 24$, with subdomain origins located at $z/D = -6, -3.17, -1.67, -0.5, 0.5, 1.67$ and 3.17) (b) $Re = 10^5$ (where $M = 13$ subdomains of order of approximation $\hat{N} = 40$, with subdomain origins located at $z/D = -6, -3.67, -2.33, -1.33, -0.8, -0.4, -0.13, 0.13, 0.4, 0.8, 1.33, 2.33,$ and 3.67).

the critical level region in the IGW shear flow interaction, while also resolving adequately, yet not excessively, the less active regions of the physical domain.

The resolutions used in this thesis aim to capture the dynamically relevant scales of motion while accommodating available computational resources and the need for rapid run turnaround. As a result, the available numerical resolution at higher Reynolds numbers is not sufficient to capture both the large, energy containing and small, dissipative scales of turbulence. With the bulk of the numerical resolution devoted to large scales, the effects of molecular viscosity which are active in the range of small, dissipative scales cannot be resolved. Attempts to solve Navier-Stokes equations in such a case will result in an underresolved simulation. When spectral schemes, which are inherently non-dissipative, are used in underresolved simulations, the resulting Gibbs oscillations are compounded by aliasing effects driven by the non-linear term, lead to catastrophic numerical instabilities (Gottlieb & Hesthaven, 2001).

To overcome such difficulties either the governing equations must be modified, e.g., by introducing an explicit subgrid-scale (SGS) model term as is commonly done in LES, or by modifying the numerical method of solution by introducing procedures that control and prevent numerical instabilities. We follow the latter approach using two techniques that are designed to ensure stability of the numerical solution while preserving high accuracy: explicit spectral filtering and penalty schemes.

3.4 Stabilization methods: spectral filtering and penalty techniques

Penalty methods consist of collocating a linear combination of the equation and boundary/patching conditions (the latter multiplied by a penalty coefficient) at the boundaries/subdomain interfaces, respectively (Hesthaven & Gottlieb, 1996; Hesthaven, 1997). A smooth transition from the subdomain interface to its interior is thus possible, enabling stable computation of the high *Re* "internal" (internal with respect to the subdomain boundary) dynamics of the flow without having to resolve the thin numerical/viscous physical boundary layers or internal sharp gradients at subdomain interfaces (Diamessis, Domaradzki & Hesthaven, 2005). Spectral filtering consists of the explicit application of an order p low-pass filter function to the spectral (modal) expansion of the solution. In this study, an exponential filter (Gottlieb & Hesthaven, 2001) is used:

$$\sigma(k) = \exp\left[-\alpha\left(\frac{k}{k_c}\right)^p \right] \tag{3.17}$$

where p is the filter order and $\alpha = -ln(\varepsilon_M)$ with ε_M being the machine precision. In Legendre space, the filter function $\sigma(k)$ multiplies the k-th Legendre modal coefficient and k_c represents the index of the highest resolved mode (see Fig. 3.2). In contrast, in Fourier space, for the purpose of implementing efficient two-dimensional filtering, k is elected to represent the magnitude of an individual Fourier wavenumber pair (k_x, k_y), i.e. $k = (k_x^2 + k_y^2)^{1/2}$ and k_c is chosen as $k_c \equiv [({k_{x,max}}^2 + {k_{y,max}}^2)]^{1/2}$, i.e. the maximum resolved Fourier wavenumber pair magnitude for the given domain dimensions. In terms of the temporal discretization summarized in §3.2, the penalty method is applied at two different levels (explicit advancement of nonlinear terms and implicit treatment of viscous terms) in the incompressible Navier-Stokes equations. Legendre spectral

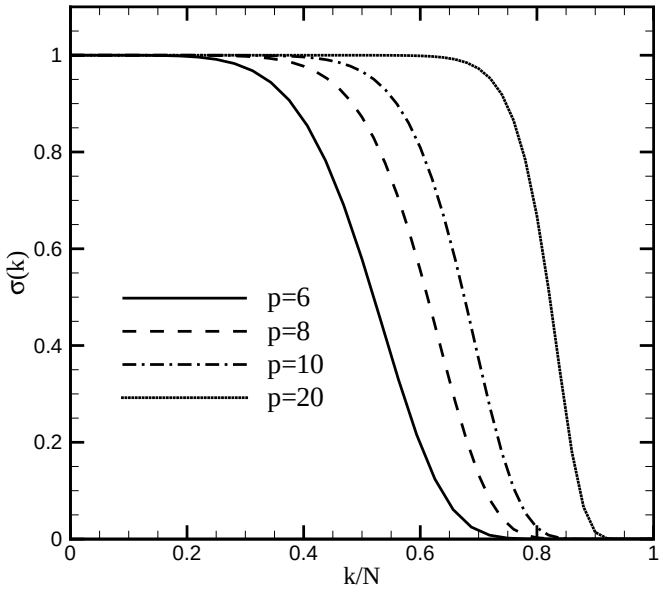

Figure 3.2: Exponential filter functions $\sigma(k/k_C)$ for the four different filter orders p = 6,8, 10, and 20 used in this study. In Legendre space, k and k_C represent the mode number and total number of available modes, respectively. In Fourier space, k and k_C represent the two-dimensional wavenumber vector magnitude and the corresponding maximum value over all resolved horizontal wavenumbers, respectively

filtering of the same order p is applied after all three fractional steps. Fourier spectral filtering is applied only after advancing the non-linear terms to suppress the accumulation of high-wavenumber numerical noise driven by aliasing. Legendre filters have a negligible influence at the subdomain interfaces (Gottlieb & Hesthaven, 2001), where the influence of the penalty method is the strongest. Thus, the two stabilizing techniques complement each other in enabling numerical stability through the entire extent of a spectral subdomain. As a final safeguard against numerical instability, adaptive interfacial averaging is used in the vertical direction (Diamessis, Domaradzki & Hesthaven, 2005).

The numerical technique employed in this thesis may be viewed as an implicit large eddy simulation, where the stabilization is not provided by the truncation error of the numerical discretization (which is exponentially small for a spectral method (Boyd, 2001)) but by the spectral filter, which may viewed as an intrinsic component of the numerical discretization in the case of under-resolved simulations. As with all large eddy simulation techniques, one must of course, be aware that simply guaranteeing numerical stability does not guarantee physically correct dynamics of the resolved scales. Therefore, the results of the simulations must be always compared with experiments and simulations, either fully resolved DNS, or LES performed with other models, to gain confidence that the method is not only numerically stable but also physically correct (Diamessis, Spedding & Domaradzki, 2010*b*).

CHAPTER 4

ON THE CONTINUOUS WAVELET TRANSFORM AND ITS USE IN FLUID MECHANICS

4.1 Spectral versus physical representation of signals

The purpose of spectral analysis is to breakdown a given signal into the relative contributions of its basic wavelength/frequency components. So, unlike proper orthogonal decomposition (such as the one described in (Diamessis, Gurka & Liberzon, 2010*a*)) where a signal is decomposed into a hierarchy of eigenmodes with arbitrary geometry, in spectral analysis, the signal is often decomposed into the sum of simple sinusoids with different weights/amplitudes. For the purpose of the following discussion we will assume that the signal is temporal rather than spatial such as a velocity time series measured at a point inside a fluid. The mathematical analyses are the same for both types of signals and the transforms developed are implemented in exactly the same way.

The Fourier transform has been used extensively in the field of signal and image processing to understand, breakdown and manipulate, if necessary, the frequency content of temporal signals. A Fourier transform pair representing the transform from the physical (spectral) to the spectral (physical) domain is defined as

$$F(\omega) = \frac{1}{\sqrt{2\pi}} \int_{-\infty}^{\infty} e^{-i\omega t}\, x(t)\; dt, \tag{4.1}$$

$$x(t) = \frac{1}{\sqrt{2\pi}} \int_{-\infty}^{\infty} e^{i\omega t}\, F(\omega)\; d\omega, \tag{4.2}$$

where $x(t)$ is the temporal signal and $F(\omega)$ is its Fourier transform. As the transform is only a function of the frequency, all time domain information is lost. As

such, the Fourier transform is not capable of finding where, in a signal, do certain component frequencies occur and hence it is mostly suited for stationary or periodic signals where the frequency content of the signal does not change over time. A song for example is a non-stationary signal where the frequency content changes dynamically as it progresses between high and low notes.

As a highly localized signal in the time domain corresponds to a broadband structure in the frequency domain, the requirement for a highly localized temporal signal precludes localizing in the frequency domain. This is the basis for the Heisenberg uncertainty principle in signal spectral analysis which simply means that obtaining a sharp resolution in the time domain is in competition with having a high resolution in the frequency domain. An intuitive extension to the Fourier transform that attempts to retain some of the time domain information is the Gabor transform (also called the short-time Fourier transform) introduced by Gabor (1946). The transform is based on modifying the Fourier transform kernel $e^{-i\omega t}$ by multiplying it by a localized function $g(\tau - t)$ (typically a Gaussian envelope with a characteristic width a) that acts to filter the temporal signal over a fixed window width (the Gaussian width a), that is

$$G(t, \omega) = \frac{1}{\sqrt{2\pi}} \int_{-\infty}^{\infty} e^{-i\omega\tau} g(\tau - t) x(\tau)\, d\tau. \tag{4.3}$$

As the parameter t is translated along the time axis one obtains a full time-frequency characterization $G(t, \omega)$ from each sub-window.

An obvious limitation to the Gabor transform is that its resolution in frequency is dependent on the window width a. The window width sets the maximum resolvable period by the Gabor transform. Simply, any spectral content with a period exceeding a will not be captured. In fact the uncertainty principle dictates that the shorter in time the window width is (and hence the higher the

time resolution is), the less frequency content will be retrievable.

The continuous wavelet transform (CWT) developed by Morlet & Grossman (1984) generalizes the ideas of translation and windowing in time of the Gabor transform by introducing an additional parameter into the transform; the window size or "scale" a. The window size/scale is varied over as broad a range as possible. The large scales capture the slow frequency components and the small scales capture the highly localized dynamical variations in the signal.

The CWT relies on a wavelet function $\psi(t)$ that satisfies certain mathematical properties. As the name suggests, a wavelet is a function that is localized in time. The function is translated along the time axis, stretched and compressed in scale and convolved with the signal $x(t)$ to unravel the signal's spectral content at all times and scales. There is a large number of wavelet functions to choose from for use in temporal data analysis. The wavelet function is designed such that it has properties that suit a particular subset of applications depending on the nature of the signal and the required manipulations. In the next section we review the mathematical underpinning of the CWT and the basics of its numerical evaluation.

4.2 Fundamentals of the 1-D continuous wavelet transform

The fundamentals of CWT are lucidly explained by Addison (2002) in a book that mainly addresses the applied science and engineering community. For a more detailed mathematical account of the subject, the comprehensive reference by Antoine *et al.* (2004) is highly recommended.

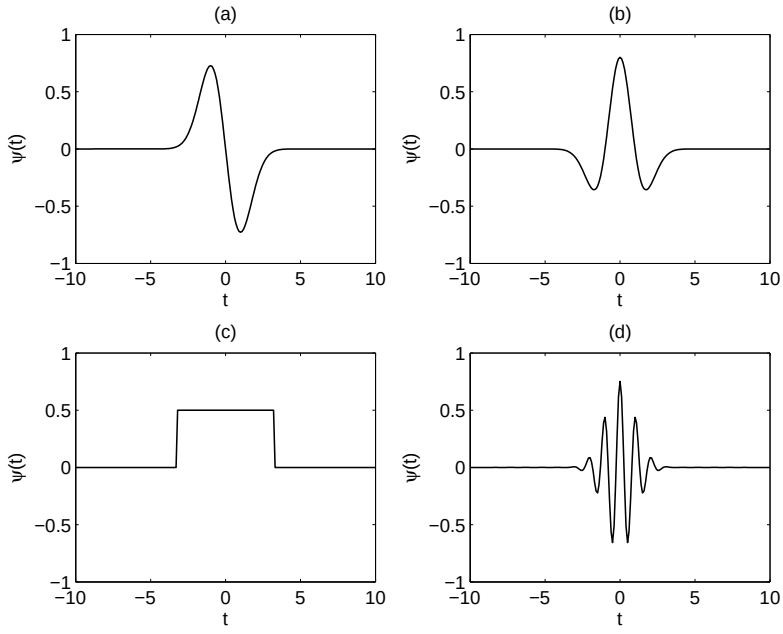

Figure 4.1: Examples of mother wavelets. (a) Gaussian wave (first derivative of a Gaussian). (b) Mexican hat (second derivative of a Gaussian. (3) Haar. (4) Morlet (real part)

Examples of wavelet functions (also called mother wavelets (Addison, 2002)) are illustrated in Fig. 4.1. The Morlet basis function is the most commonly used mother wavelet in the fluid mechanical applications as it can represent any frequently encountered localized wavepackets/disturbances with a well defined energetically-dominant length scale. It can be written as

$$\psi(t) = \frac{1}{\pi^{1/4}} \exp\left(i\, 2\pi f_0 t\right) \exp\left(-t^2/2\right), \tag{4.4}$$

where f_0 is the central frequency of the sinusoidal function which controls the number of oscillations contained within the Gaussian envelope. Two types of manipulations of the mother wavelet; translation and rescaling are illustrated in Fig. 4.2. Translation involves sliding the center of the wavelet along the time axis while rescaling involves stretching/compressing the wavelet over

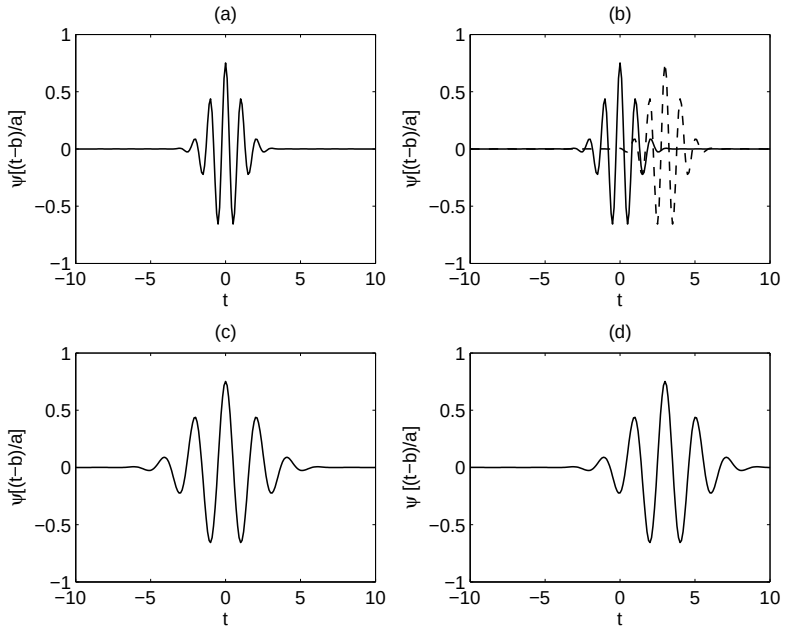

Figure 4.2: Basic manipulations of a Morlet mother wavelet. (a) Mother wavelet. (b) Translated wavelet. (c) Rescaled (dilated) wavelet. (d) Translated and rescaled wavelet.

the time axis without changing its shape. The manipulated wavelet is denoted $\psi\left[\left(t-b\right)/a\right]$ where b is the parameter representing the translation and the scale a is the parameter controlling the stretching and compressing of the mother wavelet. As the wavelet expands on the time axis (e.g. compare the wavelet in Fig. 4.2(c) to that in (b)) its spectral content contracts and hence the wavelet scale is inversely proportional to the wavelet characteristic frequency.

In order for a function to qualify as a wavelet it must meet certain mathematical criteria (Addison, 2002)

1. The wavelet must have a finite energy

$$E = \int_{-\infty}^{\infty} |\psi(t)|^2 \, dt < \infty, \tag{4.5}$$

2. The wavelet has to have a finite admissibility constant C_g

$$C_g = \int_0^\infty \frac{\left|\hat{\psi}(f)\right|^2}{f}\, df < \infty, \tag{4.6}$$

where $\hat{\psi}(f)$ is the fourier transform of the wavelet. This condition implies that the wavelet has no zero frequency component i.e. $\hat{\psi}(0) = 0$.

3. For complex wavelets (like Morlet), the Fourier transform must both be real and have a zero negative frequency content.

Now the CWT of a continuous temporal signal with respect to the wavelet function is defined as

$$T(a,b) = \frac{1}{\sqrt{a}} \int_{-\infty}^{\infty} x(t)\, \psi^* \left(\frac{t-b}{a}\right) dt, \tag{4.7}$$

where the asterisk denotes the complex conjugate of the wavelet function. In mathematical terms this is called a convolution. Addison (2002) describes the CWT as a "mathematical microscope" where b is the location on the time series being "viewed" and a is the magnification level. The inverse operation is then defined through

$$x(t) = \frac{1}{C_g} \int_{-\infty}^{\infty} \int_0^{\infty} T(a,b)\, \psi \left(\frac{t-b}{a}\right) \frac{da\, db}{a^2}, \tag{4.8}$$

which recovers the signal from its transform by integrating over all possible scales and locations. Limiting the integration to a subset of scales amounts to a basic scale-based filtering operation.

Computationally, the CWT is evaluated using the often analytically known Fourier transform of the wavelet along with a numerically computed Fourier transform of the signal through (Addison, 2002)

$$T(a,b) = \int_{-\infty}^{\infty} \hat{x}(f)\, \hat{\psi}^*_{a,b}(f)\, df, \tag{4.9}$$

where $\hat{\psi}^*_{a,b}$ is the complex conjugate of the Fourier transform of the dilated and translated mother wavelet.

The interpretation of the CWT relies heavily on understanding the local changes in the magnitude of the transform over the duration/extent of the signal. Large values of the CWT signifies resonance at the corresponding scales. Additionally, if the wavelet function is complex, the CWT will have the additional advantage of revealing local phase information at all possible locations and scales. Accordingly, using Morlet, as an example for a complex wavelet, it is easy to identify not only the local scale changes but also local transitions and discontinuities in the signal's phase. The modulus and phase of the CWT are, respectively,

$$|T(a,b)| = \sqrt{[Re(T(a,b))]^2 + [Im(T(a,b))]^2}, \tag{4.10}$$

$$\phi(a,b) = \tan^{-1}\{[Im(T(a,b))]/[Re(T(a,b))]\}, \tag{4.11}$$

where $[Re(T(a,b))]$ and $[Im(T(a,b))]$ are the real and imaginary part of the wavelet transform respectively.

While understanding the behavior of the phase of the CWT for real signals often proves to be an involved task it can (especially true for higher dimensional signals) sometimes reveal very important patterns at a sub-class of scales even in the presence of significant noise levels (such as the phase dislocation sites in the vorticity structures described in Dallard & Browand (1993)). For the sake of simplicity, all interpretations of CWTs used in this thesis are based on checking the magnitude of the transform for local resonance. As 2D/plane data is often readily available from experiments and numerical simulations, it is natural to consider extending the utility of the current CWT framework to two dimensions and hence this is the subject of the next section.

4.3 2-D continuous wavelet transforms

Separation of the amplitude and the phase of a signal $x(t)$ containing multiple frequencies can be achieved by defining a complex function

$$X(t) = x(t) - iH(x(t)), \tag{4.12}$$

where $x(t) = Re[X(t)]$ and $H(x(t))$ is the Hilbert transform of $x(t)$;

$$H(x(t)) = \int_{-\infty}^{\infty} \frac{x(\tau)}{\pi(t-\tau)} d\tau. \tag{4.13}$$

The instantaneous envelope amplitude and phase of the signal are, respectively,

$$A = \sqrt{x^2 + H(x)^2}, \tag{4.14}$$

$$\phi = \tan^{-1}\left(-H(x)/x\right), \tag{4.15}$$

It can then be shown that (Dallard & Spedding, 1993)

$$f < 0 \Rightarrow \hat{X}(f) = 0. \tag{4.16}$$

Functions satisfying (4.16) are called "Hardy" functions or are said to occupy Hardy space $\mathcal{H}$. Any wavelet function $\psi \in \mathcal{H}$ has a wavelet transform $T(a_0, b)$ (a_0 being a fixed scale) that exists in $\mathcal{H}$ and hence has an instantaneous phase and amplitude.

Dallard & Spedding (1993) extended the concept of Hardy function to two dimensions by defining wavelet functions in Fourier space, paritioning the 2D wave number plane into two partitions π^1 and π^2 and setting the Fourier transform of the function to zero on one of the half planes. Two types of wavelets were thus defined. In one type, the wavelet is directional-specific which means it selects wave vectors with a preferred wave number magnitude (i.e. scale)

and orientation. In the other type, the wavelet function is referred to as "cylindrical" which means it has no directional selectivity and hence it resonates with wave vectors having a preferred wave number magnitude regardless of their orientation.

They further defined a directional-specific wavepacket-like wavelet referred to as *Morlet2D* through

$$\psi_\alpha(\vec{r}) = \exp\left(i\,\vec{\kappa_o}.\vec{r}\right)\,\exp\left(-|\vec{r}|^2/2\right), \tag{4.17}$$

where $\vec{r}$ is an arbitrary position vector in a 2D Cartesian plane, and $\vec{\kappa_o}$ is a fixed characteristic wave number vector oriented at angle α to the horizontal x axis. The Fourier transform of *Morlet2D* is then

$$\hat{\psi}_\alpha(\vec{\kappa}) = \exp\left(-\frac{\left|\vec{\kappa}-\vec{\kappa_0}\right|^2}{2}\right). \tag{4.18}$$

Notice that *Morlet2D* is not strictly a Hardy function and that its zero frequency component is not identically zero, however these conditions are *almost* satisfied for large enough $\left|\vec{\kappa_o}\right|$ (such as $\left|\vec{\kappa_o}\right| = 5.5$ in Morlet & Grossman (1984)). Figure (4.3) shows a *Morelt2D* wavelet oriented at $\alpha = 45^\circ$ to the horizontal axis both in the spectral (a) and physical space ((b),(c)). If the analyzed 2D signal has a clearly perceived predominant directionality that is known a priori, Dallard & Spedding (1993) found that *Morlet2D* has sharper selectivity than non-directionally based wavelets. However, if the signal contains many contributions at different scales and orientations, a non-directionl wavelet would be most valuable, otherwise an exhaustive search of resonance (i.e. local maximization of the modulus of the transform) must be conducted at multiple values of α to cover the entire wave number plane.

For this reason, Dallard & Spedding (1993) sought a wavelet with additional

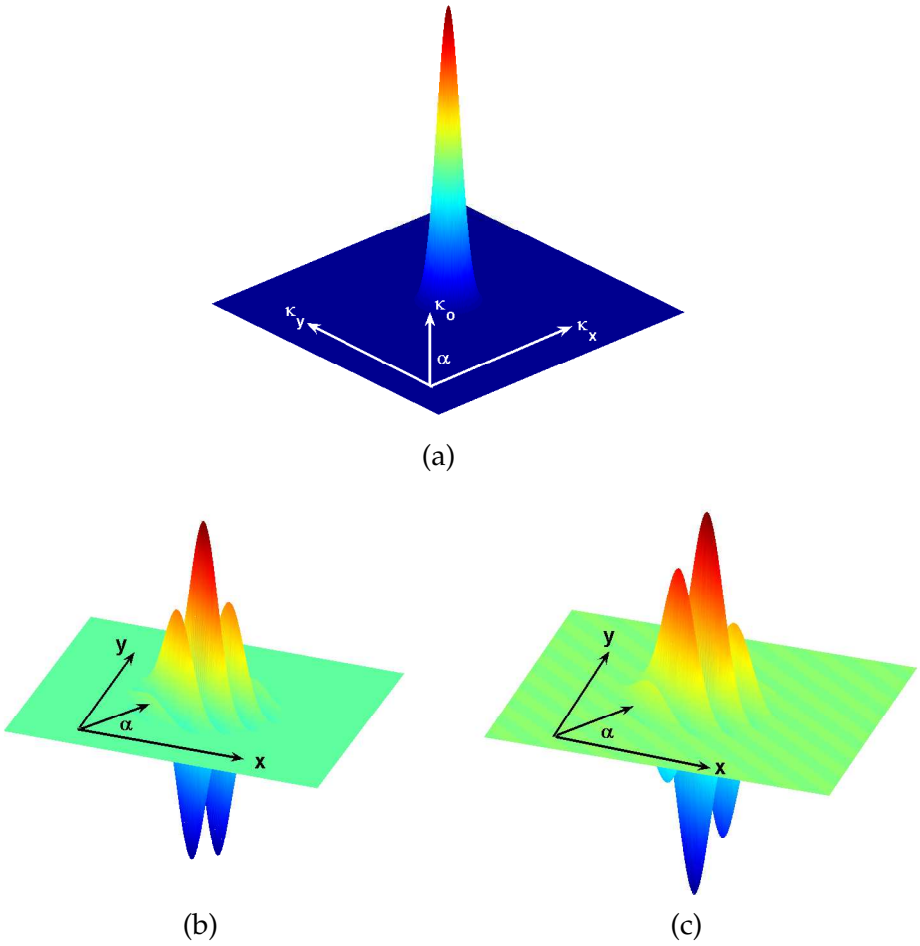

Figure 4.3: *Morlet2D* wavelet at $\alpha = 45°$(a) Fourier transform (b) Real part in physical space (c) Imaginary part in physical space

symmetry that is sensitive only to wave numbers at a specific scale regardless of their orientation. They defined a symmetric real wavelet that they referred to as *Halo* such that its structure in the wave number plane is symmetric in the radial direction in which resonance occurs over an annular-like region that is displaced from the origin by a radius κ_0/a. In order to make it a Hardy function (and thus separate the amplitude and phase information) they further restricted the contributions in the wave number space to one half-plane leading to the complex Arc wavelet (see Fig.(4.4)). Mathematically, the Arc is defined

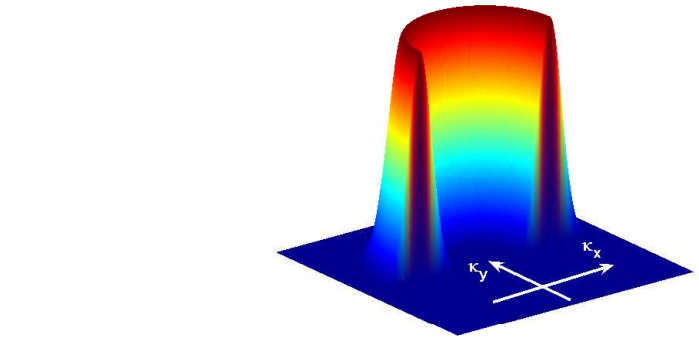

(a)

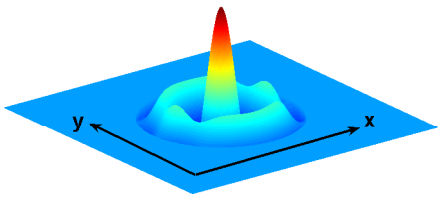

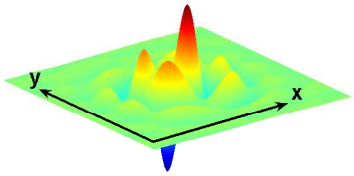

(b) (c)

Figure 4.4: Arc wavelet: (a) Fourier transform (b) Real part in physical space (b) Imaginary part in physical space

as

$$\hat{\psi}(\vec{\kappa}) = \exp\left(-\frac{\left(|\vec{\kappa}| - |\vec{\kappa_0}|\right)^2}{2}\right) \qquad \vec{\kappa} \in \pi^1;$$
$$\hat{\psi}(\vec{\kappa}) = 0 \qquad \vec{\kappa} \in \pi^2 \tag{4.19}$$

We have used a proprietary Fortran 77 code developed by Dallard & Spedding (1993) in which both the 1D and 2D CWT are implemented using Fourier transform as explained in §4.2. A series of test cases were run in order to make sure an independent Fortran-90 module that we developed based on the Fortran-77

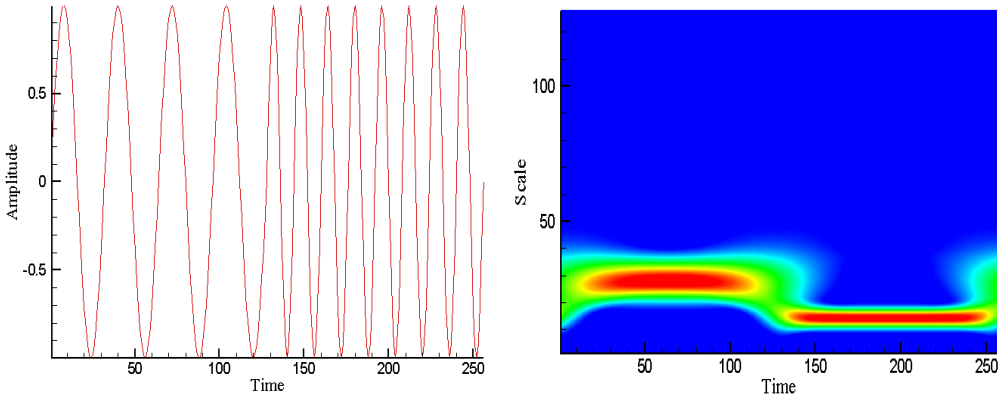

(a) (b)

Figure 4.5: Frequency doubling: (a) time domain (b) 2D contours of the CWT modulus in the wavelet space (contour levels are arbitrary)

code faithfully reproduces the evolution (distribution) of spectral content over the duration (spatial extent) of some of the well-known standard analytical test signals.

As an example for the application of the one dimensional CWT, Fig. 4.5(a) shows a 1D temporal signal in which the frequency of the oscillation doubles halfway into the signal ($t = 128$). A complex 1D Morlet wavelet function was chosen for the analysis with a number of scales $n_a = n/2 = 128$ where n is the signal size. Note that the characteristic period T_p of the wavelet at a given scale a is related to the mother wavelet primary frequency f_0 through $T_p = a \times dt/f_0$, where a is a linear index ($a = 1, 2, ..., n_a$) and dt is the time resolution of the signal. The absolute value/modulus of the CWT in what is referred to as "the wavelet space/domain" (i.e. the time-scale plane (Addison, 2002)), is plotted in Fig. 4.5(b) using red and blue (for maximum and minimum resonance,

respectively) color-coding scheme. The periodicity of the signal in the time domain is reflected as continuous bands in the wavelet space with maximum resonance occurring at the center of the bands at the expected scales. The center of the upper band corresponding to the larger periodicity occurs at a larger (double) scale than the center of the lower band and the breadth of the band (sometimes called " the band of influence"), on a linear scale, seems to be proportional to the associated resonance scale.

Finally, the visible warping of the continuous bands near the edges of the signal is a direct result of the errors introduced by the overlapping of the wavelet "support" (the characteristic width of the wavelet) with the left and right edges of a finite extent signal. The length (area in 2D signals) of the signal affected by the edge or boundary effect scales with the dilated wavelet scale (as increasingly larger portion of the dilated wavelet falls outside of the signal near its end points) and, accordingly, the accuracy of the transform is compromised at the larger scales. Usually scales beyond $n/4$ are heavily contaminated by edge effects and, as a result, should not be considered. For more test cases that further reinforce the basic principles and demonstrate the utility of the CWT the reader is referred to appendix A. The next sections provides a brief review of the fluid mechanical applications of the wavelet transform.

4.4 Applications in fluid mechanics

The early comprehensive reviews by Farge (1992) and Meneveau (1991) provided a clear and rigorous explanation of the mathematical basis of the wavelet transform, its numerical implementation and its application to the analysis and

computations of turbulent flows. For example, Farge (1992) suggested new diagnostics for turbulent flows based on wavelet analysis such as local scale-based wavelet energy spectrum, local intermittency measures, space-scale contrast, space scale isotropy measures and a local scaling and singularity spectrum.

More recently Addison (2002) provided a thorough review of the applications of wavelet transform in the general area of fluid mechanics. Some of the notable examples mentioned therein are:

- Identification and characterization of the properties of coherent eddy structures like those forming at the interface of two fluid layers moving at different velocities (Bonnet & Glauser, 1994).
- Investigating the eddy structure in free turbulent jets by Li & Nozaki (1995) and their subsequent use of a wavelet cross-correlation function to relate two simultaneous measurements at different locations.
- Identifying the frequency of vortex shedding downstream of an elliptical plate by Kiya & Abe (1999).
- Fluid-structure interaction problems such as the transient response of buildings to wind storms, and bridge response to vortex shedding (Gurley & Kareem, 1999).

Finally as the 2D wavelet transform framework developed by Dallard & Spedding (1993) is the basic tool used in this thesis for analyzing the wake generated IGWs, it becomes important to review the applications in which Spedding and collaborators subsequently used it. Long, Lai, Huang & Spedding (1993) used a one dimensional complex Morlet wavelet to analyze the measured sur-

face wave field in their experiments on the blocking and trapping of waves by inhomogenous flow fields. They found that strong current gradient near the blocking point (the area where the velocity of the local current is larger in magnitude than that of the wave group but is opposite in direction to it) traps wave energy and shifts the wave numbers into a regime that matches the microwave wavelength of many remote sensing devices; a phenomenon that provides the link between surface wave structure and strong current gradient zones.

Spedding, Browand, Huang & Long (1993) used the 2D complex wavelet transform developed in (Dallard & Spedding, 1993) to investigate the unsteady wind-generated surface wave field. They found that these waves have widespread phase dislocations that persist until the initial wave field becomes disordered in appearance. They also found that the energy in the fundamental wavelength generated by the instability of the initially quiescent water surface saturates over time, whereas the energy in the subharmonic components continue to increase over time. Energy in wave vectors aligned at a small angle off the mean wind direction was also found to increase until it becomes a substantial fraction of the total energy. They also discussed the possible role of phase defects in the nonlinear energy transfer and its analogy to plane mixing layers. Dallard & Browand (1993) used the same 2D wavelet transforms to study what they called a defect/dislocation site (a Y-shaped branching pattern) in the vorticity structures of plane mixing layers. Interestingly, they found that a dislocation site acts as a nucleus that initiates a rapid and localized evolution to larger scales.

In the next chapter, we extend the applications of the 2D wavelet transform framework developed by Dallard & Spedding (1993) to the determination of

the spectral characteristics of the internal gravity waves generated by the turbulent wake of a towed sphere in a uniformly stratified fluid. The ability of wavelets to detect spatially localized coherent waves at different scales and orientations and to relate these scales to their spatial locations has proven to be most useful in understanding and characterizing the wake generated wave field. The localization in time is also another important aspect of this problem, especially for the low Reynolds number simulations, where the wave emission by the turbulent wake is more transitory in nature than the corresponding high Reynolds number simulations.

CHAPTER 5

INTERNAL WAVE EMISSION BY A STRATIFIED TURBULENT WAKE

5.1 Problem setup

The base flow considered in this study is a stratified turbulent wake with nonzero net momentum. Such a flow corresponds to the wake of a sphere of diameter D towed with a velocity U in a uniformly stratified fluid with buoyancy frequency N. Incorporation of the wake-generating sphere in the computational domain is a highly challenging computational task, as a spherical grid positioned around the sphere would need to be coupled to a Cartesian grid further downstream. Apart from being confronted with issues of sphere boundary layer resolution at the Reynolds numbers of interest, such a spatially developing treatment of the wake would require a prohibitively large computational degrees of freedom to capture the intermediate NEQ and far Q2D regimes of wake evolution, two stages of prime interest for the study of IGWs generated by the turbulent wake. Thus, as in Orszag & Pao (1974) and in the more recent studies of stratified turbulent wakes (Gourlay, Arendt, Fritts & Werne, 2001; Dommermuth, Rottman, Innis & Novikov, 2002; Diamessis, Domaradzki & Hesthaven, 2005) the computational domain and spatial discretization do not account for the sphere and focus only on the flow generated in its wake. Specifically, the computational domain is a three-dimensional volume inside the wake region, centered on the wake centerline. Within this volume of dimensions $L_x \times L_y \times L_z$ shown in Fig. 5.1 the three-dimensional and time dependent wake flow field is computed. Effectively in this methodology, the computational domain may be regarded as an isolated three-dimensional block, centered around a fixed downstream location, in the wake region of a sphere that is

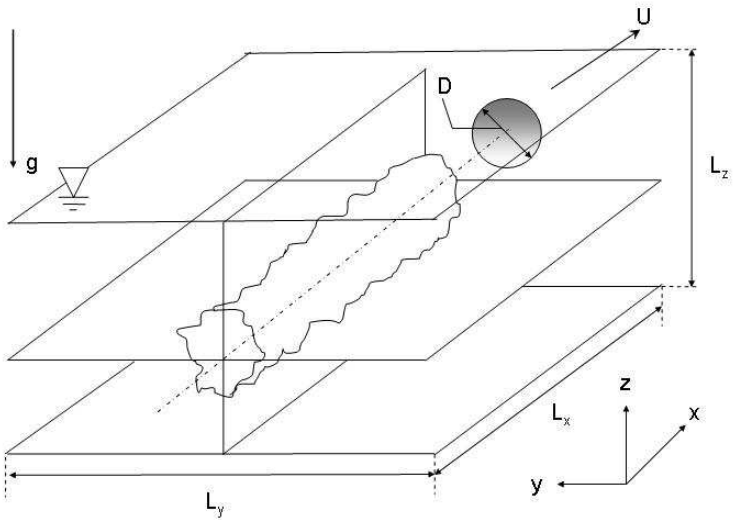

Figure 5.1: Computational domain for the simulation of a stratified turbulent wake with non-zero net momentum.

shot through a stratified water tank. The numerical simulation thus represents the time evolution of the turbulent field contained within the three-dimensional block. The coordinate axes are positioned such that $(x, y = 0, z = 0)$ corresponds to the wake centerline and $x = -L_x/2$ is at the left end of the domain. After evolution time t the solution is interpreted as a representation for a three dimensional block of the wake flow at a distance $X/D = U_o t/D = Nt.Fr/2$ downstream from the location of the initial block (denoted X_0/D). The numerical model is thus statistically homogeneous along the wake axis (the x direction) but non-stationary in time. The domain is assumed to be horizontally periodic in both directions. The periodicity in the downstream x direction is appropriate as the length of the computational domain is much smaller than the total wake length (Dommermuth, Rottman, Innis & Novikov, 2002) which ensures

that the streamwise variation of all average quantities is negligible compared to their variation in the other directions. The periodicity assumption in the spanwise direction is justifiable provided the horizontal length scale of the wake L_H does not exceed a threshold value (taken as $0.15L_y$, where L_y is the spanwise dimension of the computational domain) , beyond which spurious interactions with the spanwise-periodic image are possible (Diamessis, Spedding & Domaradzki, 2010*b*). On account of the spanwise periodicity, internal waves radiated by the wake will re-enter the computational domain unless the domain lateral boundaries are equipped with wave absorbing layers as explained in section (5.4). The vertical boundary conditions are a no-slip bottom wall and a free-slip (stess-free) top surface. The wake flow in the initial block is assumed to be fully three dimensional self-similar near wake flow and for that to be ensured, a complex initialization procedure , the details of which are summarized in the next section, is implemented.

5.2 Initialization

As discussed in section (5.1), the sphere is not accounted for in the computation and the initial condition of the simulation corresponds to an approximation of the near-wake at $x/D = 2$ from the sphere. Specifically, the initial mean and fluctuating velocity profiles are constructed to represent a self-similar axisymmetric nonstratified wake (Tennekes & Lumley, 1972; Meunier, Diamessis & Spedding, 2006). The erroneous assumption of self-similarity this close to the towed body is not critical for the purpose of these simulations, which focus on the intermediate-to-late time wake. Moreover, the specific choice of initial condition, described in detail elsewhere (Diamessis, Spedding & Domaradzki,

2010*b*), is found to reproduce a physically accurate transition into the NEQ regime, during and after which the numerical simulations exhibit power laws for the mean flow scaling and a vorticity field structure that agree very well with their experimental counterparts. It should nevertheless be noted that the generation of the initial wake velocity and density fields is a complex process consisting of two preliminary simulations before the main simulation can be started.

The preliminary runs involve a relaxation stage where the mean and turbulent velocity fields become adequately correlated and a transition stage where the mean flow exhibits the prescribed self-similar behavior and the ambient density profile is gradually introduced (ramped up) to minimize any spurious buoyancy-driven transients (Diamessis, Spedding & Domaradzki, 2010*b*). Upon termination of the relaxation procedure, the downstream distance from the sphere is assumed to be equal to $x/D = 2$. The transition run has a duration of $tU/D = 6$, which sets the equivalent of downstream distance from the sphere at the beginning of the primary simulation to be equal to $X_0/D = 8$.

5.3 Summary of numerical simulations

This study considers results from five different numerical simulations of stratified turbulent wakes with non-zero net momentum at Reynolds number, $Re = UD/\nu = 5 \times 10^3$ and 10^5 and internal Froude number, $Fr = 2U/(DN) = 4, 16$ and 64 for $Re = 5 \times 10^3$ and $Fr = 4, 16$ for $Re = 10^5$. Hereafter, each run will be labeled as *RxFy*, where $x = Re/10^3$ and $y = Fr$. For all simulations, the values of U and D are the same. The Reynolds number and Froude number are

varied by changing the values of ν and N, respectively. At a fixed Re value, all Fr simulations, where the computational domain dimensions are the same (see below), use the same relaxation run. The final result of this run is used to initialize the particular transition run for the desired Fr where the mean density gradient is ramped-up to its designated value.

As the purpose of the study is to characterize the internal wave radiation from the turbulent wake, the total "useful" simulation time is where the wake adjusts to the increasing effects of the buoyancy forces (i.e. the full extent of the NEQ regime) all the way to the initial stages of the Q2D where the pancake vortices have fully emerged and dominated the wake core. As the specific transition point leading into the Q2D is both Re and Fr dependent, being $20 < Nt < 30$ at $Re = 5 \times 10^3$ and $60 < Nt < 120$ at $Re = 10^5$ (see Diamessis, Spedding & Domaradzki, 2010*b*), it is reasonable to expect that the period $2 \lesssim Nt \lesssim 100$ captures all the dynamics of the energetically significant wave radiation at all Re and Fr relevant to this study.

As there is no need to run beyond $Nt \simeq 100$, we do not use the spanwise regridding procedure that was periodically applied by Diamessis *et al.* (2010*b*) provided $L_H \leq 0.15L_y$ is enforced during the continuous lateral expansion of the wake, if such a computational domain width can accommodate the expected wake growth during $2 < Nt < 100$. Now, wake confinement issues aside, by considering the imposed spanwise periodicity, the IGWs will re-enter the computational domain and interfere with newly emitted waves. Hence, after some time, the internal wave field will not correspond to its experimental counterpart. For this reason, the vertical and lateral domain boundaries need to be equipped with artificial wave absorbing layers (detailed in the next sec-

tion) to efficiently remove the internal waves from the computational domain before they impact the boundaries and either re-enter the domain through the lateral boundaries or reflect back towards the wake core from the top and bottom boundaries and contaminate the IGW field emitted by the wake.

Finally, from a computational data analysis stand point, the domain dimensions should allow a reasonable "free" propagation space for the radiated IGW to move away from the turbulent core in order to unambiguously determine their spectral characteristics and avoid undesirable contamination by the wake turbulence. The domain dimensions (mainly dictated by Fr) are $L_x \times L_y \times L_z = 26\frac{2}{3}D \times 26\frac{2}{3}D \times 12D$ for $Fr = 4, 16$. On account of the increased wake width with Fr at a given Nt, the spanwise dimension of the $Fr = 64$ case is chosen to be $40D$. Although a domain height $L_z = 12D$ accommodates the vertical extent of the wake for all Fr simulations throughout $1 < Nt < 100$, the free space available for wave propagation decreases with increasing Fr. Thus, for $Fr = 64$, the domain height is increased to $L_z = 20D$.

The spectral multidomain grid with the streamwise direction employing a uniform grid is shown in (see Fig. 3.1(a) and (b)) for the R5Fr4 case. The computational domain has $M = 7$ vertical subdomains with constant order of polynomial approximation $\hat{N} = 24$ inside each subdomain. The vertical resolution is optimally clustered around the wake core to accurately resolve the turbulent field and adequately capture the large scale internal wave-dominated "ambient". For $Fr = 64$ simulation the number of vertical subdomains is increased to $M = 9$ while the polynomial order of approximation inside the subdomains is kept the same. Grid independence tests for $Re = 5 \times 10^3$ are reported in Diamessis *et al.* (2010*b*) where the authors compare results from simulations with

coarser grids relative to the currently used grids and show that identical mean and fluctuating velocity profiles and streamwise spectra are obtained over the entire wake evolution. At the higher Reynolds number, and on account of the prohibitive cost of grid independence tests, the authors ensured that the thickness of the vertical shear layers that develop in the intermediate to late wake for the $Fr = 4$ case is well resolved by increasing the polynomial order to $\hat{N} = 40$ (p-refinement) and the number of subdomains $M = 13$ (h-refinement) (see Fig. 3.1(a), and (b) for details). By appealing to Fr-scaling arguments, the authors conclude that the thickness of the shear layers is larger for the $Fr = 16$ case, and hence they are well resolved, for the $Fr = 16$ case, if they are adequately resolved for the $Fr = 4$ case.

All simulations performed employ the MPI-based parallel implementation of the flow solver described in chapter 3. $Re = 5 \times 10^3$ runs use $\hat{N}_P = 32$ processors for $Fr = 4, 16$ and $\hat{N}_P = 64$ for $Fr = 64$, whereas the $Re = 10^5$ simulations require $\hat{N}_P = 256$. All simulations and postprocessing were performed at the Arctic Region Supercomputing Center's Midnight Linux cluster. Midnight has 2 Sun Fire X4600 login nodes and two types of compute nodes: (a) 256 Sun Fire X2200 nodes (2 dual core processors per node) (b) 35 Sun Fire X4600 nodes (8 dual core processors per node) with Voltaire Infiniband Interconnect. On this machine, the average wall-clock time required for a computational timestep is 7 sec and 21 sec for the low and high Re runs, respectively. The respective durations of the "relaxation" runs in wall-clock time were 16 hours and 10 days. The primary simulations at $Re = 5 \times 10^3$ required between 16 and 24 hours of wall-clock time. The wall-clock timing for a high Re simulation was approximately 26 days.

The three dimensional horizontal divergence field (an indicator of the wave field activity) and the three vorticity components were output every $0.1Nt$ for postprocessing purposes. The data base thus built comprised 1000 snapshots for each run which amount to almost 200 GB of disk space per Fr at the low Re and 2 TB per Fr at the high Re. The data was transferred to local storage drives using Cornell's connection to the National LambdaRail; a high-speed national network infrastructure with very high capacity and high bandwidth, using a multi-stream scripted file transfer command (MPSCP) which allowed us to transfer data at a rate $\simeq 2/3$ GB/minute.

Independent serial Fortran 90 subroutines were developed that allowed us to read in the binary data files dumped out by the individual processors and extract (a) two dimensional slices of data on xy, xz, yz planes at any any location/time (b) space-time diagrams $x-t, y-t, z-t$ at prespecified locations (c) time series at any arbitrary point within the three dimensional data volume. Two dimensional slice data on select xy planes were imported into the two dimensional CWT Fortran module to determine the horizontal wave lengths of the IGW field. Similarly, $x-t$ diagrams at select locations were also imported into the one dimensional CWT Fortran module to calculate the frequency of the IGWs from which the phase line inclination angles were determined using the dispersion relation. Finally, the three dimensional velocity and density fields were output every $2Nt$. The simultaneous availability of the velocity and density fields allows the calculation of the instantaneous pressure (a quantity that is not directly solved for in the main solver), the momentum, the energy and the buoyancy flux associated with the wave field, which will be the subject of future studies.

5.4 Wave sponge layers

Wave propagation problems in infinite domain require the imposition of a radiation boundary condition which requires the amplitude of waves entering the domain from infinity to be zero (Durran, 1999). On a finite computational domain, the mathematical formulation of an appropriate radiation boundary condition is very difficult to derive and is only known for simple one dimensional and spherically symmetric wave problems (Israeli & Orszag, 1981). Wave absorbing layers placed at the edges of a finite sized computational domain represent an approximate and simple way to prevent outward propagating waves from reflecting back into the computational domain. Wave absorbing layers are particularly useful in applications for which the exact radiation boundary condition are not known (Durran, 1999).

Two types of wave damping layers are typically used (Durran, 1999). For the sake of this discussion, we assume the η direction to be normal to the lateral boundaries where the sponge layers are placed . The viscous type damper involves the incorporation of a viscous term with a varying viscous coefficient; that is $\nu(\eta)\nabla^2 u$ to the right hand side of the disturbance (u) evolution equations (the momentum and density equations in our study). The viscous coefficient is zero inside the computational domain and increases smoothly with distance inside the layer. The other type is referred to as a "Rayleigh-damping" absorbing/sponge layer which takes the form $-R(\eta)u$ and is also added to the right hand side of the disturbance equation. The ratio $1/R(\eta)$ sets a characteristic time scale for the absorbing layer which is the time over which the layer acts to effectively damp out the disturbance inside it. In both layer types, although it is desirable to have a large coefficient ($\nu(\eta)$ or $R(\eta)$) to dissipate the waves before

they reach the boundaries and reflect back into the domain, rapid changes in the medium properties caused by the choice of large coefficients in combination with relatively thin layers lead to reflection of the waves off the absorbing layers back into the domain. For the linearized shallow water system, Israeli & Orszag (1981) found that the undesirable backward reflection of the waves is less scale dependent for a Rayleigh damper than a viscous damper. Hence the Rayleigh damper offers a better performance.

In our wake simulations, we use a Rayleigh type damper with a smooth profile (see Fig. 5.2), similar in form to that used by Klemp & Lilly (1978) namely:

$$R(\eta) = \alpha sin^2\left(\frac{\pi}{2}\frac{(\eta - \eta_i)}{\delta_t}\right), \tag{5.1}$$

where $\alpha = 1/T_{sp}$ and T_{sp} is the sponge layer time scale, [η is the boundary-normal coordinate direction and η_i is the coordinate of the interface between the sponge layer and the interior of the computational domain], and δ_t is the thickness of the layer (see Fig. 5.2 and 5.3). The absorbing layers wrap around the yz plane as shown in Fig. 5.3 and thus R is a function of both y and z. To avoid erroneous reflection of the wave field we choose the thickness of the layer to be comparable to the wavelength of the most energetic waves. As this scale is not known beforehand we assume a layer thickness and test its efficiency upon completion of a simulation at a given Re, Fr. We have found that a $2D$ thickness, where D is the sphere diameter, is sufficient for $Fr = 4,\ 16$ simulations at both Re, while a thickness of $4D$ was necessary for the $Fr = 64$ simulation.

We test the efficiency of the sponge layers by following the same approach in Taylor & Sarkar (2007) wherein sample depth-time diagrams at multiple down stream locations are Fourier-transformed into the vertical wave number-frequency domain. Then the ratio of the energy of the downward to the upward

moving wave field is estimated. Since this ratio is below 4% in all simulations reported here, the absorbing layers are deemed to perform reasonably well.

Finally, a word of caution is in order in terms of the choice of the absorbing layer time scale. Although it is obviously advantageous to choose a small time scale for the absorbing layer, this time scale can not be smaller than the maximum time step that is permissible by the discretization scheme (Δt_{max}). Otherwise, numerical instabilities develop. Hence, we impose an additional time step constraint;

$$\Delta t_{max} \; < \; min\left(\frac{1}{R(\eta)}\right), \tag{5.2}$$

where $R(\eta)$ usually attains its peak value at the computational domain boundary. Specifically, the time scale $T_{sp} = min\,(1/R(\eta))$ is taken to be equal to $2\Delta t_{max}$ where $\Delta t_{max} = (2\pi/N)/60$.

5.5 Results

5.5.1 Visualization of the wave field structure

The analysis of the wave field properties in this study relies on the horizontal divergence field, defined as

$$\mathbf{\Delta}_z = \nabla \,.\, \mathbf{u}_H, \tag{5.3}$$

where the horizontal velocity vector $u_H \equiv (u, v)$, serves as an indicator of the amplitude of the internal wave motion on horizontal xy planes above the turbulent wake region, as done in the experiments of Spedding, Browand, Bell & Chen (2000). From the continuity equation for an incompressible Boussinesq

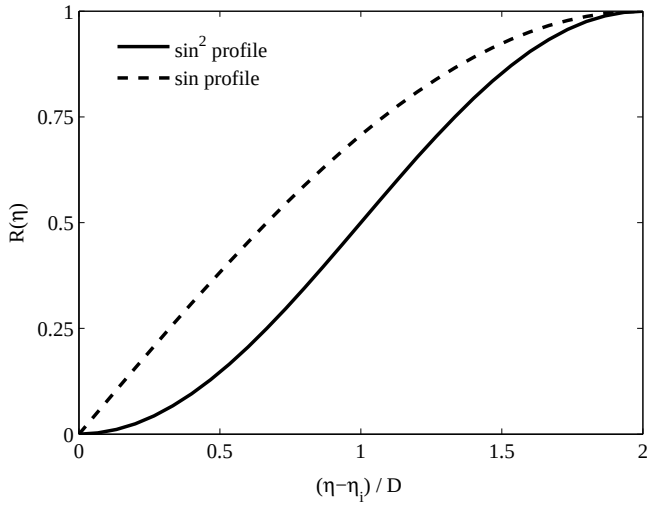

Figure 5.2: Rayleigh damping layer profile in the wall normal direction η

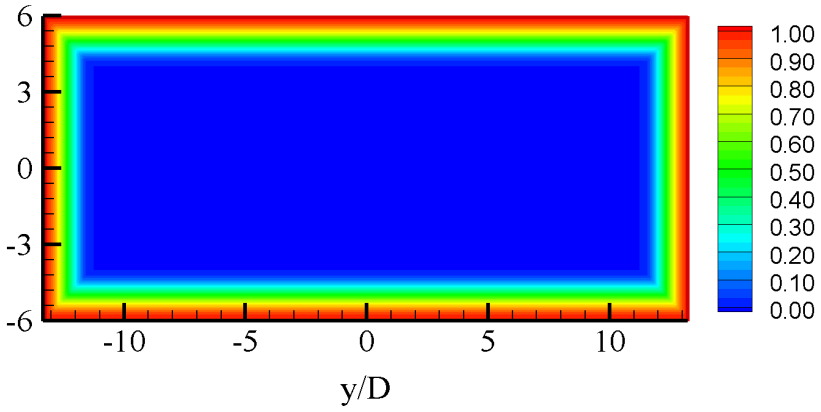

Figure 5.3: Two dimensional contours of the Rayleigh damping layer coefficient $R(y,\ z)$

fluid, it is obvious that

$$\mathbf{\Delta}_z = \frac{\partial u}{\partial x} + \frac{\partial v}{\partial y} = -\frac{\partial w}{\partial z}, \tag{5.4}$$

and hence equation 5.4 provides a direct relationship between the amplitude of the horizontal divergence field and that of the vertical derivative of the vertical velocity component of an internal wave field. Both quantities can be related to the isopycnals/vertical displacement field A_ζ through linear theory. Specifically, for a monochromatic small amplitude internal wave field in a uniformly stratified fluid, following the approach outlined in (Sutherland, 2005), it can be shown that:

$$\begin{aligned} A_{\mathbf{\Delta}_z} &= m\, A_w \ , \\ A_w &= \omega\, A_\zeta \ , \\ A_\zeta &= \frac{A_{\mathbf{\Delta}_z}}{m\, \omega} \ , \end{aligned} \tag{5.5}$$

where (absolute values are implied in equation (5.5) A_w is the amplitude of the vertical velocity field, m is the vertical wave number, $A_{\mathbf{\Delta}_z}$ is the amplitude of the horizontal divergence field, ω is the wave frequency, and A_ζ is the isopycnals displacement amplitude. As a consequence of equation 5.5, the isopycnals displacement amplitude is proportional to $\mathbf{\Delta}_z/N$ (as $\omega = Ncos(\theta)$) and hence normalizing the horizontal divergence field by the buoyancy frequency provides an approximate measure of the vertical displacement of the wave field.

Figure 5.4 shows the evolution of the normalized horizontal divergence field on horizontal xy planes above the wake center line for the low Re cases. The choice of the vertical location of the horizontal plane of analysis should be such that any possible contamination by the turbulent core during the wave evolution should be avoided. The normalized wake half height L_v/D [defined as in Diamessis *et al.* (2010*b*), through least-squares fitting a Gaussian profile to the streamwise averaged velocity] for $R5F4$ up to $Nt = 100$ (not shown); does not

exceed 0.5, a horizontal plane located at $z/D = 1.5$ is reasonably well-removed, but not too far, from the turbulent core (to minimize viscous damping of the waves). As the wake height increases with Fr, the plane locations for the other Fr cases were chosen through a $\sim Fr^{0.29}$ scaling (15% bigger than the $Fr^{0.25}$ wake height growth scaling determined by Diamessis *et al.* (2010*b*)), again, as a safety factor, to prevent any possible wake intrusion into the analysis planes. Note also that the region containing the wave field extends out to about $4D$ in the spanwise direction for $R5F4$. The limits of this region increase approximately as $Fr^{1/3}$ commensurate with the increase in the wake's horizontal extent determined by Diamessis *et al.* (2010*b*).

Note that the limits of the contour levels reported in Fig. 5.4 are chosen to optimize the visualization of the wave field at the earliest reported time. If the instantaneous maximum wave amplitude is chosen, the spatial structure of the wave packets becomes almost invisible and thus, the contour levels are chosen as approximately 50% of the maximum amplitude at the earliest shown time $Nt = 15$, where the wave emission is relatively weak. It is clear that the amplitude of the normalized horizontal divergence field increases with Fr (i.e. with reduced stratification) indicating, by virtue of equation 5.5, that the vertical displacement amplitude also increases, in general agreement with the experimental observations of Dohan & Sutherland (2003).

The wave field in Fig. 5.4 has a striking similarity to the wave field measured by Spedding *et al.* (2000) for $Fr > 4$, where the wave field is dominated by the random wake-generated waves and not the body generated lee waves. It is clear that the wake emits coherent wave packets starting early on and that the process continues throughout the NEQ regime. One of the basic differences

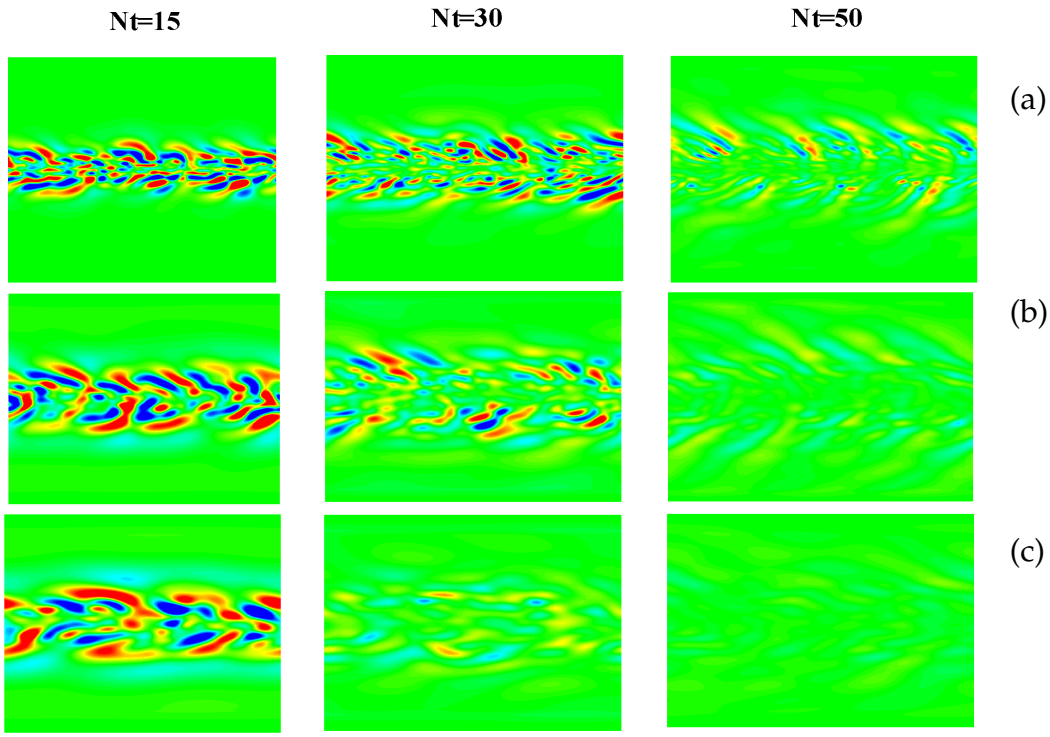

Figure 5.4: Two dimensional contour plot of Δ_z/N at different times on horizontal *xy* planes at z/D=1.5, 2.3, 3.4 for (a) R5F4, (b) R5F16, (c) R5F64. The sphere travels from left to right. The min./max. ranges for the colorbars of Δ_z/N are (a) [-0.025,0.025], (b)[-0.04,0.04] , and (c) [-0.05,0.05].

between the evolution for the different Fr cases is that the peak wave activity (as evidenced by the abundance of strong and coherent wave packets on the horizontal plane of the analysis) seems to happen earlier in Nt units as does the cessation of wave emission, as Fr increases. This is not a result of a faster wave propagation time scale (in fact we will show later that the vertical group velocity of the internal waves decreases as Fr increases) but rather seems to be a result of the comparison being held at the same Nt rather than the same down-stream distance (note that the equivalent down-stream distance for a given time Nt is proportional to Fr). In effect, what this means is that even if internal wave radiation by the wake may start at the same down-stream distance regardless

of Fr, it will appear to happen later in Nt units as Fr increases. For the same reason, the turbulence inside the wake viscously decays faster over the same period in Nt units and hence wave radiation ceases earlier (in Nt units) as Fr increases.

Regarding the scale and structure of the wave field, it can be seen that the wave packets are strongly localized in the horizontal, with the individual wave packets' spatial envelopes containing $\approx 1 - 2\lambda_H$), where λ_H is the horizontal wavelength. Also the localization tends to increase with Fr and the horizontal wavelength appears to increase with Fr. For a given simulation, the horizontal wavelength tends to decrease over time and the wave field tends to lose its coherence over time. A more quantitative analysis of the length scales will follow in the next section.

One of the intriguing features of the $R5F64$ case, also observed in the experiments of Spedding *et al.* (2000) for $Fr > 40$, is the presence of almost horizontal coherent bands at the left and right edges of the wave dominated region. This was described to by Spedding *et al.* (2000) as "a wave front marking the maximum horizontal propagation rate of disturbance due to initially turbulent eddy motions (analogous to a Mach cone in compressible flow)". By reducing the limits of the contour levels for the $Fr = 16, 64$ (not shown), it was clear that the bands also exist at the $Fr = 16$ case but they are significantly weaker in magnitude and less streamwise coherent, which perhaps made them only measurable in the Spedding *et al.* (2000) experiments when $Fr > 40$.

At the high *Re* (Fig. 5.5 and 5.6), the most evident feature is the persistence of the wave emission linked to the prolongation of the NEQ regime observed

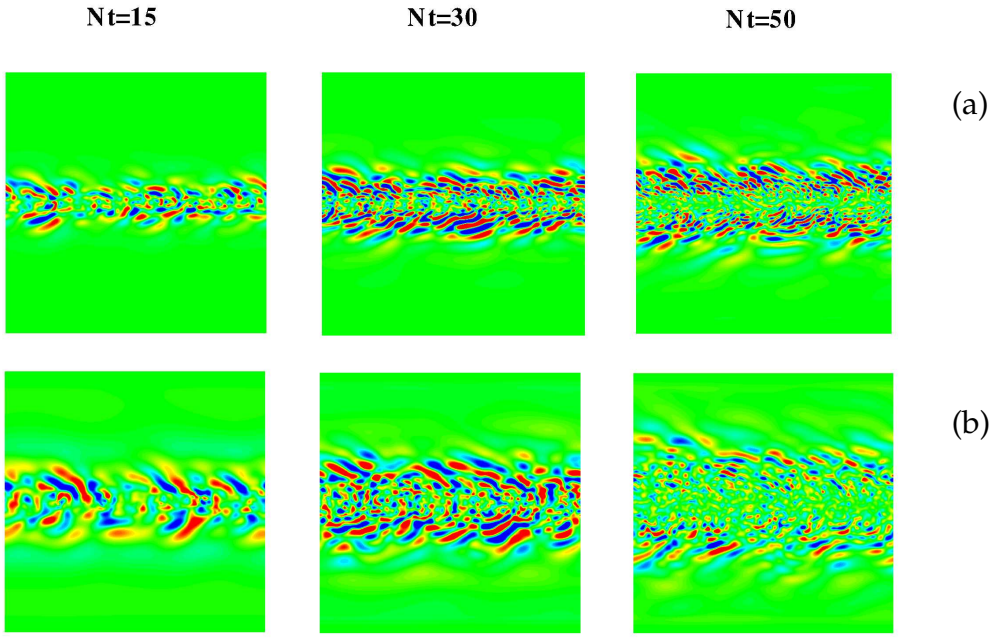

Figure 5.5: Two dimensional contour plot of $\mathbf{\Delta}_z/N$ at different times through $15 < Nt < 50$ on horizontal xy planes at z/D=1.5, 2.3, for (a) R100F4, (b) R100F16. The min./max. ranges for the colorbars of $\mathbf{\Delta}_z/N$ are (a) [-0.05,0.05], (b)[-0.075,0.075].

by Diamessis *et al.* (2010*b*). The Fr-specific of the end of wave emission observed at the low *Re* is also observed here. For example, in the $R100F4$ simulation, energetically significant waves continue to be emitted up to $Nt \approx 90$ whereas for the $R100F16$, intense wave radiations appears to stop by $Nt \approx 70$. By considering Fig. 5.4, 5.5, and 5.6, it is clear that for the same Fr there is a significant increase in the amplitude of the normalized horizontal divergence field with *Re* and a pronounced decrease in the wavelength at the high *Re* relative to the low *Re*.

Finally, it is instructive to examine the structure of the horizontal divergence field on an *xz* plane. The phase line tilt in Fig. 5.7 is similar to that in the shad-

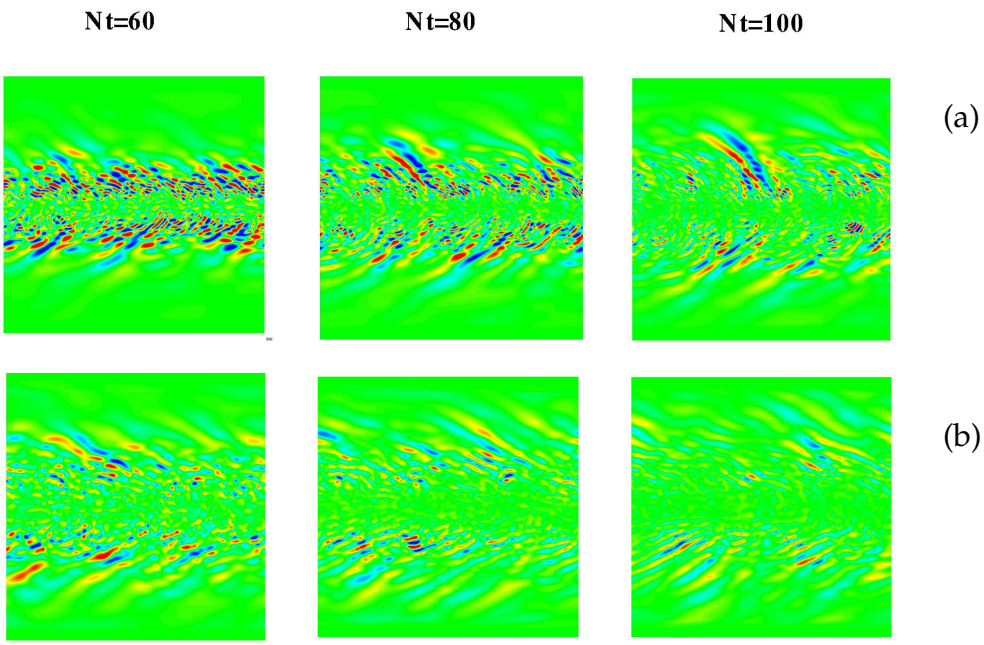

Figure 5.6: Two dimensional contour plot of Δ_z/N at different times through $60 < Nt < 100$ on horizontal xy planes at z/D=1.5, 2.3, for (a) R100F4, (b) R100F16. The min./max. ranges for the colorbars of Δ_z/N are (a) [-0.05,0.05], (b)[-0.075,0.075].

owgraph side views of the wake of the sphere measured by Bonneton *et al.* (1993). The wave packets essentially spread forward (i.e. in the direction of towing) and outwards from the center line. The prolongation of the wave emission, the increase of the amplitude of the normalized horizontal divergence field, and the decrease in the vertical length scales in the $R100F4$ case relative to the $R5F4$ case, seen in Fig. 5.7 are all features consistent with the xy plane visualizations. Finally, for the $R100F4$ simulation, the continued horizontal expansion of the wake core appears to leave a sizeable region of small scale turbulence inside the xz plane. The equivalent manifestation of the lateral growth of the wake at the $R5F4$ seems to be the almost horizontal banded structures concentrated around the wake center line.

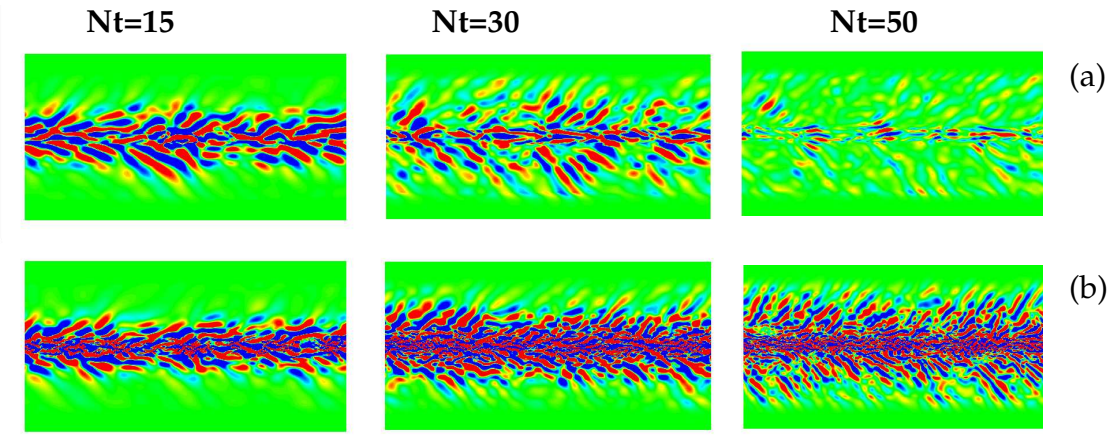

Figure 5.7: Two dimensional contour plot of $\mathbf{\Delta}_z/N$ at different times through $15 < Nt < 50$ on a vertical xz planes at y/D=1.5 for (a) R5F4, (b) R100F4. The min./max. ranges for the colorbars of $\mathbf{\Delta}_z/N$ are (a) [-0.025,0.025], (b)[-0.05,0.05].

There are numerous reasons as to why an xy horizontal plane is the ideal plane for visualizing and quantifying the wave spectral characteristics. First of all, the wake flow is inhomogenous in the spanwise direction and thus analyzing one vertical xz plane at a select y/D distance from the center line is not sufficient to capture any spanwise variability of the wave properties. Even more importantly, the lateral growth of the wake is not limited by buoyancy forces and hence at some point, later in time, the turbulent wake core will cross the analysis plane (regardless of how far away, from the centerline, the plane is chosen) and may possibly contaminate the measured wave properties. Finally, from a computational data analysis standpoint, the limited vertical extent of the domain ($12D$ for $Fr = 4, 16$ and $20D$ for $Fr = 64$) implies that any length scale bigger than $L_z/4$ will be heavily contaminated by edge effects and thus can not be reliably determined.

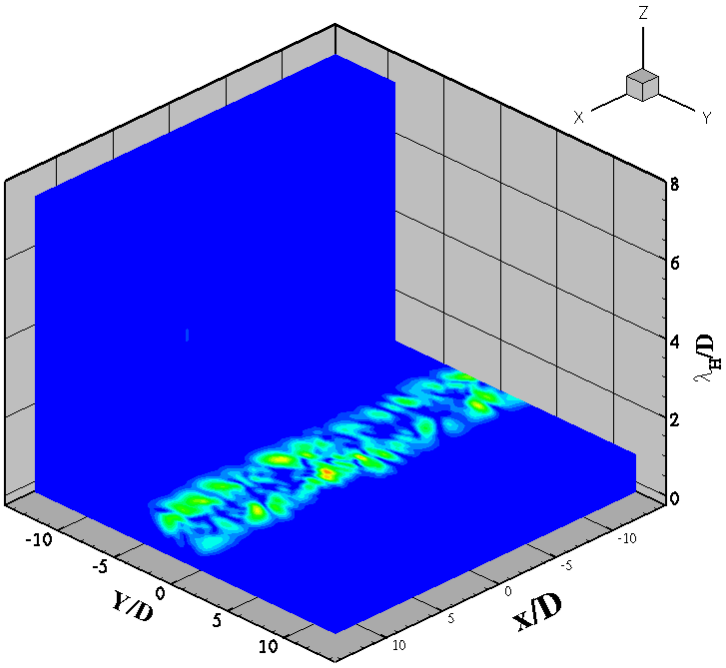

Figure 5.8: Three dimensional isosurface plot of the modulus of the Arc wavelet transform of an xy plane for $R5F4$ at $Nt = 30$. The horizontal axes are the physical space axes x and y. The vertical axis is the horizontal wavelength (normalized by the sphere diameter) corresponding to the wavelet scale.

5.5.2 Spectral characteristics of the internal gravity wave field

We first apply the two dimensional Arc wavelet transform to the horizontal divergence field data on an xy plane above the wake center line, and then search the resulting cube of data (the space-scale domain) for resonance. Figure 5.8 shows a cutaway view through the cube of data resulting from the application of the Arc wavelet to the wave field in Fig. 5.9. The horizontal transect at $\lambda_H/D \approx 1.5$ in the cutaway view shows localized peaks that can be traced back to individual wave packets on the xy plane. Figure 5.10 shows a vertical transect at $y/D = 2.5$ through the modulus cube shown in Fig. 5.8. The plot clearly shows localized regions (bands of influence) where the transform is locally maximized as a result of resonance with wavepackets at the scales

corresponding to the center of the bands. The area of the the bands of influence is clearly proportional to the spatial scale of resonance. The locations of the local maxima on the space-scale plane seem to strongly correlate with the locations of the wave packets marked by arrows in Fig. 5.9 at $y/D = 2.5$. The centers of the influence bands are concentrated around an average length scale of about $\lambda_H/D \sim 1.5$ with deviations (across all peaks) of less than $0.5D$.

The purpose of the analysis is to extract the length scales of the most energetic waves at a given spanwise location on the *xy* plane of interest. Thus, the scales corresponding to those local maxima where the transform modulus is bigger than 50% of the global maximum are averaged and a mean scale is reported at this spanwise location. This conditional averaging acts to filter out local resonance associated with weak wave packets. As the wake-radiated internal wave field is quasi-random in nature, waves of certain scale detected at a particular location may not be detected at the same location in different realizations of the flow with identical, yet slightly different, initial conditions. However, the statistics of the wave scales, such as the mean and r.m.s. deviations, should be repeatable in such realizations.

By virtue of the spanwise symmetry around the center line ($y/D = 0$), it suffices to consider only half of the *xy* plane. Hence, we focus on the (x, $y/D > 0$) half plane. We further limit the search for resonance on the *xy* half plane to limited areas/bands in the spanwise direction where there is significant wave acitivity. The choice of these bands depends mainly on Fr and weakly on Re, for example we focus on $1.5 < y/D < 4.5$ for the $R5F4$ simulation. In order to minimize the search for resonance we sample the transform modulus data at few equally spaced y/D locations within the bands (e.g. a spacing of $1D$ is

chosen for the $R5F4$) to exclude statistically dependent data. The spanwise extent of the search bands is increased with Fr, being $1.5 < y/D < 6.5$ for $R5F16$ and $1.5 < y/D < 8.5$ for $R5F64$. As the wave emission is prolonged at the higher Re (up to $Nt \approx 90$ for $R100F4$) and on account of the continued lateral wake growth, the spanwise extent of the search bands is increased relative to the low Re, being $1.5 < y/D < 6.5$ for $R100F4$ and $1.5 < y/D < 8.5$ for $R100F16$. Finally, to avoid edge effects, we discard the modulus data over a region of length $\approx 2 - 4D$ near the left and right boundaries of the domain.

The results obtained from the five different simulations are shown in Fig. 5.11 and 5.12. As soon as significant wave activity reaches the analysis plane, the horizontal length scale (not shown) remains nearly constant over a short period ($O(5 - 10Nt)$), the duration of which is mainly dependent on Reynolds number, the longer period corresponds to the high Re. Since the arrival time of the internal wave field at the analysis plane is hard to define objectively, we are not showing this initial constant length scale phase. The length scales then transition into a regime where they decay at a uniform rate that mainly depends on Re, but is also weakly dependent on Fr. The decay in the wavelength (and possibly the loss of coherence over time) may be attributed to interference between wavepackets that are emitted from different locations with different wavelengths and frequencies/angles of propagation.

The average power law fit of all the data at the different spanwise sampling locations are shown in Fig. 5.11 and 5.12 as solid lines along with data from only two sampling locations in order to facilitate the interpretation of the results. The mean values of the coefficients of the average power law fits α and β in $\lambda_H/D = \alpha Nt^{\beta}$, along with their standard deviations (r.m.s values) are sum-

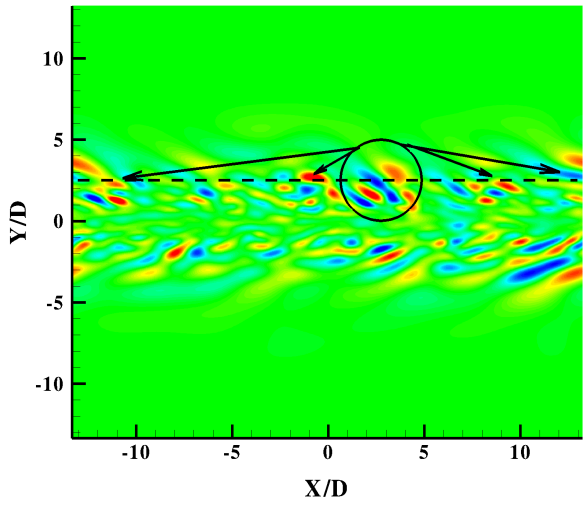

Figure 5.9: The normalized horizontal divergence field on a horizontal xy plane at $z/D = 1.5$ for $R5F4$ at $Nt = 30$. The min./max. ranges for the colorbars are [-0.04,0.04]

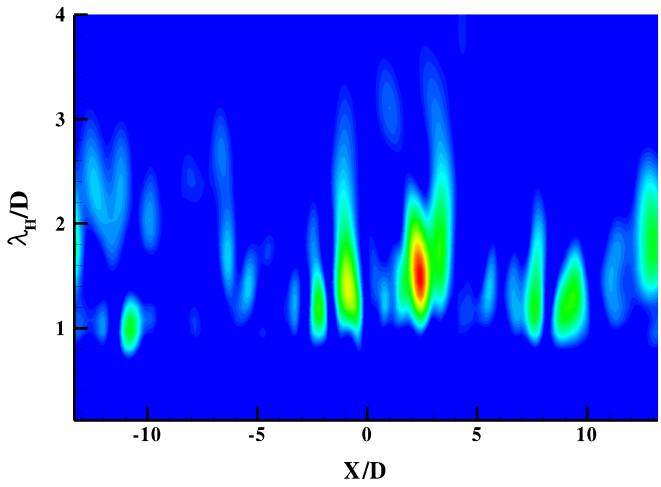

Figure 5.10: A vertical transect through the modulus transform cube (Fig. 5.8) at $y/D = 2.5$.

Table 5.1: Summary of the band averaged power law fit coefficients from the Arc wavelet transforms ($\lambda_H/D = \alpha Nt^{\beta}$)

Simulation	α (mean)	α (r.m.s.)	β (mean)	β (r.m.s.)
$R5F4$	4	0.4	-0.3	0.03
$R5F16$	6.8	1.1	-0.35	0.04
$R5F64$	10.0	1.7	-0.39	0.06
$R100F4$	10.0	1.8	-0.56	0.03
$R100F16$	22.9	2	-0.70	0.02

marized in table 5.1. The Fr driven variations in the decay rates are small and may not be detectable experimentally, for example at the low Re, they may be hard to differentiate from a $1/\sqrt{Nt}$, considering the inevitable experimental error levels.

The horizontal wave length decay rates reported here are significantly different from the $1/Nt$ found experimentally by Bonneton *et al.* (1993) where Fr, Re = $(10/\pi, 8320)$, (4, 10456), (5, 13070). The experimental data plotted in Fig. 8 in Bonneton *et al.* (1993), as commented on by the authors, show large scatter in the length scale data, but in addition to that, the average decay rate by visual observation of their data appears to be noticeably slower than the proposed $1/Nt$. The faster decay rate in the experiments may be a result of the difference between our sampling criteria that only focuses on the most energetic waves. Details of the sampling of the wave field and determination of the wavelength were not reported in Bonneton *et al.* (1993). Finally, a purely empirical $Fr^{1/4}$ scaling seems to accurately collapse all the horizontal wavelength data in all five reported simulations (see Fig. 5.13 and 5.14).

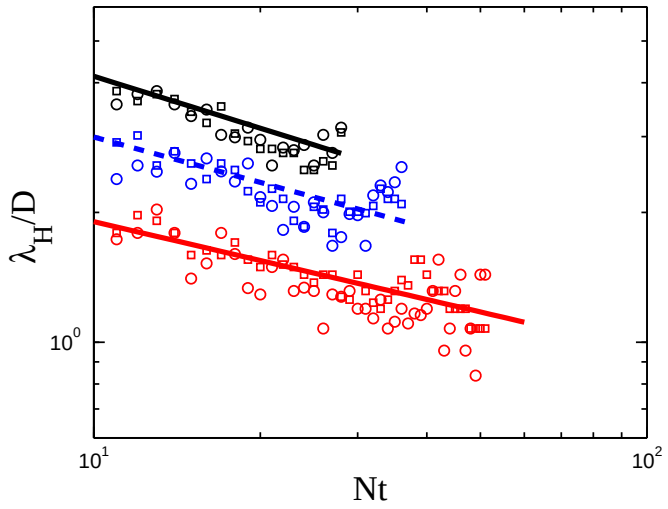

Figure 5.11: The evolution of the normalized horizontal wavelength obtained from the Arc wavelet transform of the horizontal divergence field on a horizontal xy planes at $z/D = 1.5,\ 2.3,\ 3.4$ for $R5F4$, $R5F16$, $R5F64$, respectively. Color coding is as follows: red for $Fr = 4$, blue for $Fr = 16$, black for $Fr = 64$. Circles and squares represent data at $y/D = 1.5,\ 2.5$ for $Fr = 4,\ 16$ and $y/D = 2.5,\ 4.5$ for $Fr = 64$, respectively. Solid lines are band-averaged power law fits.

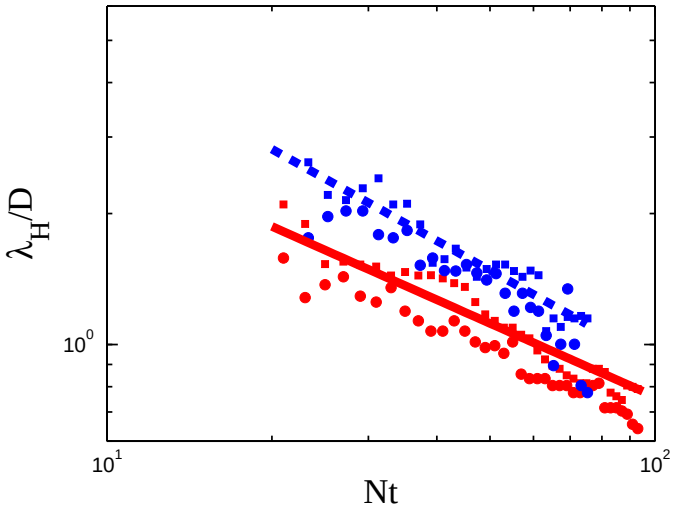

Figure 5.12: The evolution of the normalized horizontal wavelength obtained from the Arc wavelet transform of the horizontal divergence field on a horizontal xy planes at $z/D = 1.5,\ 2.3$ for $R100F4$, $R100F16$, respectively. Legend as in Fig. 5.11.

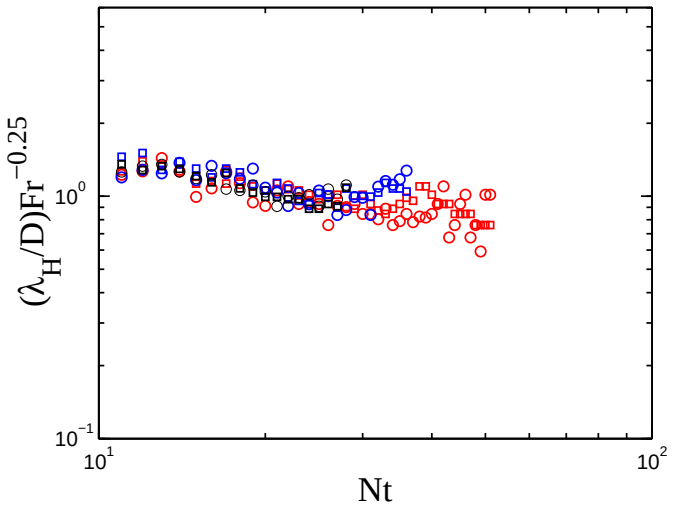

Figure 5.13: Fr scaling of the normalized horizontal wavelength obtained from the Arc wavelet transform of the horizontal divergence field on a horizontal xy planes at $z/D = 1.5, 2.3, 3.4$ for $R5F4$, $R5F16$, $R5F64$, respectively. Legend as in Fig. 5.11

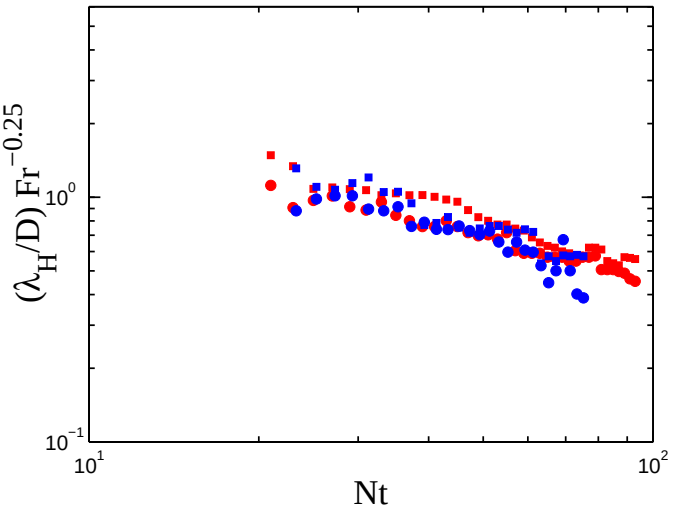

Figure 5.14: Fr scaling of the normalized horizontal wavelength obtained from the Arc wavelet transform of the horizontal divergence field on a horizontal xy planes at $z/D = 1.5, 2.3$ for $R100F4$, $R100F16$, respectively. Legend as in Fig. 5.11.

Careful consideration of the visualizations in Fig. 5.4, 5.5, 5.6 shows that, although the orientation of the dominant wavenumbers of the individual wavepackets vary over space and time, it appears that the wave numbers remain concentrated around a single mean direction with slight deviations therefrom. Accordingly, it is hoped that interrogating the two dimensional signal with *Morlet2D* wavelet at this mean direction may capture the bulk of the wave energy. Identification of the mean direction, referred to hereafter as ϕ allows us to better understand the dominant orientation of the wavepackets on the horizontal plane and, if desired, allows direct decomposition of the horizontal wave number into its streamwise and spanwise components.

The statistical principles for the determination of a mean angle from a collection of measured angles is explained in detail in appendix B. Essentially the technique involves interrogation of the signal (the horizontal divergence field on horizontal *xy* planes) using the *Morlet2D* wavelet transform at several angles where local resonance is sought. Remarkably, all resonant angles, thus determined, were found to be highly concentrated around mean directions (for more details see appendix B). The mean directions (also called "azimuth angles") are summarized in table 5.2 along with power law fits of the horizontal length scales obtained from *Morlet2D* wavelets. The azimuth angles in all five cases were in the range $56 - 60^{\circ}$ with no systematic dependence on either Re or Fr. The power law fits obtained from the *Morlet2D* wavelets are indeed in close agreement with those obtained from the non-directional Arc wavelets , with maximum length scale deviations of less than 15%, confirming our expectation that there are prevalent mean directions carrying the bulk of the wave field energy in all the simulations. Furthermore, a scatter plot of the horizontal wavelengths (Fig. 5.15) obtained from the Arc and *Morlet2D* wavelets, from all

Table 5.2: Summary of the azimuth angles and the band averaged power law fit coefficients from the *Morlet2D*wavelet transforms (ϕ , $\lambda_H/D = \alpha N t^{\beta}$)

Simulation	ϕ	α (mean)	α (r.m.s.)	β (mean)	β (r.m.s.)
$R5F4$	60°	3.5	0.6	-0.3	0.02
$R5F16$	56°	6.5	0.8	-0.38	0.03
$R5F64$	60°	9.7	2.0	-0.4	0.06
$R100F4$	59°	8.0	1.5	-0.52	0.03
$R100F16$	60°	18.4	4	-0.66	0.03

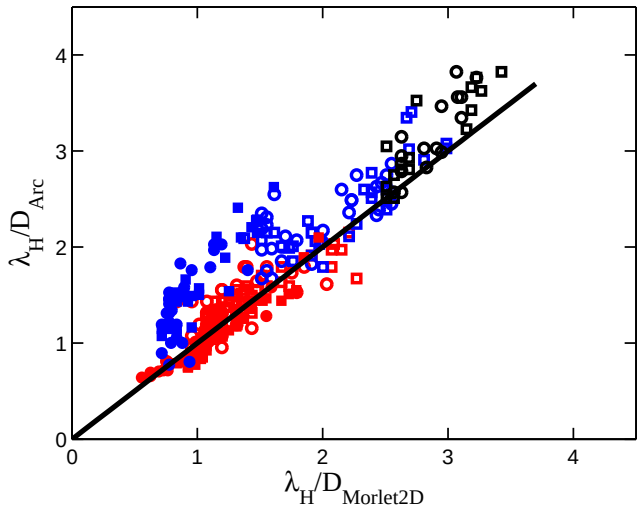

Figure 5.15: Scatter plot for the horizontal length scales obtained from the Arc and *Morlet2D* wavelet transforms for the five different simulations. Legend as in Fig. 5.11 with filled symbols for $Re = 10^5$ data and open symbols for $Re = 5 \times 10^3$. The black solid line is the identity line.

five simulations, shows a high concentration of the data in the vicinity of the identity line.

In view of the limitations of wavelet analysis on the *xz* plane, detailed in §5.5.1,

we use the internal gravity wave dispersion relation (equations 1.4 and 1.5) to determine the vertical wavelength. As this approach requires that the frequency of the waves to be known, we now seek ways to understand and quantify the distribution of the wave frequency over the analysis planes.

Figure 5.16, 5.17 show streamwise-time $x - t$ diagrams extracted at ($z/D = 1.5$, $y/D = 1.5$) for $R5F4$ and $R100F4$, respectively. The diagrams mimic a hypothetical experiment in which large number of sensors are placed next to one another in the streamwise direction, at a fixed distance from the wake centerline in the vertical and spanwise directions, to continuously record the horizontal divergence field over the duration of the experiment. The most notable feature in Fig. 5.16 (the low *Re*) is the prevalence of a nearly constant wave period (the distance between two consecutive points , along the time axis, having the same phase) whereas Fig. 5.17 (the high *Re*) shows somewhat continuous decrease in the wave period. In addition, at early time the wave period for the high *Re* seems to be larger than the wave period in the low *Re*. The selection of a narrow range of frequencies is in general agreement with all previous studies of turbulence generated IGWs..

As we only need to determine the frequency of the waves, there is no need for two-dimensional wavelet transforms of the $x - t$ diagram. Instead, one dimensional transforms in the time coordinate direction are sufficient for this purpose. We extract 21 time series from the $x - t$ in the range $x/D \in [-10, 10]$, each sampling location spaced by a sphere diameter, and take their one dimensional wavelet transforms using the complex Morlet wavelet. The modulus of the transform of a time series is essentially a function of time and frequency.

For a given time series, at a specific x/D, we conduct a one dimensional search at a given time to determine the frequency that maximizes the modulus of the transform. Now, at a given Nt, the resonant frequencies from all time series at the different x/D distances, are conditionally averaged. Frequencies where the associated values of the modulus of the transform is below 50% of the global maximum across all downstream locations, are excluded from the averaging. The frequencies are finally transformed into equivalent phase line tilt angles (also called "polar angle"; θ) through the dispersion relation (equation 1.4). To capture the spanwise variability of the frequencies we repeat the procedure outlined above for $x - t$ diagrams extracted at multiple spanwise locations (on the same xy analysis plane) within the bands of significant wave activity.

Figure 5.18 shows the evolution of the phase line tilt angle obtained from the one dimensional wavelet transform for the five simulations. Remarkably, the angles (and the implied frequencies) and their evolution seems to faithfully reproduce the general features found in Fig. 5.16 and 5.17. The angles, being in the range $\theta = [27 - 50]$ are in good agreement with previous studies of turbulence generated IGWs (Sutherland & Linden, 1998; Dohan & Sutherland, 2003, 2005; Aguilar, Sutherland & Muraki, 2006; Taylor & Sarkar, 2007; Munroe & Sutherland, 2008; Pham, Sarkar & Brucker, 2009), implying that the properties of these waves are universal, independent of the specific underlying turbulent process (such as wakes, boundary layers, and oscillating grid). Nevertheless the current results clearly establish the following:

- At a given Re, any Fr dependence of the phase line tilt angles is weak.
- At low Re where viscous effects are important, the phase line tilt angles are close to 35°, the angle that maximizes the group velocity of the waves

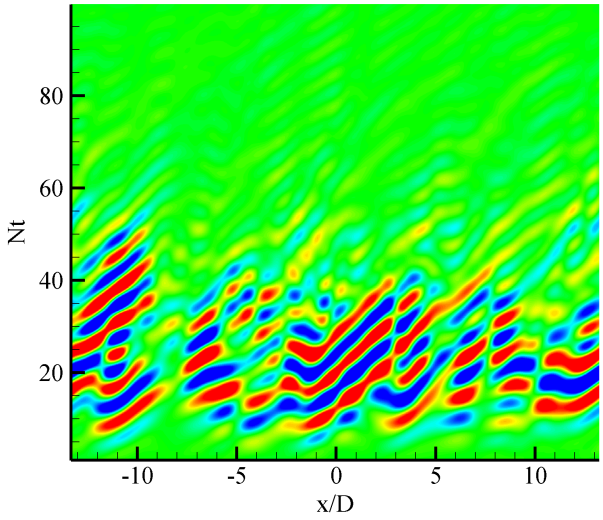

Figure 5.16: Streamwise-time ($x - t$) diagram of the normalized horizontal divergence field at $y/D = 1.5$, $z/D = 1.5$ for $R5F4$.The min./max. ranges for the colorbars of $\mathbf{\Delta}_z/N$ are [-0.025,0.025].

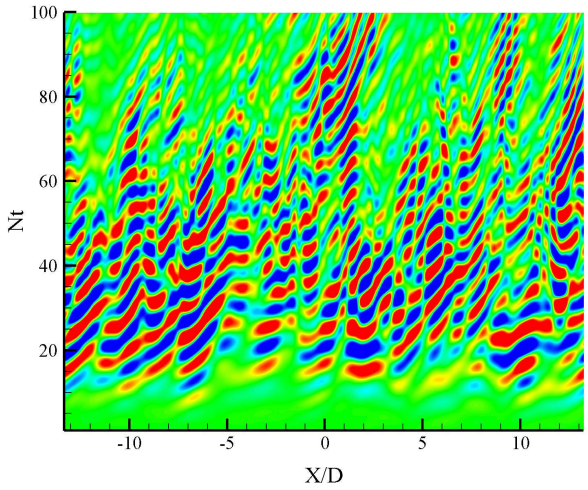

Figure 5.17: Streamwise-time ($x - t$) diagram of the normalized horizontal divergence field at $y/D = 1.5$, $z/D = 1.5$ for $R100F4$.The min./max. ranges for the colorbars of $\mathbf{\Delta}_z/N$ are [-0.05,0.05].

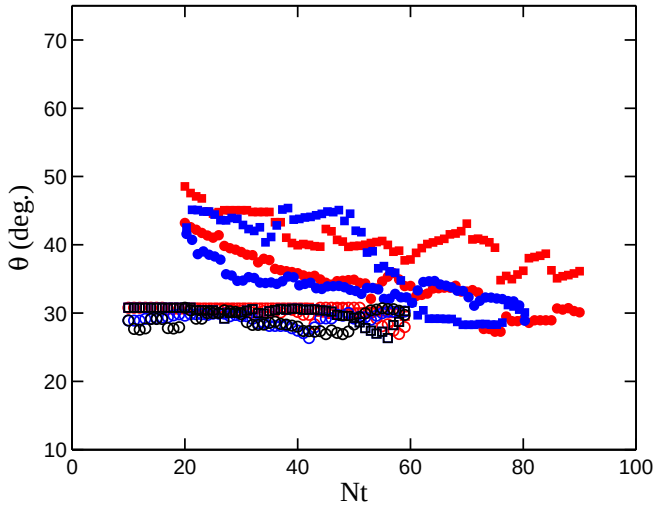

Figure 5.18: Evolution of the phase line tilt/polar angle obtained from the one dimensional wavelet transforms. Legend as in Fig. 5.11 with filled symbols for $Re = 10^5$ data and open symbols for $Re = 5 \times 10^3$.

and hence waves propagating at these angles will experience the minimum viscous decay (Sutherland, 2005).

- At large enough *Re*, where viscous effects are negligible, the the phase line tilt angles , especially around the time of maximum wave activity, are close to 45°, the angle that maximizes the momentum extraction from the wake shear profile (Sutherland, 2005), and thus waves that are capable of exerting the maximum drag on the wake prevail.

Table 5.3 and 5.4 summarizes the coefficients of the power law fits of the tangent of the phase line tilt angle and the vertical length scales obtained from equation 1.5.

Remote detection of subsurface signature of IGWs depends critically on the vertical component of the group velocity of these waves; the velocity by which

Table 5.3: Summary of the band averaged power law fit coefficients for the tangent of the polar angles ($tan(\theta) = \alpha N t^{\beta}$).

Simulation	α (mean)	α (r.m.s.)	β (mean)	β (r.m.s.)
$R5F4$	0.6	0.01	0	0.0
$R5F16$	0.59	0.02	0	0.0
$R5F64$	0.61	0.02	0	0.0
$R100F4$	1.7	0.30	-0.19	0.04
$R100F16$	1.9	0.32	-0.16	0.03

Table 5.4: Summary of the band averaged power law fit coefficients for the normalized vertical length scales ($\lambda_z/D = \alpha N t^{\beta}$).

Simulation	α (mean)	α (r.m.s.)	β (mean)	β (r.m.s.)
$R5F4$	6.7	0.5	-0.3	0.03
$R5F16$	11.5	1.2	-0.35	0.04
$R5F64$	16.4	1.9	-0.39	0.06
$R100F4$	5.9	1.2	-0.37	0.04
$R100F16$	12.0	2.1	-0.54	0.03

the wave energy propagates in the vertical (can be estimated from equation 1.7). Figure 5.19 shows the evolution of the estimated vertical group velocity in all five simulations. The time series clearly shows that the group velocity is mainly dependent on Fr, being smaller at the higher Fr. Although equation 1.7 shows that the group velocity is a function of the buoyancy frequency (or equivalently Fr) , the length scales, and the phase tilt angles (the length scales and the angles themselves are functions of both Re and Fr), it appears that Fr effects overshadow a very weak Re dependence. An empirical $Fr^{-}3/4$ scaling (Fig. 5.20) appears to accurately collapse all the data from the five simulations,

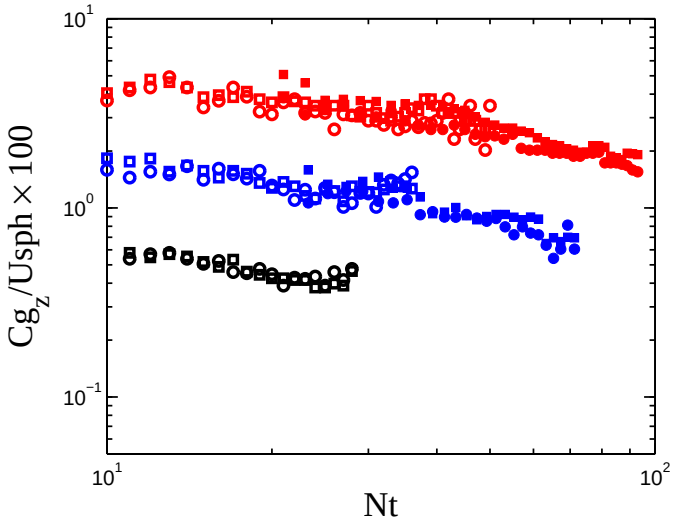

Figure 5.19: Evolution of the vertical group velocity obtained from the five simulations. Legend as in Fig. 5.11 with filled symbols for $Re = 10^5$ data and open symbols for $Re = 5 \times 10^3$.

confirming the lack of any Re dependence. The time-average vertical group velocity over (the interval of significant wave emission) $10 < Nt < 50$ for $R5F4$ is about 3.5% of the sphere velocity. Not surprisingly, nearly the same velocity estimate is obtained over the interval $20 < Nt < 90$ for the $R100F4$.

5.5.3 Degree of nonlinearity

The steepness of the internal wave field, defined as $A = A_\zeta/\lambda_x$ for a two-dimensional wave field is a measure for the nonlinearity of the waves and their potential for resonant wave-wave interactions and convective breaking. For a three dimensional wave field, we define $A = A_\zeta/\lambda_H$ as a more appropriate measure for the steepness of the underlying wave field. Equation 5.5 shows that the displacement amplitude can be calculated if the frequency and the vertical wavenumber are known. On account of the spatial variability of the horizon-

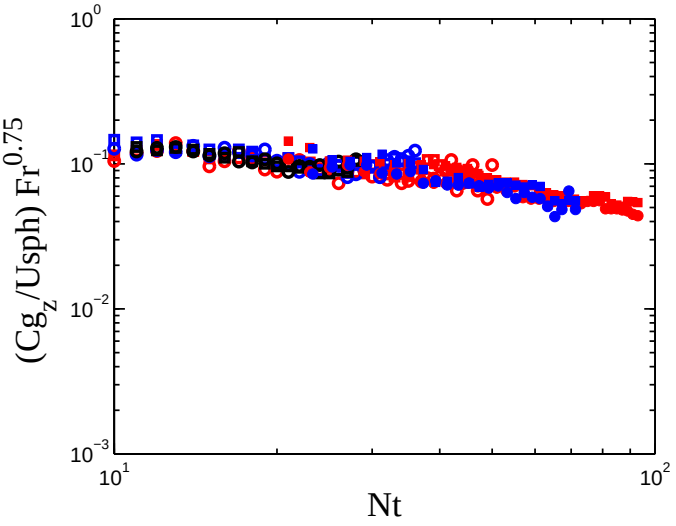

Figure 5.20: Fr scaling of the vertical group velocity obtained from the five simulations. Legend as in Fig. 5.11 with filled symbols for $Re = 10^5$ data and open symbols for $Re = 5 \times 10^3$.

tal divergence field, there is a need to define an average amplitude to be used in 5.5. While a plane average will tend to smooth out local maxima associated with wavepackets having large horizontal divergence amplitude, a global maximum (the maximum amplitude over the whole *xy* plane) will also tend to over-estimate the steepness of a wave field with few isolated local maxima. As a result, it seems that the most appropriate definition would be to conditionally average the local maxima over the bands of significant wave activity.

Figure 5.21 shows the estimated wave steepness in all five simulations. The plot reproduces some of the features of the wave emission process observed in Fig. 5.4, 5.5, 5.6. In particular, at a given *Re*, increasing Fr leads to a steeper wave field. For example, Fig. 5.21 shows that the peak steepness increases from $\sim$ 1% in the $R5F4$ case to $\sim$ 1.8% in the $R5F16$ case. An even larger increase in the peak steepness can be clearly seen in the $R5F64$ case relative to the $R5F16$ case. Also, at a given Fr, increasing *Re* leads to a significant increase in the

peak steepness. For example, the peak steepness in $R5F4$ is $\sim$ 1% whereas for $R100F4$, the peak steepness is $\sim$ 2.2%. Finally, the peak steepness and the cessation of significant wave emission are attained at earlier Nt as Fr increases. In addition to that, increasing Re leads to a significant delay in attaining the peak steepness (at a given Fr) because of the associated prolongation of the NEQ regime. For example, the peak steepness for $R5F4$ is attained around $Nt \sim 20$, whereas for $R100F4$ the peak is attained around $Nt \sim 40$.

Finally, our results show that (see Fig. 5.22) the maximum vertical displacement amplitude attained by the wake generated waves is relatively large, being 1 – 7% of the horizontal wavelength (10 – 70% of the self acceleration limit) in the low Re simulations and 2 – 4% of the horizontal wavelength in the high Re runs (20 – 30% of the self acceleration limit). The results in $R5F4, R5F16, R100F4, R100F16$ are in close agreement with Dohan & Sutherland (2003) where the steepest measured waves were in the 2 – 4% range which corresponded to 25% of the instability limit.

5.6 Discussion

The use of two-dimensional CWT allowed us to determine the spectral properties of a turbulent wake generated internal wave field. In particular, the horizontal wavelengths of the energetically dominant wavepackets were comparable to the sphere diameter ($O(2 - 4D)$) and decayed over time at a rate that is dependent on both Fr and Re, but in general is significantly slower than the $1/Nt$ predicted by the impulsive wave theory (Bonneton, Chomaz & Hopfinger, 1993) which does not even imply any dependence on either Fr or Re. The

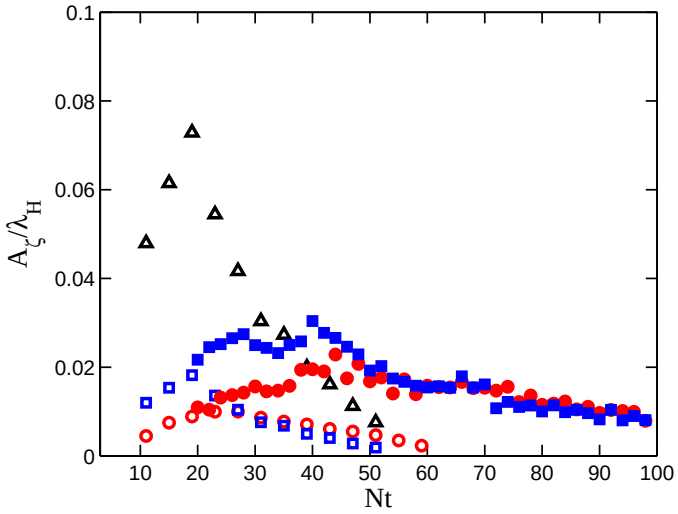

Figure 5.21: Evolution of the internal wave field steepness from the five simulations. Color coding is as in Fig. 5.11 with filled symbols for $Re = 10^5$ data and open symbols for $Re = 5 \times 10^3$.

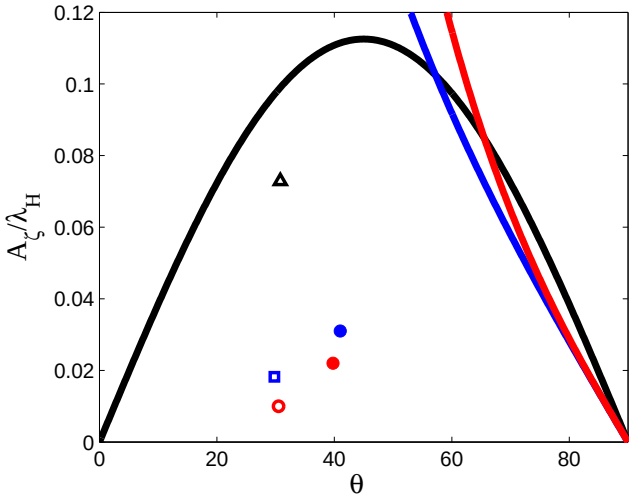

Figure 5.22: Comparison of the maximum wave steepness in all five simulations to the internal wave instability limits, plotted against the phase line tilt angle θ. Symbols' color coding is as in Fig. 5.11 with filled symbols for $Re = 10^5$ data and open symbols for $Re = 5 \times 10^3$. Black solid line represents the self acceleration limit while the blue solid line indicates the overturning limit. Finally, the red solid line represents the convective breaking limit.

horizontal wavelengths were also dependent on both Fr and Re such that they increase with increasing Fr and decreasing Re. The Fr scaling was empirically determined to be $Fr^{1/4}$.

The orientations of the wave numbers on a horizontal plane above the wake center line were concentrated around a mean direction of $\sim 60^{\circ}$ independent of both Fr and Re. One-dimensional CWT based on the complext Morlet wavelets allowed us to determine the internal wave frequencies and phase line tilt angles from multiple time series. Surprisingly, for all low Re simulations, the angles were constant over time and equal to $\sim 31^{\circ}$, i.e. close to the angle that maximizes the vertical group velocity of the wave field ($\sim 35^{\circ}$), which indicates that the prevalence of waves propagating at this angle in the low Re simulations, where viscous effects are more strongly "felt" by the waves, is because they experience the minimum viscous decay. These angles are very close to the $\sim 26.6^{\circ}$ angle that minimizes the viscous decay according to the viscous decay model proposed by Taylor & Sarkar (2007). On the contrary, at the high Re, where the viscous time scale is 20 times bigger than at the low Re and hence viscous effects are minimal, the angles exhibited a slow decay rate, with the waves at the most intense wave emission period propagating at angles $\sim 45^{\circ}$, again nearly independent of Fr. Waves propagating at $\sim 45^{\circ}$ are associated with maximum vertical flux of horizontal momentum and thus they are most capable of exerting the maximum drag on the turbulent wake. This in turn suggests that, at high Re wave emission by the wake is governed by a resonant feed back between the waves and the turbulent wake, whereby waves that are most capable of modifying the turbulent wake region act back on it to enhance their emission. To the best of our knowledge, the clear identification of Re as the basis for the selection mechanism of wave propagation angles is a novel

result that has not been reported before in the literature.

Knowledge of the propagation angles and the horizontal wavelengths allowed us to estimate the vertical length scales (through the linear dispersion relation) and the vertical group velocity. Although the vertical length scales at $R5F16$ were comparable to the height of the vertical space available for wave propagation, visualization of the wave field on the xz plane showed that the wave field is strongly localized in the vertical, with vertical envelope sizes of $\sim 1/2\lambda_z$ and hence confinement was not an issue. This indeed suggests that the current results can be supplemented by another wavelet type that enables the determination of the size of the wavepacket envelopes where the most energetically significant oscillations reside. Daubechies or Mexican hat wavelets seem to be attractive for this purpose

The wave displacement amplitude was shown to increase with both *Re* and Fr. While the intuitive dependence of the displacement amplitude on Fr is supported by all the few available experimental studies, the dependence on *Re* has not yet been established experimentally. For a fixed *Re*, Increasing Fr amounts to decreasing the strength of the stratification as Fr is inversely proportional to N. Since the horizontal wavelength increases with Fr, the only plausible explanation to the observed increase in the steepness with Fr is an even faster increase in the displacement amplitude A_ζ with Fr. This is in general agreement with the experimental results of Dohan & Sutherland (2003) for IGWs generated by stationary turbulence, where the authors found that $A_\zeta \sim N^{-1.68}$ where $N \in [0.75 - 1.23]$ rad/s. For $F \in [4 - 10]$ Bonneton *et al.* (1993) found that $A_\zeta \sim F^2$ (or equivalently $A_\zeta \sim N^{-2}$) for internal waves generated in the wake of a towed sphere. On the other hand, for an internal wave field generated

by a towed sphere below a thermocline Robey (1997) found that the increase in the measured internal wave amplitudes with Fr is closer to a linear than a quadratic.

In our simulations, although it is hard to accurately estimate the scaling of the maximum vertical displacement with Fr (due to the limited number of simulations), linear least square fit (not shown) of the maximum wave displacement in the three reported simulations at the low Re shows a $Fr^{0.98}$ scaling, i.e. close to the linear scaling supported by the measurements of Robey (1997). It is to be noted that in the experiments of Bonneton *et al.* (1993), changing Fr is accompanied by a change in Re. In fact Bonneton *et al.* (1993) argue that the the dependence of the displacement amplitude on Re should be weak as the amplitude is determined by the scale of the energy containing eddies in the wake at the onset of collapse which is independent of Re, but they do not provide a clear evidence to support this argument.

Clearly any Re based arguments/scaling requires a detailed understanding of the wave generation mechanisms which are not yet well understood. The results, in their core, indicate that simplified models based on wake collapse or the superposition of impulsive mass source(s) Bonneton *et al.* (1993); Voisin (1991, 1994) may need to be reexamined.

Finally, the steepness of the wave fields were moderately large in the $Fr = 4$, 16 simulations, being in the range $10 - 30\%$ of the wave instability limit, however, for the $Fr = 64$ simulation the steepness was as large as 70% of the instability limit. The large steepness determined for the $Fr = 64$ simulation cast some doubt on the reliability of the wave propagation angles and vertical length

scales estimated from the linear dispersion relation, in this particular simulation, as it is strictly valid for low amplitude internal waves. Direct calculation of the vertical length scales from the *xz* planes in our simulations is not reliable either as the vertical window size is comparable to the vertical wavelength. Increasing the vertical height of the domain to enable accurate wavelet analysis on the *xz* plane is beyond the available computational resources.

Like the wave displacement amplitude, the steepness increases with both Re and Fr, indicating that extrapolating the results to navally relevant conditions, where Re and Fr are typically larger than the values considered here, implies that the waves generated behind the naval submarines are more prone to nonlinear wave-wave interactions and breaking. Thus, the proposed mechanisms of remote breaking events, driven by submerged-turbulence-driven IGW radiation, proposed by Keeler *et al.* (2005) could be feasible in the ocean and might be enhanced upon the interaction of these waves with critical layers (Winters & D'Asaro, 1989, 1994) and density jumps (Delisi & Orlanski, 1975).

CHAPTER 6

NUMERICAL GENERATION AND EVOLUTION OF LARGE AMPLITUDE INTERNAL WAVES

6.1 Problem description

We are primarily interested in examining the generation and propagation (and breaking, when desired) of a large-amplitude hydrostatic IGW packet such as that considered in previous investigations (Winters & D'Asaro, 1989; Slinn & Riley, 1998*a*). The horizontal wave-length of such a wave is much bigger than its vertical wave-length and accordingly it has near-horizontal group velocity. Note that the findings of this study are also relevant to non-hydrostatic IGWs.

The governing equations are the two-dimensional, incompressible, Navier-Stokes equations under the Boussinesq approximation (equations 3.1- 3.3, where for a two dimensional field, $\mathbf{u} = (u, w)$) with forcing terms $F_{\mathbf{u}} = (F_u, F_w)$ and F_ρ added to the right hand side of the momentum (3.1) and the density (3.2) equations, respectively. The forcing terms are patterned after the initial condition often used in IGW process studies, a wave packet at time $t = 0$ as represented by a solution of the inviscid, non-diffusive linear internal wave equations (Winters & D'Asaro, 1989):

$$u_w(x, y, t = 0) = U_o \left(-\frac{Am}{k} F(z) cos\phi - \frac{A}{k} F'(z) sin\phi \right), \tag{6.1}$$

$$w_w(x, y, t = 0) = U_o A F(z) cos\phi, \tag{6.2}$$

$$\rho_w(x, y, t = 0) = -\left| \frac{d\rho}{dz} \right| \frac{U_o A}{\omega} F(z) sin\phi, \tag{6.3}$$

where $\phi = kx + mz$, m and k are the vertical and horizontal wave numbers, ω is the angular frequency, U_o is a reference velocity scale and A is the non-

dimensional amplitude of the vertical velocity, such that AU_0 is the vertical velocity amplitude of the generated wave packet. Consistent with the definition used by Slinn & Riley (1998*a*) in their study of continuously forced IGW trains, the forcing terms, $F_{\mathbf{u}}$ and F_ρ , result from dividing (6.1)- (6.3) with a reference timescale L/U_o (where the reference lengthscale is $L = \lambda_x = 2\pi/k$) and replacing the phase argument with $\phi = kx + mz - \omega t$. We use the same localization function used by Slinn & Riley (1998*a*) and Winters & D'Asaro (1989):

$$F(z) = \exp\left(-\frac{(z - z_{cen})^2}{2\sigma^2}\right), \tag{6.4}$$

which, however, we recast in terms of the half-height σ of the localization function. The particular choice of σ is such that the Gaussian envelope of this function fits about four vertical wavelengths.

6.2 Numerical simulations summary

The baseline case around which all simulations are designed is patterned after that considered by the critical level interaction study of Winters & D'Asaro (1989). The problem geometry is illustrated in figure 6.1. Two possible configurations are considered in a linear stratification: one where the generated IGW freely propagates away from the generation region and one where it encounters a Gaussian jet that is positioned several vertical wave-lengths away from the wave source. The four governing parameters, defined in terms of the wave properties, are the wave-based Reynolds number, $Re_w = C\lambda_x/\nu$ (where $C = \omega\lambda_x$ is an approximate horizontal phase speed) and Richardson number, $Ri_w = (N\lambda_x/C)^2$, vertical-to-horizontal wavenumber ratio m/k and the non-dimensional vertical velocity amplitude A. To enable a straightforward comparison with the work of Winters & D'Asaro (1989), we also consider an

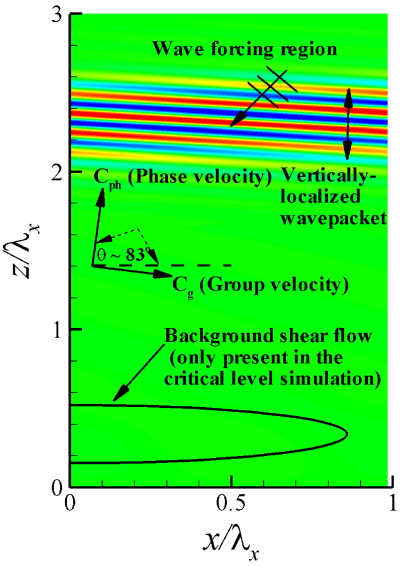

Figure 6.1: Schematic of problem setup: a vertically localized IGW is generated in the forcing region and allowed to freely propagate downward. In the critical level simulation, a Gaussian background shear flow is positioned near the bottom of the computational domain.

alternative Richardson number denoted by $Ri = (N\lambda_x/U_o)^2$. Note that throughout this chapter, ω and N are used in units of *rad/sec* (including the definitions of Ri_w and Re_w). For the purpose of comparing with Winters and D' Asaro, the definition of Ri considers N in units of Hz. Table 6.1 summarizes the values of the parameters used in the baseline case for the free propagation simulations.

It is emphasized that, for the baseline case, $Ri = 1$, $Re_w = 1.5 \times 10^6$, $m/k = 8$ and $A = 0.015$. For the particular choice of m/k, the wave number vector is inclined at an angle $\theta = \arctan(m/k) \approx 83^\circ$ to the horizontal. The value of A in the base case, which is the same as in the large amplitude case studied by Winters & D'Asaro (1989), is such that the steepness of the wave field is slightly below the overturning limit (defined as $\cot\theta/(2\pi)$ in Sutherland (2001)) for the particular

Table 6.1: Parameter values used in the base-case simulation

Parameter	Value
Ri	1
Ri_w	65
Re_w	1.5×10^6
Pr	1
m/k	8
A	0.015
L_x/λ_x	1
L_z/λ_x	3
σ	$L_x \sqrt{(0.21)^2/(-2\ \ln(1/2))}$
z_{cen}/L_z	0.8

angle θ. Finally, an additional set of simulations is considered where the stratification frequency N is increased by a factor of 4, leading to a value of $Ri = 16$ but the same value of $Ri_w = 65$.

The rectangular computational domain has dimensions L_x and L_z. In all simulations, L_x is chosen to accommodate one horizontal wavelength, with the exception of the runs investigating the effect of horizontal localization where L_x is adjusted accordingly (see §6.3.2). L_z is selected to allow for a domain where the generation region is sufficiently far from the top and bottom boundaries to avoid unwanted reflections and allow sufficient distance for the wave to propagate downward through the ambient fluid.

In all simulations, the forcing is turned on and off impulsively (i.e. without any gradual ramp-up and ramp-down in amplitude) and is kept active for ex-

actly one wave period, up to time $T_w = 2\pi/\omega$. The resulting vertically localized wave packet, hereafter referred to as the "mature wave-packet" is expected to have the specified frequency and wave lengths and to propagate downward with the group velocity predicted by the linear theory. Through a series of preliminary runs, the forcing amplitude input to the numerical model is iteratively adjusted so that by the end of the forcing period, the mature wave packet will have the nominal vertical velocity amplitude AU_0.

The baseline grid resolution for the free propagation simulations consists of 64 grid points in the horizontal and 25 vertical subdomains of equal height and uniform order of polynomial approximation of 40, for a total of 1025 vertical grid points.

6.3 Results

6.3.1 Horizontally periodic and vertically compact wave packet

We first examine results from fully nonlinear numerical simulations for the baseline case of a horizontally periodic and vertically compact IGW ($Ri = 1$). Two-dimensional contours at $t = 5T_w$ of the horizontal velocity field (fig. 6.2) show a homogeneous horizontal band of negative flow created behind the rear of the wave packet. Focusing on one-dimensional vertical transects and as the generated wave packet moves downwards, a progressive reduction of its amplitude is observed along with strong structural modulations and distortions

of its rear flank (see figure 6.3). By $t = 5\ T_w$, the wave packet has decayed to nearly half its originally prescribed amplitude. Note that the asymmetry that develops in the wave envelope prevents a consistent/accurate definition of the wave amplitude at $t = 5\ T_w$.

Such a relatively weak and structurally modified wave packet may not be suitable for numerical simulations directed towards exploring the amplitude sensitivity of strong wave intensification and breaking. Presumably, the decay of the wave packet's amplitude can be compensated for by the use of larger initial forcing amplitude. However, since the wave amplitude considered here is very close the overturning limit at the given wave number orientation angle, the initial amplitude cannot be increased any further without risking the breaking of the wave at the source.

Figure 6.4 shows the evolution of the mean horizontal velocity profile, defined as

$$U(z,t) = \frac{1}{\lambda_x} \int_0^{\lambda_x} u'(x',z,t)dx' \quad , \tag{6.5}$$

during the wave generation phase. As is visible in figure 6.4 and also in contour plots of the instantaneous horizontal velocity at much later times (not shown here), the mean flow is associated with two counter-flowing horizontal jets that develop in the forcing region. As shown in the subsequent discussion of §6.4.3, the negatively-oriented jet remains localized in the forcing region as a residual mean flow. It is found to grow nonlinearly with time by, apparently, depleting the IGW packet of its energy and producing strong structural modulations. Finally, §6.4.3, also establishes that the positive component of the horizontal jet corresponds to what has been identified in previous studies as the mean flow induced by the propagating wave.

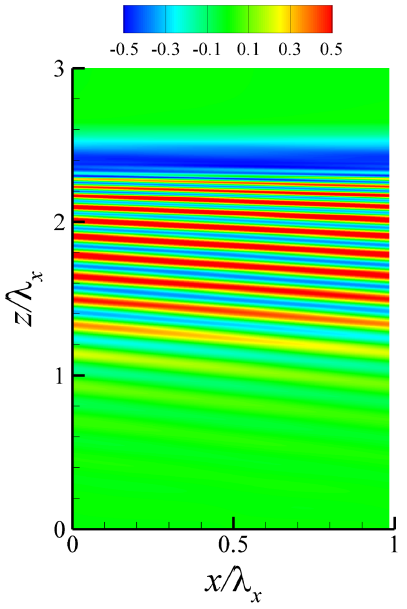

Figure 6.2: Two-dimensional contours of the horizontal velocity field at $t = 5T_w$ in a fully nonlinear simulation of a horizontally periodic, vertically localized wave packet, for $Ri = 1$ (contours are normalized by the horizontal velocity amplitude $A_u = AU_o m/k$ at $t = T_w$).

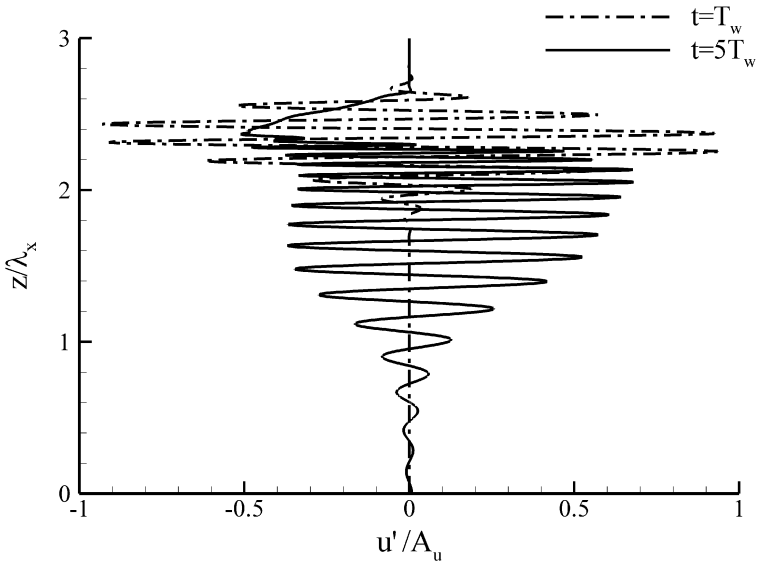

Figure 6.3: Vertical profile of the instantaneous horizontal velocity at $x = L_x/2$ at $t = T_w$and $5T_w$ in a fully nonlinear simulation of a horizontally periodic, vertically localized wave packet, for $Ri = 1$.

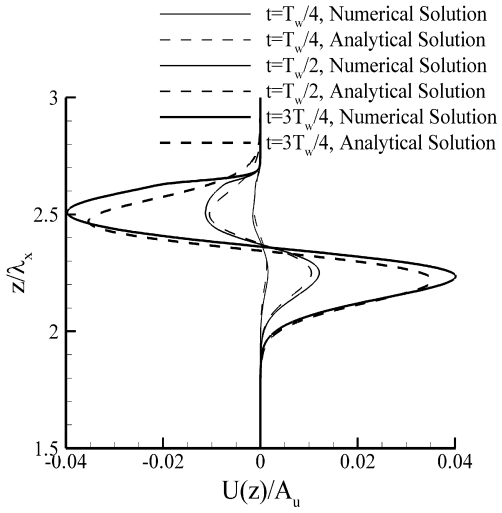

Figure 6.4: Comparison of the analytical and numerical solutions of the mean flow evolution during the wave generation phase in a fully nonlinear simulation of a horizontally periodic, vertically localized wave packet, for $Ri = 1$.

An additional simulation, similar to the one described above has been run where all parameter values are kept the same, except for the the Brunt Vaisala frequency, N, which is now quadrupled ($Ri = 16$). In this case, the highly nonlinear near-source interaction of the IGW with the residual mean flow produces only a 20% decay of the wave's initial amplitude and significantly weaker structural modulations of the rear flank of the packet (figure 6.5).

6.3.2 Effect of horizontal localization

By virtue of the design of the forcing functions described in §6.1, the resulting IGW packets are infinitely periodic in the horizontal. In the laboratory and in nature, a more realistic wave source will have a finite extent not only in the vertical but also in the horizontal, thus generating waves that are localized in

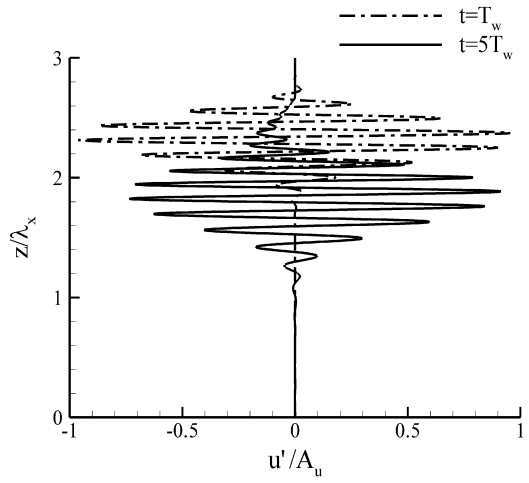

Figure 6.5: Vertical profile of the instantaneous horizontal velocity at $x = L_x/2$ compared at $t = T_w$ and $5\,T_w$ in a fully nonlinear simulation of a horizontally periodic, vertically localized wave packet, for $Ri = 16$.

the horizontal. Such horizontal localization can have a significant impact on the evolution of large-amplitude IGWs (Sutherland, 2001). Jones & Houghton (1972) argued that a horizontally localized IGW source injects momentum into the mean flow in a horizontally limited region, thereby enabling the development of horizontal pressure gradients which, in turn, oppose the formation of mean currents.

A simulation has been performed in which the wave packet is compact in both the vertical and horizontal directions. The vertical localization function and governing parameters values are the same as those employed in the horizontally periodic case of §6.3.1. The horizontal/vertical localization function is

$$F(x,z) = \exp - \left(\frac{(x - x_{cen})^2}{2\sigma_x^2} + \frac{(z - z_{cen})^2}{2\sigma_z^2} \right) \tag{6.6}$$

where, in order to avoid potential horizontal dispersion effects, σ_x is such

that the horizontal envelope (defined as the interval spanning ±10% of the maximum value of 1 in $F(x, z)$) of the forcing encompasses two horizontal wavelengths. The horizontal domain dimension and resolution are quadrupled, with respect to those listed in §6.1, to prevent spurious interactions of the wave packet with its periodic image and to maintain the same number of horizontal grid points per wave length. The wave packet is initially centered at $x = L_x/2$, where the forcing itself remains centered throughout its entire duration (one wave period).

Two-dimensional contours of the horizontal velocity field (fig. 6.6) at $t = 5\ T_w$ show a significantly weaker, horizontally inhomogeneous, negatively oriented jet-like flow behind the rear of the wave packet. It can also be seen that the IGW packet has undergone weaker structural modulation at its rear end. A vertical profile of the instantaneous horizontal velocity sampled through the center of the wave packet at $t = T_w$ and $5\ T_w$ (fig. 6.7) shows that the wave packet at $t = 5\ T_w$ has experienced only a 30% decay of its initial amplitude with pronouncedly weaker structural modulations relative to its horizontally periodic counterpart. In § 6.4.4, we further explore the underlying cause for the observed reduction in the strength of the mean flow for the horizontally localized wave packet and assess the validity of the Jones & Houghton (1972) conjecture on horizontal pressure gradients driving suppression of horizontal streaming of a horizontally localized IGW packet.

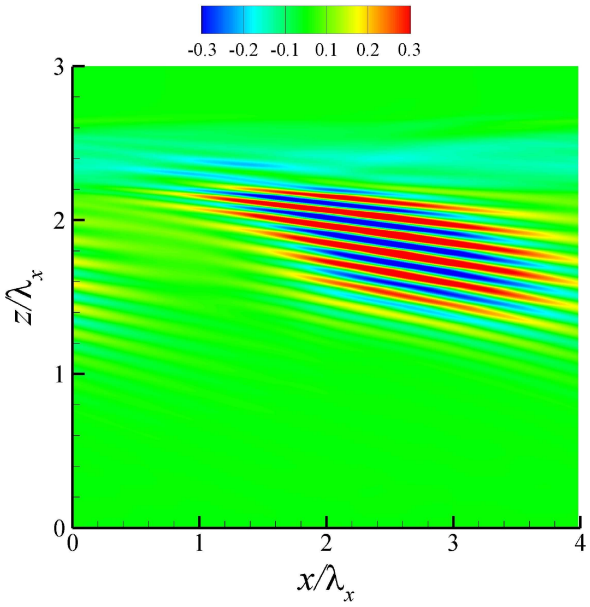

Figure 6.6: Two-dimensional contours of the horizontal velocity field at $t = 5T_w$ in a fully nonlinear simulation of a both vertically and horizontally localized wave packet,, for $Ri = 1$.

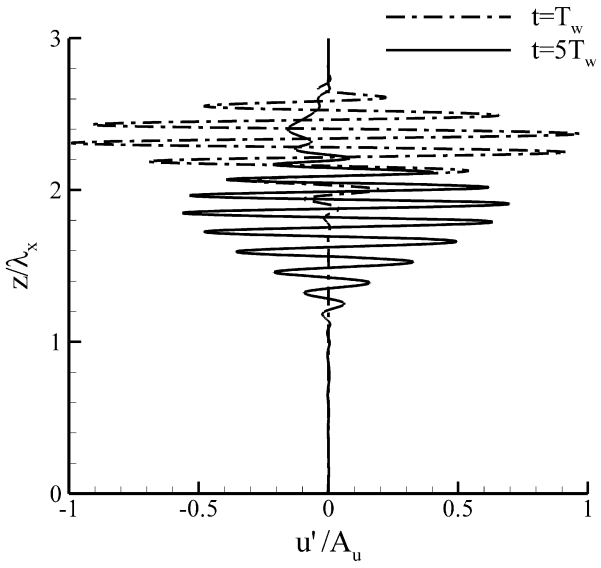

Figure 6.7: Vertical profile of the instantaneous horizontal velocity at the instantaneous wave packet center, x_c, compared at $t = T_w$ and 5 T_w in a fully nonlinear simulation of a both vertically and horizontally localized wave packet, for $Ri = 1$.

6.4 Model for wave packet deformation

6.4.1 Mean flow evolution equation and scaling

Decomposing the instantaneous velocity field $u(x, z, t)$ into the sum of a horizontal average (denoted by an overbar) $\overline{U}(z, t)$ and an associated perturbation $[u'(x, z, t), w'(x, z, t)]$ it can be shown that, for two-dimensional, non-rotating, stratified flow, which is statistically homogeneous in x (which is valid for an IGW that is infinitely periodic in the horizontal when the averaging interval is λ_x), the evolution equation for the mean horizontal velocity is given by

$$\frac{\partial \overline{U}}{\partial t} = -\frac{\partial \overline{u'w'}}{\partial z} + \nu \frac{\partial^2 \overline{U}}{\partial z}, \tag{6.7}$$

which is the same equation as that considered by Zikanov & Slinn (2001) and Scinocca & Shepherd (1992), with the latter focusing on the inviscid version.

The mean flow is, therefore, driven by the Reynolds stress gradient and viscous attenuation. For ideal, space-filling IGWs, the Reynolds stress takes on a uniform value in the region occupied by the waves and thus cannot induce a mean flow. However, strong vertical localization can introduce non-negligible vertical variations in the Reynolds stress and, as a result, a strong mean flow. Lighthill (1978) argued that, in the laboratory, the mean force resulting from viscous attenuation can be cancelled by horizontal pressure gradients that may be easily set up in a finite-size container (presumably due to free surface tilting).

By neglecting the viscous term (an assumption justified by the values of

Reynolds number considered in this study), equation (6.7) simplifies to:

$$\frac{\partial \overline{U}}{\partial t} = -\frac{\partial \overline{u'w'}}{\partial z} \quad . \tag{6.8}$$

Note that due to the periodicity of the forcing terms, they do not appear in both equations (6.7) and (6.8). Thus, these equations represent the mean flow velocity that forms not only when the forcing is active but also when a localized IGW packet freely propagates away from the source region.

An estimate of the growth in the mean horizontal velocity of a vertically localized IGW packet during one wave period $T_w = 2\pi/\omega$ may be obtained by appropriately non-dimensionalizing equation (6.8). The characteristic velocity and time scales are chosen to be $A_u = AU_o\ m/k = A_\zeta \omega\ tan(\theta)$ and $1/\omega$, respectively. The characteristic length scale is that of the Reynolds stress variation in the vertical, i.e. σ. Equation (6.8) now becomes:

$$\frac{\partial U^*}{\partial t^*} = -\frac{A_\zeta}{\lambda_x}\frac{tan(\theta)}{\gamma}\ \frac{\partial \overline{u'^* w'^*}}{\partial z^*} \ , \tag{6.9}$$

where stars represent non-dimensional quantities and $\gamma = \sigma/\lambda_x$. The growth of the mean horizontal flow over one wave period therefore scales with $A_\zeta\ tan(\theta)/(\lambda_x \gamma)$, i.e. the mean flow is enhanced with increasing wave steepness and degree of vertical localization of the packet. Furthermore, mean flow formation is enhanced for wave packets that are closer to the hydrostatic limit ($\omega/N << 1$ for $\theta \to \pi/2$), i.e. near-horizontally propagating waves.

Alternatively, one can write

$$\frac{A_\zeta}{\lambda_x}\frac{tan(\theta)}{\gamma} = A/\sqrt{Ri}\ \frac{tan(\theta)}{\gamma\ \omega/N} \ , \tag{6.10}$$

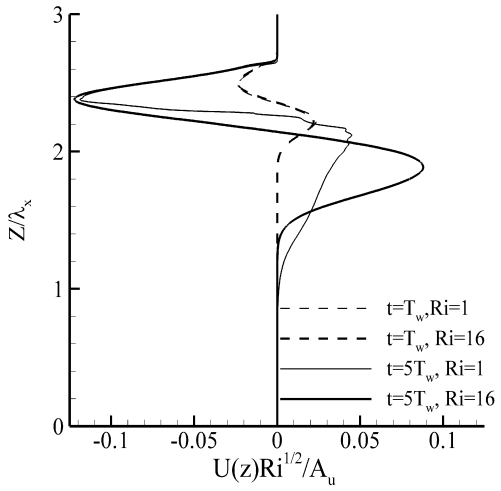

Figure 6.8: Richardson number-rescaled mean flow profiles in fully nonlinear simulations of a horizontally periodic, vertically localized wave packet at $Ri = 1$ and 16.

which quantifies the scaling of the mean flow velocity as a function of input parameters (see table 6.1). Thus, equation (6.10) indicates that for a fixed nondimensional vertical velocity amplitude A, wave number inclination angle θ and degree of vertical localization γ, wave packets operating in weaker stratifications are more susceptible to mean flow generation, as they are bound to have higher steepness (i.e. larger A_ζ/λ_x).

If one rescales the mean flow velocity profiles of the $Ri = 1$ and 16 cases with $\sqrt{Ri}$, the profiles are found to coincide at $t = T_w$, (figure 6.8). At $t = 5T_w$, the scaled profiles nearly coincide over their negative jet portion but show significant differences over the positive jet component. This deviation suggests that the proposed scaling does not accurately capture the highly nonlinear later stages of the wave-mean flow interaction (apparently intensified with the large wave steepness in the $Ri = 1$ case) in which the mean flow becomes strong enough to modify the initially prescribed wave field characteristics upon which

the current scaling is based.

6.4.2 Approximate solution at early times

At sufficiently early time, i.e. when the forcing is active ($0 < t < T_w$), the mean flow is not found to grow enough to significantly alter the structure of the wave field. The early time evolution of the wave field may therefore be accurately predicted. Specifically, it is reasonable to assume that the mature wave-packet resulting from the application of the forcing to an initially quiescent flow field, has, to leading order, velocity and density fields that are given by equations (6.1)-(6.3) with an amplitude $\tilde{A}(t)$ that grows in time and a time-dependent phase $\phi = kx + mz - \omega t$.

Furthermore, assuming negligible dispersion, the wave envelope has a structure that is considered to remain unchanged in time and translates downwards with the vertical component of the packet's group velocity, C_{gz}, as computed by linear theory. Our observations during the interval $0 < t < T_w$ confirm the above assumptions, which are invalidated as soon as significant mean flow begins to form, thus altering the structure of the instantaneous u-velocity field.

The associated Reynolds stress distribution may now be written as

$$\overline{u'w'} = U_o^2 \left(-\frac{\tilde{A}^2(t)m}{k} \Phi^2(z,t) \overline{cos^2\phi} - \frac{\tilde{A}^2(t)}{k} \Phi(z,t)\Phi'(z,t) \overline{cos\phi sin\phi} \right), \qquad (6.11)$$

where $\Phi(z,t)$ has the same structure as $F(z)$ in equation (6.4) but with z_{cen} replaced by $z_{cen} - |C_{gz}|t$ to account for the downward propagation of the wave packet. By evaluating the horizontal averages and substituting them back

into (6.8) we have:

$$\frac{\partial \overline{U}}{\partial t} = U_o^2 \tilde{A}^2(t) \frac{m}{k} \Phi(z,t) \Phi'(z,t). \tag{6.12}$$

To proceed, the amplitude function $\tilde{A}(t)$ needs to be defined. In the simulations considered here, during the time of active forcing, the amplitude of the wave field is found to increase linearly with time as $\tilde{A}(t) = At/T_w$. An estimate of the initial mean growth may then be obtained by integrating equation (6.12) from $t = 0$ to some time $t < T_w$. For the purpose of integration, the wave packet is assumed fixed in space in a quasi-static sense ; the time dependence of the argument of the Gaussian function, Φ, is not taken into account when carrying out the integration. This assumption is justifiable when the total integration time is comparable to T_w and, thus, small compared to the significantly longer wave packet's vertical propagation time-scale λ_z/C_{gz}. The early-time mean flow is thus computed as

$$\overline{U}(z,t) = U_o^2 \frac{A^2}{T_w^2} t^3 \frac{m}{3k} \Phi(z,t) \Phi'(z,t) \qquad t < T_w = \frac{2\pi}{\omega} \,. \tag{6.13}$$

The estimate for mean flow evolution predicted by equation (6.13) is compared to the mean flow obtained from the numerical solution of the fully nonlinear Navier-Stokes equations in figure 6.4 for the baseline case. The analytical estimate captures quite well the initial structure, amplitude and growth rate of the numerically generated mean flow up to $t = 3/4T_w$, when the numerical results exhibit non-negligible, but still small, deviations from the analytical solution. Beyond this time and as the mean flow continues to grow, the wave-packet undergoes significant distortions and is no longer faithfully represented by the velocity fields given by equations (6.1)-(6.2). Consequently, the mean

flow that is further generated can no longer be predicted by equation (6.13), as one must consider the changes in the wave velocity field structure. To this end, a fully nonlinear analysis is needed where the coupling between mean and wave velocity fields is bi-directional, unlike the uni-directional coupling from wave to mean flows described above.

6.4.3 Mean flow structure at later times

It is instructive to compare the mean flow observed within the mature IGW packet, namely when it has moved sufficiently far from the source, with previous theoretical predictions. Specifically, the mean flow, derived for a conservative (unforced, inviscid) flow of a freely propagating low-amplitude IGW (Scinocca & Shepherd, 1992), may be closely approximated by the second-order-accurate expression for the pseudomomentum Sutherland (2001), namely:

$$M(z) = -\overline{\omega_y A_\zeta}, \tag{6.14}$$

where $\omega_y = \partial u'/\partial z - \partial w'/\partial x$ is the vorticity and $A_\zeta = \rho'/|d\rho/dz|$ is the vertical displacement and the overbar denotes averaging over one horizontal wavelength (as in the previous two sections). Although the above expression is derived for small amplitude waves, Sutherland (1996) showed, using fully-nonlinear numerical simulations, that the above expression is still accurate within numerical truncation and round-off errors, even for wave amplitudes close to the breaking limit (Sutherland, 2006*a*).

Figures 6.9(a) and 6.9(b) compare the computed wave pseudomomentum with

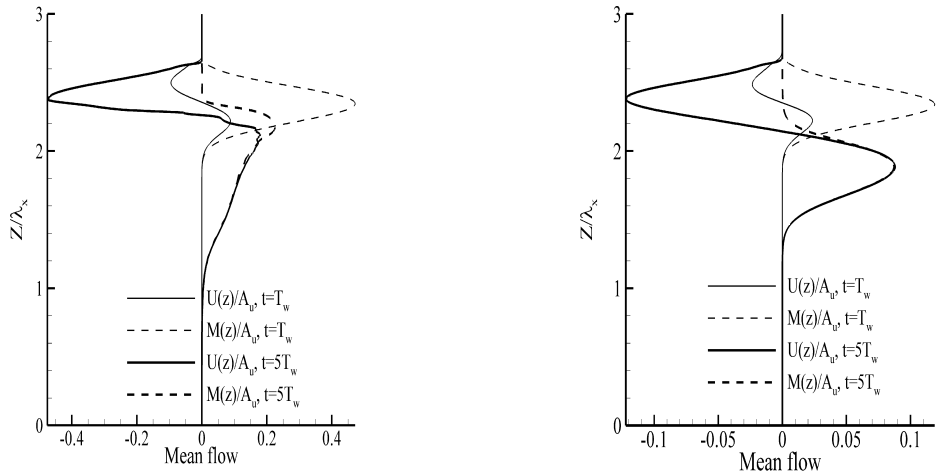

Figure 6.9: Comparison of the mean horizontal flow profile and the wave pseudomomentum , $M(z)$, in a fully nonlinear simulation of a horizontally periodic, vertically compact wave packet at $t = T_w$ and 5 T_w, for (a) $Ri = 1$ (b) $Ri = 16$.

the actual mean horizontal flow at $t = T_w$ and $5T_w$ for the $Ri = 1$ and $Ri = 16$ simulations, respectively. The initial structure of the mean flow, as discussed in §6.4.2, is composed of a positive and negative jet, whose structure is dictated by the term $\Phi(z,t)\Phi'(z,t)$ in equation (6.13). According to figure 6.9(a) and 6.9(b), the wave pseudomomentum is not characterized by any negatively oriented flow, whereas its positive component strongly overpredicts the corresponding mean flow observed inside the source region.

As the forcing is turned off and the wave packet freely moves downward, the amplitude of the negative jet continues to grow at the expense of the decaying wave packet. By $t = 5T_w$, it becomes about half the horizontal velocity magnitude, A_u, for the $Ri = 1$ case. At the same time, in the $Ri = 16$ case, the negative jet amplitude is very close the vertical velocity magnitude $A_w = AU_0 = 1/8A_u$,

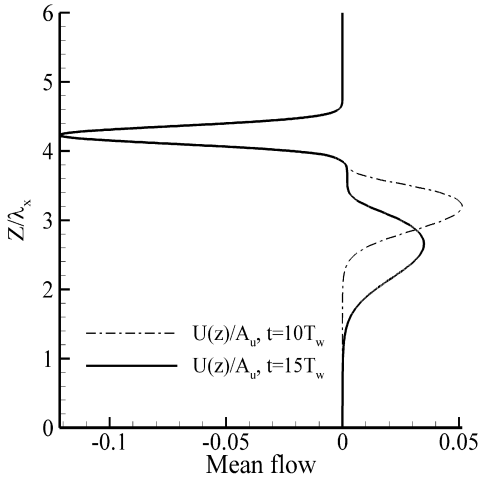

Figure 6.10: Comparison of the mean horizontal flow profiles at $t = 10T_w$ and $15T_w$, in a fully nonlinear simulation of a horizontally periodic, vertically compact wave packet in a domain with height $L_z = 6\lambda_x$, for $Ri = 16$.

which corresponds to a factor of $1/\sqrt{Ri} = 4$ reduction in the strength of the negative jet relative to the $Ri = 1$ case. Figures 6.3 and 6.5 show that during the same period, the wave packets have decayed by about 50% and 20% of their initial amplitude in the $Ri = 1, 16$ cases, respectively.

The growth of the negative jet has been further monitored in a special simulation where the height of the domain (and the vertical resolution) have been doubled. This growth is found to continue until the weakened and structurally modulated wave packet completely leaves the forcing region, leaving behind the negative jet as a steady-state residual mean flow (see fig. 6.10). At this point, the mature wave packet propagates further out into the ambient and evolves independently of the generation mechanism and any interaction with the negative jet.

Now, the positive jet created during the forcing period remains attached to the wave packet and propagates with it away from the source. Since the concept of wave pseudomomentum does not apply for forced IGW packets, it is expected that it initially overpredicts the positive component of the mean flow. However, it does predict with increasingly better accuracy the mean flow associated with the mature wave packet once the wave packet has exited into the ambient fluid and is no longer subject to the influence of the negative jet. Accordingly, we refer to the positive jet as the "wave-induced" mean flow to differentiate it from the negative jet left behind in the source region, which is regarded as a "residual" mean flow.

For the $Ri = 16$ run (figure 6.9(b)), the near-Gaussian shape of the computed wave-induced mean flow is consistent with the shape of the mean flow reported in the low-amplitude simulations of Sutherland (2001, 2006*b*). At $Ri = 1$ and $t = 5T_w$ (figure 6.9(a)), however, the wave-induced mean flow exhibits a non-symmetric profile, with a more diffuse leading edge and a peak near the rear flank of the packet, agreeing qualitatively with the general shape of the mean flow in the more hydrostatic ($m/k = 2.5$) of the large-amplitude cases examined by Sutherland (2001), which is less hydrostatic than the wave considered here. The agreement of the wave-induced mean flow and the predicted pseudomomentum is worse at $Ri = 1$, i.e. the case with larger steepness, especially near the trailing edge of the packet, than for the $Ri = 16$ case. This is, apparently, a result of the highly nonlinear wave-mean flow feedback (intensified by the larger wave steepness) which inevitably leads to stronger structural modulations of the rear flank of the wave packet in the $Ri = 1$ case.

6.4.4 Mean flow reduction due to horizontal localization

Understanding the cause underlying the observed reduction of the mean flow generated by a horizontally localized wave packet requires an appropriate definition of the horizontal averages of velocity and momentum fluxes to enable objective comparisons with the corresponding metrics for a horizontally periodic wave. To this end, the horizontal mean of a variable $a(x, z, t)$ is defined as

$$\overline{a}(z,t) = \lim_{\ell \to \infty} \frac{1}{\ell} \int_{x_0}^{x_0+\ell} a(x,z,t)\, dx\,, \tag{6.15}$$

where ℓ is the sampling interval length. For the mean to be well-defined, the limit must be independent of the initial location x_0 around which the limit is sought. While for a horizontally periodic IGW packet the averaging is clearly independent of the initial location x_0, for a horizontally localized packet the limit is a function of where the averaging interval starts (i.e. x_0). For a horizontally limited monochromatic IGW packet, it is possible to separate the wave form into an equivalent mean (as defined by equation 6.15) and a pure periodic wave-like component through phase averaging. Specifically, the phase average operator $\langle\ \rangle$ is defined as (see Reynolds & Hussain (1972); Finnigan *et al.* (1984))

$$\langle a(x,z,t)\rangle = \overline{a}(z,t) + \tilde{a}(x,z,t) = \lim_{N \to \infty} \frac{1}{N} \sum_{n=1}^{N} a(x \pm n\lambda_x, z, t). \tag{6.16}$$

The phase-averaged wave form $\langle a(x, z, t)\rangle$ is therefore the ensemble average of a sequence of all points along the x direction which have the same phase with respect to a reference wavelength (here taken as the IGW horizontal wavelength λ_x). Moreover, $\tilde{a}(x, z, t)$ is a horizontally periodic signal with

a wavelength λ_x. However, on account of the the horizontal variation of the "local" energy density per wavelength inside the horizontally localized IGW packet, the amplitude of $\langle a(x,z,t)\rangle$ is less than the maximum value of the original wave, $a(x,z,t)$. The desired horizontal mean $\overline{a}(z,t)$ can then be retrieved from the phase averaged wave form by taking its horizontal average over one wavelength λ_x, i.e.

$$\overline{a}(z,t) = \overline{\langle a(x,z,t)\rangle}, \tag{6.17}$$

since the average of $\tilde{a}(x,z,t)$ vanishes. The quantity $\overline{\langle a(x,z,t)\rangle}$ may then be directly compared to its counterpart for a horizontally periodic wave. Note that, computationally, the sum over N in equation (6.16) is limited to the effective width of the wave packet (defined as the interval spanning ±10% the maximum value of $u(x,t)$ at the particular z-location) to avoid artificial damping of the mean field $\overline{\langle a(x,z,t)\rangle}$.

Now, consider the conservative form of the inviscid horizontal momentum equation for the wave field namely

$$\frac{\partial u'}{\partial t} = -\frac{\partial u'u'}{\partial x} - \frac{\partial u'w'}{\partial z} - \frac{\partial p'}{\partial x}. \tag{6.18}$$

Taking the phase average of both sides of equation (6.18) followed by the horizontal average, we obtain

$$\frac{\partial \overline{U}}{\partial t} = \underbrace{-\overline{\langle \frac{\partial u'u'}{\partial x}\rangle}}_{I} \underbrace{-\overline{\langle \frac{\partial u'w'}{\partial z}\rangle}}_{II} \underbrace{-\overline{\langle \frac{\partial p'}{\partial x}\rangle}}_{III}, \tag{6.19}$$

where $\overline{U}(z,t)$ is the mean horizontal velocity. By numerically evaluating each of

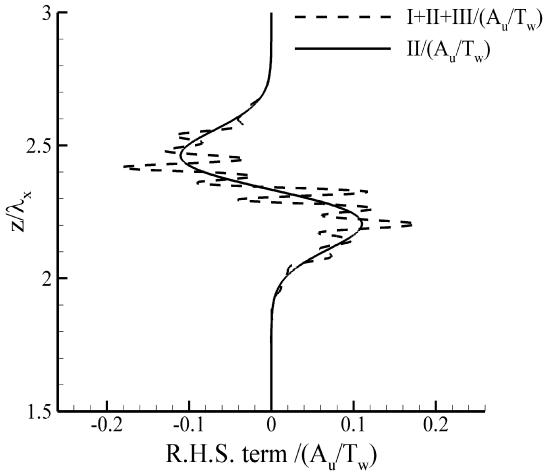

Figure 6.11: Vertical profiles of the sum of all the r.h.s. terms of equation (18) $(I + II + III)/(A_u/T_w)$ and the second term $II/(A_u/T_w)$, in a fully nonlinear simulation of a horizontally as well as vertically localized wave packet at $t = T_w$, for $Ri = 1$.

the three terms on the right hand side of (6.19), one can identify the dominant term which drives the observed mean flow formation. Figure 6.11 compares the vertical profiles of the sum of the r.h.s. terms of equation (6.19), $I + II + III$, normalized by(A_u/T_w) to the vertical profile of the second term $II/(A_u/T_w)$. We have found (not shown) that both the pressure gradient term III and the horizontal gradient of the wave Reynolds stress term I strongly oscillate in the vertical with a phase shift such that their individual profiles tend to cancel each other out. It can be seen from figure 6.11 that indeed the r.h.s. of Equation (6.19) is dominated by the vertical gradient of the wave Reynolds stress. The sum of all three terms fluctuates around $II/(A_u/T_w)$ with a standard deviation of about 14%. The dominance of the second term in equation (6.19) is found to persist over the course of the entire simulation.

The magnitude of the vertical gradient (not shown) of the wave Reynolds stress at $t = T_w$ for the horizontally localized wave is found to be approximately

half of the corresponding value for the horizontally periodic wave. This reduction in the strength of the Reynolds stress gradient is nearly commensurate with the observed reduction of the strength of the mean flow of the horizontally localized packet (computed by phase averaging followed by horizontal averaging of the horizontal velocity field) with respect to the mean flow of the horizontally periodic packet (figure 6.12)

The mean flow reduction in a horizontally localized IGW packet, as compared to its horizontally periodic counterpart, is thus primarily driven by the reduced magnitude of the vertical gradient of the wave Reynolds stress which stems from the reduced wave energy density per horizontal wavelength. Both the horizontal gradient of the Reynolds stress and the horizontal pressure gradient play a secondary role in the evolution of the horizontal mean flow. Accordingly Jones & Houghton (1972) claim about the possible role of horizontal pressure gradients in reducing the mean horizontal flow seems to be non-applicable.

6.4.5 Residual mean flow containment techniques

Two different strategies are considered towards containing the residual mean horizontal flow in the forcing region to prevent any disruptive interactions with the propagating wave packet. To this end, i.e. to enable the formation of a robust mature wave packet but also to prevent the spurious suppression of energy transfer to a pre-existing mean flow (a background current in mid-water/air or along a boundary), the particular technique under consideration must be switched-off at an appropriate time or be restricted to the wave generation region which, by design, should be sufficiently removed from the inter-

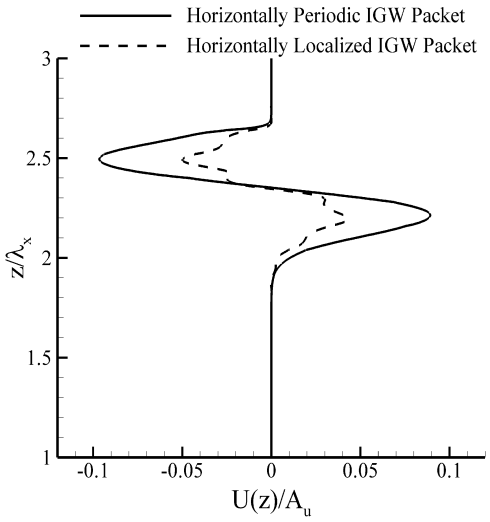

Figure 6.12: Comparison of the numerical computed horizontal mean flow for a horizontally periodic and a horizontally localized IGW packet at $t = T_w$, for $Ri = 1$.

action region.

The first mean flow containment technique relies on assuming a horizontally periodic wave field. It involves the explicit removal of the mean horizontal flow component from the corresponding instantaneous velocity component after each time step. The approach is similar to that of Zikanov & Slinn (2001), who, however, remove the plane average of the along-slope velocity component, as this direction is periodic, statistically homogeneous and normal to the gravity vector (they note that any mean flow component in the up/down slope will be opposed by gravity and should be minimum). In the first phase of their simulation, they activate the mean flow removal technique throughout the computational domain. However, to avoid artificial suppression of the along-slope current in the second phase of their simulation, where the waves approach the sloping boundary and reflect off of it, the mean current removal is restricted to the upper 60% of the computational domain.

For the problem geometry considered here, i.e. a two-dimensional rectangular domain where the x-direction is normal to the gravity vector, the mean flow can be removed by setting the zero Fourier mode of the horizontal velocity field to zero. The zero Fourier mode deactivation region is delineated by a slowly varying window with a broad Gaussian envelope which smoothly couples the forcing region with the exterior fluid. This technique may be readily implemented in codes using Fourier discretization in the horizontal and is easily adaptable to algorithms using other discretizations (e.g. finite volume or finite difference) in horizontally periodic domains. In the latter case, one can directly calculate the mean flow through equation (6.5) and subtract it off the horizontal velocity field after each time step.

Motivated by equation (6.12), another technique for mean flow removal is now proposed. The technique involves the incorporation of a sink term in the r.h.s. of the horizontal momentum equation. The term is equal and opposite in magnitude to the rate of change of the mean horizontal flow. For the horizontally periodic wave packet, the form of this absorbing term is simply the negative of the r.h.s. of equation (6.12):

$$F_t = -U_o^2 \tilde{A}^2 \frac{m}{k} \Phi(z)\Phi'(z) \ . \tag{6.20}$$

The $U_o^2 \tilde{A}^2 \frac{m}{k}$ factor in the above forcing term is approximated by the product of the absolute value of the instantaneous horizontal and vertical velocities at the center of the wave packet after each time step. The vertical coordinate of the instantaneous wave packet center is calculated as the location in the vertical profile of the wave packet's horizontal velocity (sampled at $x = L_x/2$) where an absolute maximum is attained. This location serves as the instantaneous origin for the functions $\Phi(z)$ and $\Phi'(z)$.

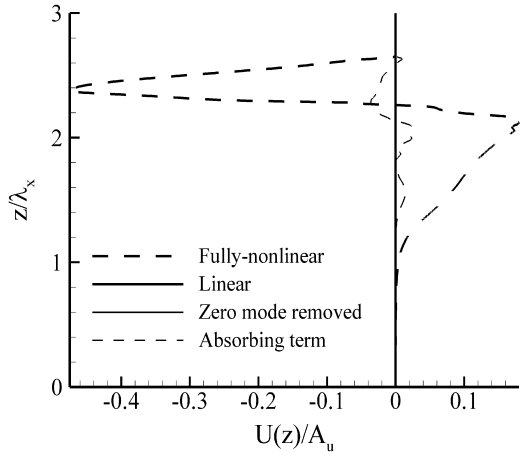

Figure 6.13: Comparison of the mean horizontal flow in a fully nonlinear simulation and linear simulations, along with simulations in which either the zero Fourier mode is removed or the proposed mean flow absorbing term is used, for a horizontally periodic vertically localized wave packet at $t = 5T_w$, with $Ri = 1$ (note that the mean flow is zero everwhere in both the linear simulation and that with the zero Fourier mode removed).

Two separate simulations have been run where each of the mean flow containment techniques is implemented throughout the full duration of the simulation for an IGW packet in the absence of any background flow. An additional run has been performed where the nonlinear terms are "turned off" but the zero-Fourier mode is left untouched for the entire run. The results from all three cases are compared in figure 6.13. The mean flow is identically zero when either the nonlinear terms or the zero Fourier mode are absent. Thus, as indicated by equation (6.7), the observed wave-induced mean flow is driven by nonlinear effects with no energy deposited in higher horizontal harmonics. When a sink term is used, a very weak mean flow develops over the course of the simulation. When examining the wave packet's instantaneous structure in figure 6.14, it can be seen that, apart from dispersion effects typical of large

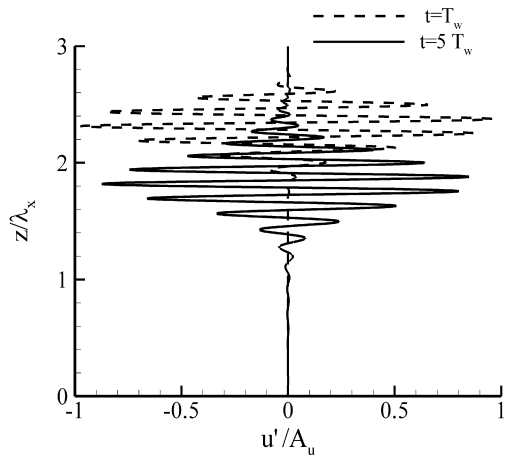

Figure 6.14: Vertical profile of the instantaneous horizontal velocity at $x = L_x/2$, compared at $t = T_w$ and 5 T_w in a fully nonlinear simulation of a horizontally periodic vertically localized wave packet in which the mean flow absorbing term is used, for $Ri = 1$.

amplitude IGWs, the wave packet has preserved its initial spatial structure and decayed by less than 5% of its initial amplitude.

6.4.6 Critical level interaction

The viability of the mean flow containment techniques, particularly the zero Fourier mode removal, is further tested in the framework of the critical layer interaction of a large amplitude, horizontally periodic, vertically compact IGW packet with a Gaussian background shear flow. The simulation parameters are chosen to match the baseline case described in table 6.1. The background current is configured to be the same (summarized in table 6.2) with that used in

Table 6.2: Values for additional parameters relevant to critical level simulation: Unless otherwise listed, all other parameters have the same value as in the baseline case described in table 6.1.

Parameter	Value
L_z/λ_x	1.8
σ_{shear}	$L\sqrt{(0.08)^2/-2\ \ln(1/2)}$
$(z_{cen}/L_x)_{forcing}$	1.2
$(z_{cen}/L_x)_{shear}$	0.325
U_s	$1.5\ \omega/\kappa$

the simulation of Winters & D'Asaro (1989). Its profile has the same shape as in equation (6.4) but with a with a magnitude (U_s in table 6.2) such that a critical level is initially established at $z/L \approx 0.39$.

Winters & D'Asaro (1989) found that, because of the associated mean flow acceleration, the vertical location of the critical level is displaced upward towards the wave source. Therefore, adequate resolution within the vicinity of the initial location of the critical level is imperative and is enabled through the multidomain scheme. A little over two subdomains are assigned to the dominant nonlinear critical layer thickness. The onset of instability at the critical level generates higher horizontal wave numbers than those supported by the initial horizontal resolution of $N_x = 128$ grid points. Thus, to avoid aliasing effects, a regridding procedure is applied wherein the horizontal resolution is changed to $N_x = 256$ as the wave reaches the interaction region, and a final regridding to $N_x = 512$ is implemented few buoyancy periods before the instability onset. The wave packet reaches the interaction region by $Nt \approx 35$ where it is trapped near the critical level. The diminishing vertical wavelength leads to intensifica-

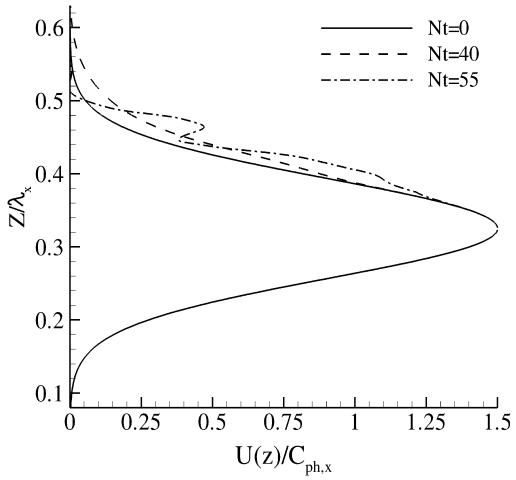

Figure 6.15: Mean flow evolution during the wave-shear flow interaction for the critical level simulation

tion of the wave shear. The resulting discontinuity in the wave Reynolds stress leads to exchange of momentum with the background shear flow resulting in its acceleration as seen in figure 6.15.

The development of the instability is best illustrated by considering the evolution of the vorticity field in the highly resolved interaction region. As the wave packet approaches the critical level, the constant phase bands of its vorticity field (figure 6.16(a)) tilt closer to the horizontal direction in the decelerating front of the packet than in its rear, as it is in the former region where the vertical wavelength decreases and the energy density increases. Beyond this point, the vorticity near the critical level starts to intensify in response to the increase in the wave shear. By $Nt \approx 52$, localized instabilities are visible close to the critical level (figure 6.16(a)) which then give way to the rapid emergence of distinct Kelvin-Helmholtz billows along the entire critical layer region (figure 6.16(b)) confirming that in a two-dimensional framework, as noted by Winters & D'Asaro (1989) and Lin *et al.* (1993), this instability is shear-driven.

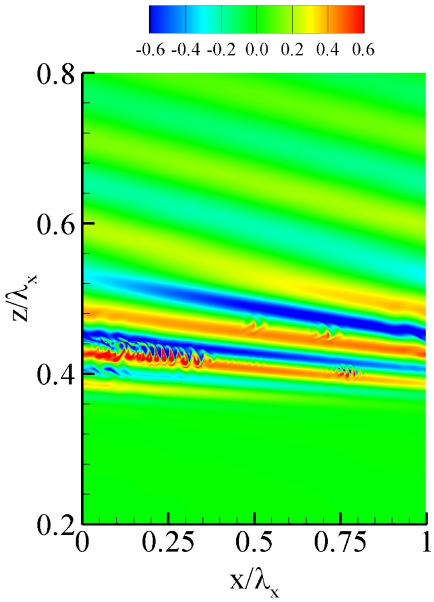

(a)

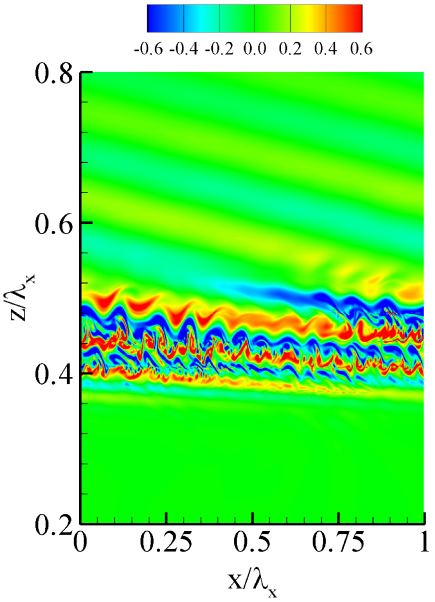

(b)

Figure 6.16: Two dimensional contours of the vorticity field for the critical level simulation (a) $Nt = 52$ (b) $Nt = 55$. The min/max range for the colorbar for the two snapshots is symmetric about $\omega_y = 0$ to $\pm(|\omega_y^{max}| + |\omega_y^{min}|)/2$ at $Nt = 50$ (i.e. close to the onset of the shear instability).

6.5 Discussion

6.5.1 Mature wave-packet: generation via mechanical forcing vs. impulsive introduction

The focus of the present study is on the numerical generation of IGW's through the incorporation of explicit forcing terms into the governing equations. Forcing terms serve as a more generalizable approach which is amenable to the generation of either wave packets or continuous wave trains. However, the results of this work are also applicable to simulations of IGW's with equivalent initial conditions. In this case, when a mature wave packet is directly introduced, with the initial wave velocity and field prescribed by equations (6.1)-(6.3), there is no mean flow present at time $t = 0$ by virtue of horizontal periodicity. Following the analysis of §6.4.2, the initially developing mean flow will establish the same spatial structure with the forced system. The early-time growth rate of the mean flow is linear and with a constant growth coefficient $\tilde{A}(t) = A$. In contrast, in the forced system, the mature wave packet, which requires one wave period to form, is already accompanied by a weak mean flow (see figure 6.8) that has developed with a cubic growth rate as indicated by equation (6.13). For both cases, the later stages of the wave mean-flow interactions are expected to be similar to what is described in §6.4.3. As the core of the interaction occurs once the forcing has been switched off after one wave period, the weak mean flow established after one wave period in the forced approach is not likely to significantly alter the wave residual mean flow interaction.

However, the presence of forcing may enhance the accumulation of energy in

the forcing region in the form of a non-propagating component of the solution, as compared to an equivalent simulation with initial conditions, through other mechanisms than those described above. Specifically, it can further be argued that, because the forcing is abruptly turned on and off, additional (typically higher) frequencies are introduced beyond the primary frequency. Also as the the vertical Gaussian envelope of the forcing narrows in the physical space, its spectral support increases, resulting in the introduction of additional vertical length scales beyond the primary vertical wavelength of the wave packet. For a specified horizontal wavelength, these additional vertical length scales may not match either the forcing frequency or the additional frequencies introduced by the transient nature of the forcing and the associated energy may remain trapped in the source region. Note, however, that several test simulations were run in which the forcing terms were gradually ramped up and down over an interval $[0, 2T_w]$. On one hand, little reduction in the strength of the residual mean flow component was observed. On the other, the resulting wave packet developed an envelope that was broader than desired, leading to enhanced dispersion.

6.5.2 Generation of an internal wave train

Issues with mean flow formation are also relevant in the framework of the continuous generation of IGWs, as already reported by Zikanov & Slinn (2001). What they describe as a "transient mean flow associated with the propagating front of the wave" is near-equivalent to the mean flow induced by the mature wave packet. The mean flow generated in their forcing region, however, is the equivalent of the negative jet discussed in §6.4.2 and §6.4.3 . In terms of the problem geometry they consider, the establishment of a statisti-

cally steady state of wave reflection (and possible breakdown into turbulence) near the bottom boundary requires persistent injection of energy into the vertically limited forcing region to generate a wave train. Over longer times, on account of the vertical gradient of the Reynolds stress that is established in the forcing region (see also equation (6.9)), a non-negligible residual mean flow will inevitably develop therein which will significantly alter the propagating wave packet through the mechanism described in §6.4.2 and §6.4.3. Despite differences in the nature of the wave forcing (body force terms in the governing equations vs. physical wave generator ; see the next section), such a mechanism may not only be operative in numerical simulations but also in equivalent laboratory experiments, as the formation of disruptive horizontal currents that significantly contaminate the source region have been reported to us (T. Peacock, personal communication).

6.5.3 Additional connections with the laboratory and nature

In a computational setting, the use of a body force term in the governing equations allows for the fluid within the source region to move freely. In contrast, in the laboratory, the internal wave generator is a mechanical device within which no fluid motion is possible (Gostiaux, Didelle, Mercier & Dauxois, 2007). Furthermore, lab-space limitations require that such a device be inevitably localized in the horizontal, which is expected to significantly reduce the mean flow, as suggested by §3.2. In addition, any externally imposed incidental horizontal pressure gradients may also act to oppose horizontal streaming, as proposed by Lighthill (1978). Most importantly though, confinement effects of the tank/container walls in a small-scale facility can strongly impede the formation and sustenance of a horizontal mean flow. Now, for the particular case when

IGWs are excited by the oscillation of a vertical cylinder in a stratified fluid, waves are observed to propagate in a Saint Andrew's cross pattern (Mowbray & Rarity, 1967). The inherent symmetry of this particular set-up suggests that the residual mean flows induced by the generation of the oppositely moving waves can potentially cancel one another. Note that symmetry may also act to reduce the impact of the residual mean flow in equivalent numerical simulations, such as the one reported in Javam & Redekopp (1998).

In the ocean and atmosphere, IGWs are usually generated by a source of finite scale and, as a result, have dimensions that are comparable to those of the source, as suggested in Appleby & Crighton (1987); Hurley & Keady (1997). Furthermore, in such settings, horizontal and vertical confinement are typically not an issue. Thus, under sufficiently strong and vertically localized periodic forcing, strong residual horizontal currents could be produced for either IGW packets or wave trains at the respective generation site. A favorable situation where this may happen is a sufficiently nonlinear internal tide operating over a particular geometry of bottom topography in the deeper ocean (see Peacock, Echeverri & Balmforth, 2008).

CHAPTER 7

CONCLUSIONS AND FUTURE WORK

7.1 Concluding remarks

7.1.1 Wake-generated internal gravity waves

The first half of the thesis has investigated the generation of internal gravity waves by the turbulent wake of a towed sphere in a linearly stratified fluid. For this specific flow, we have conducted the first (to the best of our knowledge) quantification of the wave field properties, in the near field of the wake, using LES of the fully nonlinear governing equations over a broad range of Re and Fr.

We have used continuous wavelet transforms to quantify the horizontal wavelengths of the energetically dominant internal waves on prescribed horizontal planes close to, but outside, the turbulent wake edge. The wavelet transform has estimated the horizontal wavelength of the wave field and allowed us to understand and assess its spatial variability over the entire horizontal plane under consideration. The estimated wavelengths obtained from two independent wavelet analyses based on the cylindrical Arc wavelet and the directionally biased *Morlet2D* wavelets are in close agreement. On one hand, this agreement indicates that the calculated wavelengths are accurate and reliable estimates of the internal wave field wavelengths. On the other hand, it implies that the observed orientations of the quasi-random wave field, on a particular horizontal plane, are highly concentrated around a mean direction that is independent of either Re or Fr.

The estimated horizontal wavelengths, and their subsequent decay rates, are found to be dependent on both Re and Fr, with an empirical $Fr^{1/4}$ scaling and decay rates significantly slower than the $1/Nt$ characteristic of internal waves emitted by an impulsive point mass source. For the first time, the dependence of the horizontal wavelength on both Re and Fr has been reported.

The frequencies of the IGWs are obtained from one-dimensional wavelet transforms of multiple time series at several streamwise and spanwise locations on the horizontal planes. The linear dispersion relation was used to obtain the angle of the phase line tilt to the vertical and the vertical wavelength. In agreement with the properties of turbulence-generated IGWs reported in previous studies, the angle values are found to lie in a rather narrow range $\theta \in [27 - 50°]$, however, this study additionally establishes the connection of the underlying selection mechanisms to Re. The results suggest that at low Re, the coupling of the waves to the turbulent wake region is not strong and that the selection is merely based on the capabilities of the waves to propagate away from the turbulent region while experiencing the minimum viscous decay as they move at the maximum possible vertical group velocity. At high Re, however, the prevalent angles indicate that the waves are likely to be strongly coupled to the turbulent region dynamics as they most efficiently extract horizontal momentum from the wake region.

The vertical group velocity of the internal wave field is empirically found to scale as $Fr^{-3/4}$ scaling, independent of Re. Accordingly, under navally relevant conditions ($Fr = O(200)$), the wake-emitted waves are expected to move vertically towards the ocean surface at even slower rates. Even though wake-

radiated internal waves reach the surface at the same rate, independent of *Re*, internal waves radiated by a high *Re* wake are found in locations that are further offset from the wake axis in the spanwise direction. This can be explained on the basis of persistence of wave emission by the turbulent wake for much longer time and the continued increase in the horizontal width of the wake at high *Re*.

The estimated isopycnal displacement amplitude and the steepness of the waves increase with both *Re* and Fr, indicating that the waves become more nonlinear and thus more vulnerable to instabilities and breaking as both parameters increase. The increase of the displacement amplitude in weak stratification (high Fr) is in agreement with previous measurements, however the proposed increase with *Re* has not yet been verified experimentally. Extrapolating this result to navally relevant parameter values implies that the waves under these conditions are even more likely to break remotely into small scale turbulence and potentially expose the turbulence generating source. From an oceanographic and geophysical standpoint, the wave breaking and the ensuing turbulence act as a localized source of mixing in the water column. From energetics point of view, the increase in the displacement amplitude with *Re* indicates that there is more energy available for the wave field at high *Re*.

Explicating and resolving the dependence of the horizontal wave length and the displacement field on either *Re* or Fr requires understanding of the underlying generation mechanisms of the internal wave field. Questions are still open on the connection between the observed wave properties and the dynamics of the turbulent wakes. For example; how are the observed length scales relate to the turbulence length scales such as the pancake eddy scales or the spacing

between them and how are the frequencies of the waves relate to the frequency spectrum of the turbulence? Answers to these questions can possibly help theoreticians formulate new wave generation theories. Finally, the energetics of the wave emission by the turbulent wake such the wave momentum and energy flux can help in understanding the possible impact of the wave emission process on the dynamics of the turbulent wake and explain the coupling between the waves and their turbulent source region. Oceanographers are particularly interested in knowing answers to these questions as there are almost no available measurements of wave energy fluxes radiated from the wakes of submerged topography (seamount) or a headland/island in a strongly stratified water.

This study has established a comprehensive parametrization of the internal wave field emitted by a stratified turbulent wake of a towed sphere. It is hoped that such parametrization will guide new theoretical studies of wave generation mechanisms and will also help researchers improve the current sub-grid scale models and understand the impact of small scale processes on large scale atmospheric and oceanic flow problems.

7.1.2 Numerically forced internal gravity waves

In the second half of the thesis, the formation of strong mean horizontal flows in the wave generation region has been examined in two-dimensional numerical simulations of internal gravity wave (IGW) packets where the waves are generated by incorporating mechanical forcing terms into the incompressible Navier-Stokes equations. The observed mean flows are, in part, a direct result of modeling the vertically localized forcing based on a solution to the linearized

inviscid internal wave equations, yet introducing it at large amplitude into the fully nonlinear governing equations. As a result, a vertically localized gradient in the Reynolds stress field emerges within the source region giving rise to an opposing horizontal current which distorts the prescribed structure of the IGW packet and depletes it of its energy as the wave packet moves into the ambient fluid.

At early times, a simple mathematical model, based on a uni-directional coupling from the wave to the mean flow, accurately predicts the time structure of the horizontal mean flow, which consists of two counter-flowing jets. The jet oriented against the horizontal group velocity of the wave packet remains trapped within the forcing region as a residual mean flow. The jet component aligned with the horizontal wave group velocity remains attached to the IGW as the wave propagates away from the forcing region. Sufficiently far from the source, the structure of the latter component of the mean flow is predicted reasonably well by the correlation of vertical displacement and vorticity fields.

Scaling arguments indicate that the mean flow is enhanced with a stronger degree of localization of the forcing, higher degree of hydrostaticity and increasing wave packet steepness. Equivalently, it is enhanced with weaker stratification and higher IGW amplitude and degree of hydrostaticity. Horizontal localization is found to appreciably reduce the strength of the mean flow as a result of the reduced vertical gradient of the wave Reynolds stress field on account of the reduced wave energy density per wavelength.

In the particular flow solver under consideration, the mean flow may be eliminated by setting to zero the horizontal zero Fourier mode. A more generaliz-

able approach consists of incorporating appropriately designed sink terms into the solver which also account for the propagation of the wave packet. With either of the above techniques, care must be taken that they are appropriately de-activated to avoid the spurious suppression of any physically-driven mean flow formation as in the enhancement of flow along a sloping boundary or the transfer of momentum to a background current in mid-water or air.

The findings of this study are of particular value towards designing robust computational process studies of the above mentioned types of remote interaction of an IGW packet (or a continuously forced wavetrain) where the wave amplitude range is required to be as broad as possible. Insight into the underlying physics of near-source horizontal currents in laboratory experiments of persistently forced IGW beams may also be obtained. Furthermore, we conjecture that similar horizontal currents may form in the flow of the oceanic internal tide over bottom topography in the strongly nonlinear regime.

An idealized numerical process study of the amplitude sensitivity of a remote interaction of a highly vertically localized and well-defined, in terms of envelope and primary frequency and wavelength, IGW packet, in which any distortions to wave structure and amplitude are contained through the approaches outlined in §6.4.5, is undoubtedly highly instructive. However, strong vertical localization is imposed by practical limitations in computational resources and not necessarily geophysical considerations. A process-focused simulation of a wave packet that is broader in the vertical can be prohibitively costly, especially when three-dimensional dynamics within the interaction region are of interest.

The concept of a "self-destructing" IGW was originally considered by Jones &

Houghton (1972). Specifically, an initially weak amplitude IGW packet, which has propagated upward, over sufficiently large distances, through a compressible atmosphere and a background density gradient decreasing with altitude, can experience significant amplification. This amplification may be of such an extent that the weak precursors of the wave at its leading edge are able to significantly modify the background flow state by creating a strong local mean flow in an otherwise quiescent atmosphere. As the bulk of the wave packet reaches the altitude where the mean flow has previously been created, a critical level forms and the wave breaks down and dissipates. While this common situation leads to strong modification of the wave structure and possible breakdown into turbulence, it happens far from the wave generation site (where the waves are presumably weak in amplitude during the wave generation) as large propagation distances are needed for significant wave growth.

This study is focused on the near source non-linearities of an IGW packet (in an incompressible flow) which can lead to intense structural changes within the generated wave field. A relevant though different inquiry may thus be posed: in nature, is it physically possible for a large amplitude strongly vertically localized IGW packet to form and, moreover, propagate over even a short distance away from its source (in what might effectively be a uniform stratification) while preserving a well-defined envelope and well-defined primary frequency and wavelength ? Consequently, in a computational process study how legitimate is it (in the context of the actual oceanic and atmospheric physics) to suppress any mean flow that develops within an IGW packet before any remote interactions occur ? Both of these questions may ultimately have to be taken into account in the formulation of ray theory-based models (Broutman, Rottman & Eckert, 2004) if and when large-amplitude IGW packets are considered.

7.2 Future work

The research considered here essentially focuses on the aspects of the near source region of IGWs whether the waves are naturally excited by the turbulence or through external forcing. A natural extension to the current research work is to focus on the waves as they move away from the source region and interact with typical atmospheric/oceanic environments.

An extension to the wake-generated IGW analysis provided in this thesis is to consider horizontal planes far from the wake center line and to quantify any changes in the wave properties as they move away from their source. This suggested study will shed some light on the importance of non-linear interactions between the waves and also the impact of viscous decay over significant propagation distances. Computational resource limitations will be a deciding factor in how much distance, far away from the source, one might be able to simulate. In this regard, discretizations of the governing equations based on non-uniform grids (such as the current multi-domain scheme) will be convenient as they naturally allow maximum flexibility in deploying the available resolution where it is most needed.

The research subject of this thesis is, for the most part, mainly concerned with the propagation of internal waves in simplified environments where the background stratification is uniform and there is no background shear flow. In a typical geophysical setting, IGWs are more likely to encounter significant local variations in the stratification profile such as in the ocean pycnocline where the buoyancy frequency of the medium increases abruptly over a relatively short vertical distance or in the surface/bottom mixed layer. Variations of the strat-

ification profile of the medium lead to complex phenomena including wave transmission, reflection, absorption, ducting and tunnelling.

We are currently collaborating with Drs. Scott Wunsch and Alan Brandt at Johns Hopkins University who are currently conducting experiments on the interaction of a forced internal wave beam with a pycnocline both in the presence and absence of a background current. We are aiding and guiding their experimental efforts as they are complicated by a variety of factors (tank size limitations, boundary reflection, image distortions for large amplitude waves and inevitable experimental noise-related errors) that can be eliminated or at least minimized in a controlled numerical simulation. A first set of simulations, for the interaction of a beam with a pycnocline with a fixed thickness but with varying maximum strength of the pycnocline stratification profile, were run by Michael Richter; a senior undergraduate researcher who was trained and guided by the author of this thesis and his thesis advisor. Reflection and transmission coefficients (fractions of incident energy that are transported into and reflected from the transition region, respectively) were calculated and compared to their experiments. The initial results helped our collaborators confirm that the measured reflection coefficients for large jumps in the stratification profile were mainly an experimental noise. Future simulations will offer significant insight and answers to many questions such as:

- The impact of the maximum stratification strength inside the pynocline on the reflection and transmission coefficients.
- The importance of the pycnocline thickness of for a given maximum stratification strength.
- The effect of the incidence angle as a representation for IGW excitation at

the driving/source frequency and its subharmonics.

- The significance of incident wave steepness on the observed wave dynamics.
- The evolution of the wave phase velocity inside the pycnocline. The answer for this question will help in the interpretation of future experiments where shear layers will be collocated with the stratification profile inside the pycnolcine as it sets the location of the critical level.

Finally, future efforts will also focus on the remote signature of the wake-radiated waves by examining their interactions with the subsurface region.The research is motivated by the need to understand and quantify remote detection of submerged turbulence and internal waves in the ocean by optical and radar images. In this regard, hypotheses and predictions based on fossil turbulence theories (Gibson, 1982; Dillon, 1984; Gibson, 1986; Keeler, Bondur & Gibson, 2005) can be tested against fully nonlinear LES and possibly improved on.

APPENDIX A

TESTING THE CONTINUOUS WAVELET TRANSFORM CODE

The ability of the CWT to identify the frequency components of a 1D temporal signal can be demonstrated through the so-called "chirp" signal in which the frequency increases continuously over time. Figures A.1(a), and (b) shows the signal in the time and wavelet space, respectively. The chirp segment occupies the middle third of the signal ($n/3 < t < 2n/3$). The transform plot, from left to right, shows peaks at decreasing scale. Note the decrease in the transform amplitude with increasing scale that reflects the continual decrease in the resolution of the CWT at progressively larger scales (i.e. as the scales approach the window/signal size) in a finite-sized signal.

The ability of the CWT to recognize intermittent features of a signal is seen in Fig. A.2(a) where two localized wavepackets appear at different times within the signal. The transform plot, Fig. A.2(b) shows two circular like regions representing the frequency content of the wave packets. The center of the band of influence occurs at the dominant frequency associated with the wave packet at the same time in which the wavepacket attains its maximum amplitude in Fig. A.2(a). Figure A.3 further demonstrates the reduced degree of resolution of a low frequency wave packet compared to a high frequency one.

Now, the 2D Arc wavelet is used to detect the scales comprising a 2D spatial signal. The result of the transform in this case is a 3D cube of data representing the local values of the modulus of the transform across all scales at all points on the *xy* plane. As an example, Fig. A.4(a) shows a 2D signal composed of one wave number oriented at 45° to the *x* axis. For such a simple signal it suf-

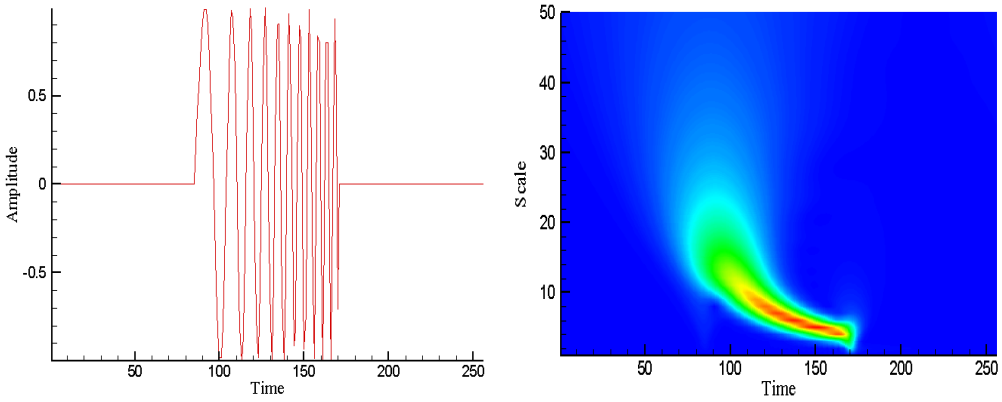

(a) (b)

Figure A.1: A chirp signal: (a) time domain (b) wavelet domain

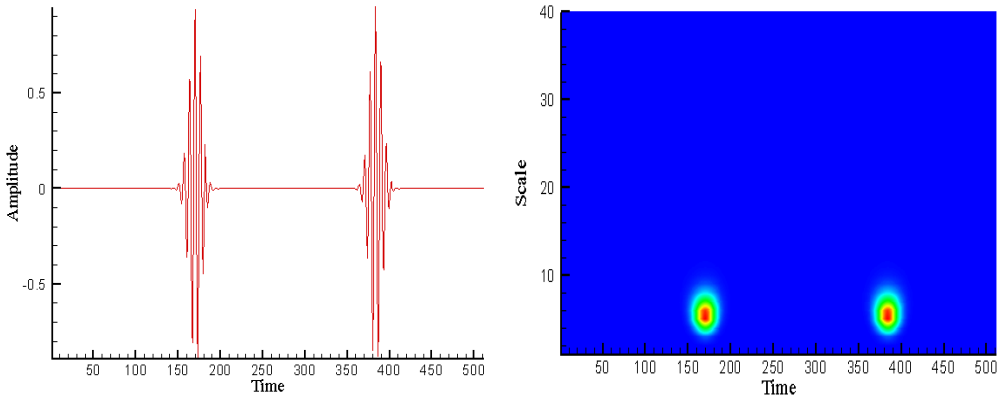

(a) (b)

Figure A.2: Same frequency at two different times: (a) time domain (b) wavelet domain

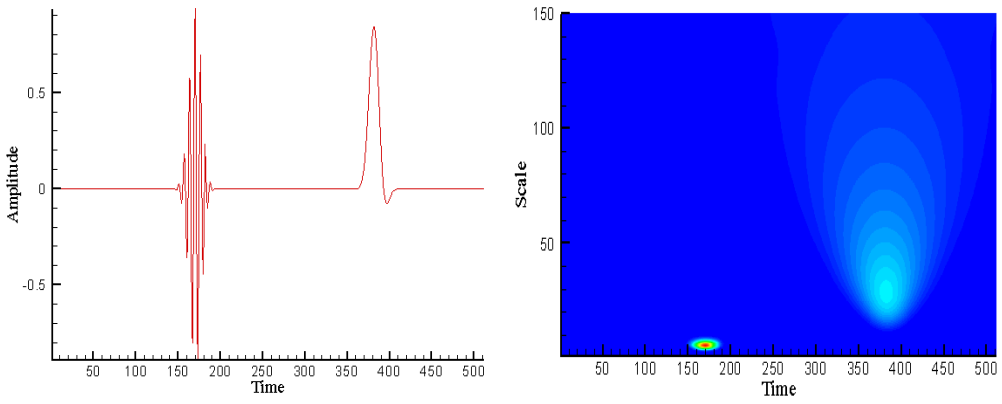

(a) (b)

Figure A.3: Two different frequencies at two different times: (a) time domain (b) wavelet domain

fices to look at the variation of the plane averaged values of the modulus of the transform with scale as a measure of scale-based resonance. The idea of plane averaging seems to contradict the purpose of the wavelet analysis which is revealing spatial distribution of the scales of resonance. However, once again, this simple choice of interpreting the modulus of the CWT is acceptable for this highly idealized signal. Figure A.4(b) shows that the peak of the modulus of the transform occurs at the expected scale. The convenience of having a non-directional wavelet transform can be illustrated by the CARRÉ signal defined in Dallard & Spedding (1993) and reproduced in Fig. A.5. The signal is distributed over the four quadrants of the *xy* plane with two different wave numbers and three orientations. We arbitrarily define the normalized length of the signal in both directions as 256 and scales corresponding to the two wave numbers as 5 and 10. In this example, it is clear that averaging the modulus at a given scale is completely futile, as it will not differentiate between wave numbers corresponding to the same scale but different orientations.

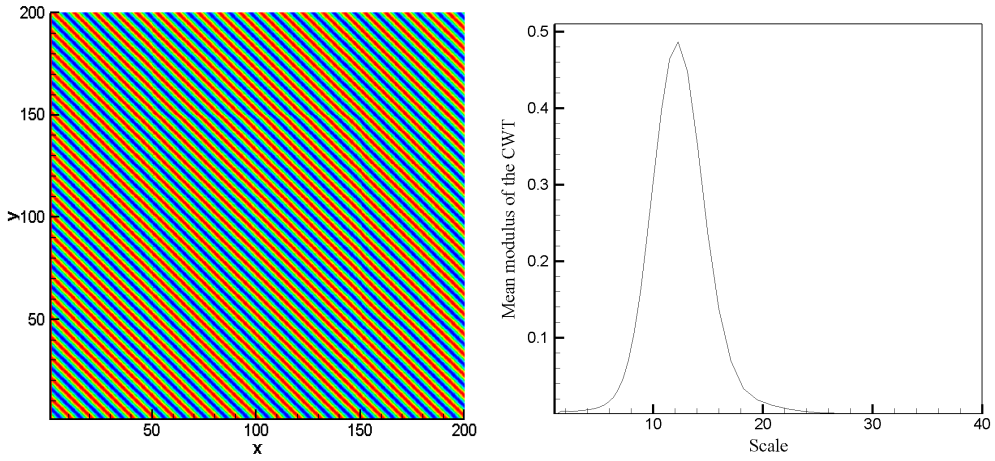

(a) (b)

Figure A.4: (a) A 2D spatial test signal composed of one wave number/length scale (b) Plane averaged modulus of the 2D Arc wavelet transform.

The simultaneous availability of scale and space information in the cube of data resulting from the application of the 2D CWT on the plane data is where the power of a wavelet based analysis resides. To further illustrate this point using the CARRÉ signal, Fig. A.6(a) shows a cut in the 3D cube of data at a specific x, y location along the scale axis. It serves to identify the local scale of resonance at one point on the $x - y$ plane. The cut clearly shows that resonance occurs at the expected scales in the quadrants designated as A and B in Fig. A.5. Another way of interrogating the cube of data is to identify the locations where certain scales dominate by making a cut at a specific scale and location along one direction and plot the distribution of the modulus of the transform along the other direction. Figure A.6(b) for example shows a cut at two different scales at $x = 50$ as a function of y. It clearly shows that the modulus peaks over the quadrant in which the specified scale exists and is nearly zero elsewhere.

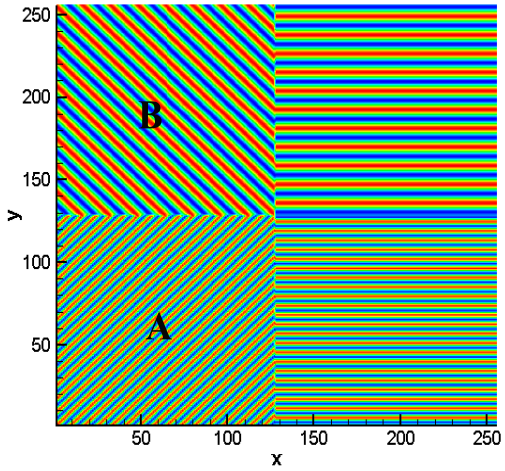

Figure A.5: CARRÉ test signal

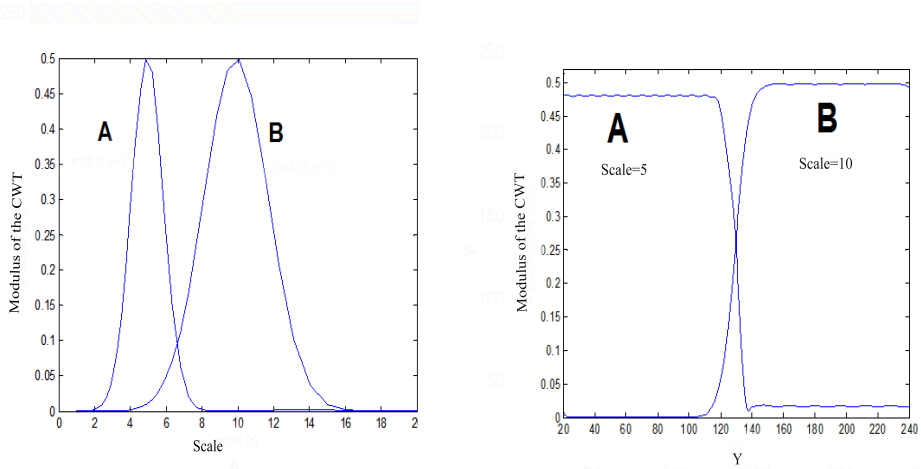

(a) (b)

Figure A.6: CARRÉ test signal: (a) Modulus of the 2D Arc wavelet transform at $x = 50, y = 50, 180$ (b) Modulus of the 2D Arc wavelet transform at $x = 50$ and $a = 5, 10$

If the data under analysis has a clearly visible mean direction with small deviations therefrom, *Morlet2D* offers better resolution capabilities than the non-directional Arc wavelet. In the absence of a dominant mean direction, a comprehensive search of resonance along multiple directions becomes a must. As an example of the use of *Morlet2D*, we once again analyze the same signal which we already analyzed using the Arc wavelet (Fig. A.4(a)). However, this time, we use the *Morlet2D* wavelet. We assume that the wave number orientation (45° in this case) is not known and, accordingly, perform the CWT at various interrogation angles. Maximum resonance (see Fig. A.7(b)) occurs at the the 45° interrogation angle which matches the orientation of the wave number. Note that the transform has angular symmetry about the wavelet direction (orientation of $\vec{\kappa_0}$) as evidenced by the identical distributions of the plane averaged modulus at the (60°, 30°) and (75°, 15°) seen in Fig. A.7(b).

Interrogations at other angles (not shown) showed that the angular selectivity (the change in interrogation angle that causes significant differences in the CWT's modulus) of the transform is on the order of 5°. As a result in situations where the signal is composed of many component wave numbers aligned along different unknown orientations and multiple interrogation angles are needed, then angle increments of 5° seem to be optimum. A final subtle point about *Morlet2D* is that the way it is defined (see equations 4.17, 4.18) is such that it possesses reflectional symmetry and hence is unable to differentiate between a wave number aligned at θ and $\theta + 180°$ (where $\theta \in [0, \pm 90°]$). In situations where wave numbers at θ and $\theta + 180°$ exist in clearly isolated regions of the *xy* plane then the signal can be analyzed by *Morlet2D* through alternately setting the signal's amplitude to zero over one region and interrogating the other. Finally, when a wave field is composed of arbitrary wave numbers aligned at

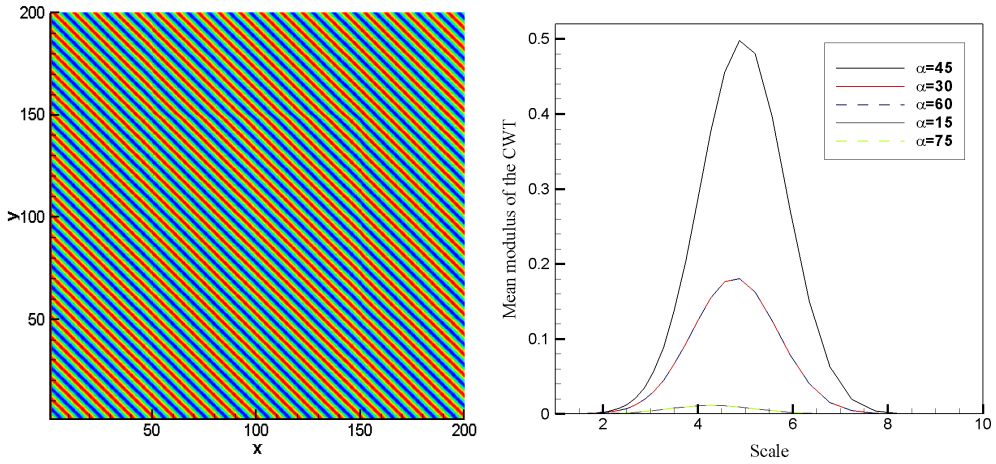

(a) (b)

Figure A.7: (a) A 2D spatial test signal composed of one wave number oriented at 45° to the *x* axis. (b) Plane averaged modulus of the *Morlet2D* wavelet transform at multiple interrogation angles

random orientations it becomes necessary to look for a statistical tool by which one can find the prevailing mean direction, if any, and a measure for the standard deviations relative to it. The hope is that by the use of *Morlet2D* wavelet at the prevailing mean direction one can capture the bulk of the energy of the signal and capitalize on its high resolution capabilities. Appendix B thus provides the necessary background material on directional data statistics.

APPENDIX B

DIRECTIONAL DATA STATISTICS

A separate branch of statistics that deal with directional data in such diverse fields as computer vision, robotics, biology, and geology is now well developed. Some of the most widely used methods of analyzing circular data in earth sciences are reviewed in the recent book by Trauth (2010).

The main problem which motivated the use of some of the concepts from directional/circular data analysis is the need to estimate the mean direction of a sample of resonance angles "recorded" at multiple spatial locations and to estimate a standard deviation from it. It turns out that a simple-minded arithmetic average of a collection of angles can lead to a largely erroneous mean angle. It can be simply explained on the basis of the wraparound at 360° or, simply put, the fact that 0°and 360° are identical angles. As an example consider the problem of finding the mean angle of 6° and 354°. It is clear that the arithmetic average 180° is not the true mean and that the standard deviation with respect to the mean is not 246°.

The solution to the mean direction problem is to treat the individual directions ϕ_i as the angle made by unit vectors with the horizontal and to use vector addition rules to sum them up and to finally divide by the number of directions N. Mathematically, this is equivalent to calculating the mean of the cosines and sines of each direction and to then obtain the mean angle $\overline{\phi}$ by calculating the inverse tangent that is

$$\overline{\phi} = \tan^{-1}(x_r/y_r), \tag{B.1}$$

where

$$x_r = \sum_{i=1}^{N} \sin(\phi_i), \tag{B.2}$$

and

$$y_r = \sum_{i=1}^{N} \cos(\phi_i). \tag{B.3}$$

The length of mean direction vector R is then

$$\overline{R} = \left(\sqrt{x_r^2 + y_r^2} \right) / N. \tag{B.4}$$

The more concentrated the angles are around the mean direction the larger the value of the mean direction vector (i.e. $\overline{R} \rightarrow 1$). Accordingly, one can define a measure for the dispersion around the mean as (Trauth, 2010)

$$\sigma_o = 1 - \overline{R}, \tag{B.5}$$

which is referred to as the "circular" variance.

The classic graphical representation of directional data is the rose diagram. A rose diagram is a histogram for a collection of measured angles. Whereas in a bar histogram, the heights of the bars are proportional to the frequency of the data contained within predefined bins, the rose diagram consists of segments of a circle with the radii of the sectors being proportional to the frequency of the data within the individual bins. We use Matlab's built-in Rose function to calculate and display the rose diagram of directional data. The function $ROSE(THETA, N_b)$ has two input arguments, namely the vector of measured angles $THETA$ and the number of bins N_b. Matlab then divides the 360° into N_b equally spaced bins, calculates the frequency of the data in each bin and displays the rose diagram. As an example to illustrate the basic utility of the circular statistics tools, we estimate a mean angle for the local resonance angles obtained through multiple interrogations ($\phi \in [0\ 90°]$ in 5° increments) of

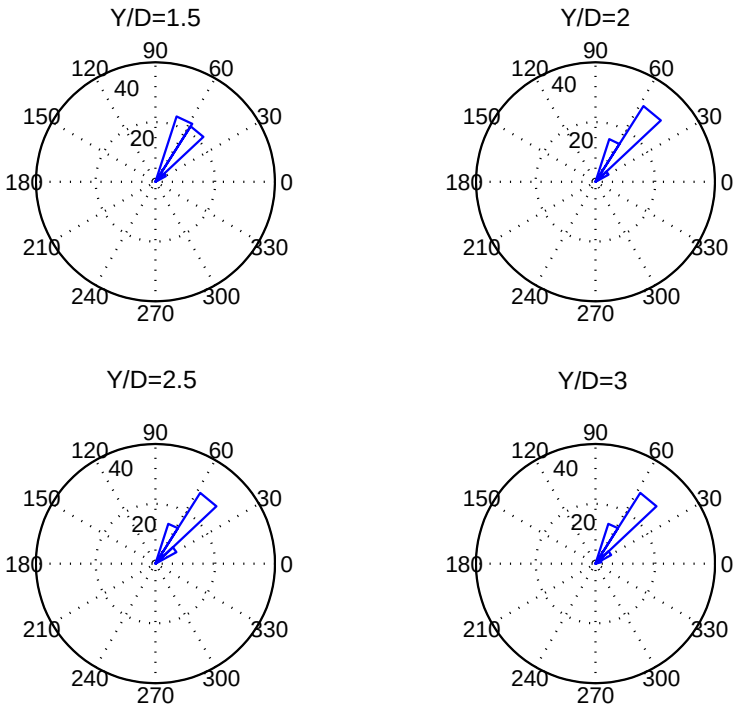

Figure B.1: Rose diagrams of resonance angles obtained at multiple span-wise locations y/D on the right half xy plane at $z/D = 1.5$ for the $R5Fr4$ simulation over $10 < Nt < 50$

the horizontal divergence field on a horizontal plane above the wake center line every $Nt = 1$ during the period of strong wave activity ($10 < Nt < 50$ for Re5kFr4 simulation at $z/D = 1.5$). Local resonance angles at multiple span-wise locations covering the approximate area through which the wake expands horizontally during its evolution ($y/D \in [1.5\ 3]$ for Re5kFr4 simulation) are stored in arrays and imported into an independent Matlab function that calculates the circular statistics and plots the rose diagram. Due to the symmetry of the wave radiation by the turbulent wake we only focus on one half plane. Differences between the statistics obtained from the two half planes are typically small ($O(5^\circ)$).

At every snapshot (i.e. $\Delta Nt = 1$), the local resonance angles along a given y/D location are sampled every $\Delta x/D = 1$ from the 3D cube of data resulting from the application of the *Morlet2D* transform to the 2D plane data. Only those resonance angles at x/D locations where the signal's amplitude (not the transform modulus) exceeds half the maximum global amplitude at the given y/D location are retained. This procedure acts to remove local resonance associated with weak wave packets. The mean directions of all resonance angles at the various y/D locations were in the range $[56^\circ - 65^\circ]$ with typical resultant vector magnitude $\overline{R} \sim 0.97$ and a circular variance $\sigma_o \sim 0.03$. We finally calculate a mean of the individual means obtained at the different y/D locations. In this particular case $\overline{\phi} \simeq 60^\circ$. The concentration of the resonance angles around 60° is clearly seen in Fig. B.1.

BIBLIOGRAPHY

ADDISON, P.S. 2002 *The illustrated wavelet transform handbook*. institute of Physics Publishing.

AGUADO, E. & BURT, J. E. 2003 *Understanding weather and climate*. Upper Saddle River, NJ.: Prentice Hall.

AGUILAR, DA & SUTHERLAND, BR 2006 Internal wave generation from rough topography. *Phys. Fluids* **18**, 066603.

AGUILAR, D.A., SUTHERLAND, B.R. & MURAKI, D.J. 2006 Laboratory generation of internal waves from sinusoidal topography. *Deep Sea Research Part II: Topical Studies in Oceanography* **53** (1-2), 96–115.

ANTOINE, J.P., MURENZI, R., VANDERGHEYNST, P. & ALI, S.T. 2004 *Two-dimensional wavelets and their relatives*. Cambridge Univ Pr.

APPLEBY, J. C. & CRIGHTON, D. G. 1987 Internal gravity waves generated by oscillations of a sphere. *J. Fluid Mech.* **183**, 439–450.

BAINES, P. G. 1995 *Topographic effects in stratified flows*. Cambridge,UK: University Press Monographs on Mechanics.

BONNET, J.P. & GLAUSER, M.N. 1994 Eddy structure identification in free turbulent shear flows. *Pure Appl. Geophys.* **143** (4), 779.

BONNETON, P., CHOMAZ, J.M. & HOPFINGER, E.J. 1993 Internal waves produced by the turbulent wake of a sphere moving horizontally in a stratified fluid. *J. Fluid Mech.* **254**, 23–40.

BOOKER, J.R. & BRETHERTON, F.P. 1967 The critical layer for internal gravity waves in a shear flow. *J. Fluid Mech.* **27** (03), 513–539.

BOYD, J. P. 2001 *Chebyshev and Fourier Spectral Methods*. Mineola, New York: Dover.

BRETHERTON, F.P. 1966 Gravity waves in shear. *Q.J.R. Met. Soc.* **92**, 466–480.

BROUTMAN, D., ROTTMAN, J. W. & ECKERT, S. D.. 2004 Ray methods for internal waves in the atmosphere and ocean. *Ann. Rev. Fluid Mech.* **36**, 233–253.

BROWAND, F. K., GUYOMAR, D. & YOON, S. C. 1987 The behaviour of a turbulent front in a stratified fluid: experiments with an oscillating grid. *J. Geophys. Res.* **92**, 5329–5341.

CAMPBELL, L. J. & MASLOW, S. A. 2003 Nonlinear critical-layer evolution of a forced gravity wave packet. *J. Fluid Mech.* **493**, 151–179.

CHASHECHKIN, Y.D. 1989 Hydrodynamics of a sphere in a stratified fluid. *Fluid Dynamics* **24** (1), 1–7.

CHOMAZ, J. M., BONETTON, P. & HOPFINGER, E. J. 1993 The structure of the near wake of a sphere moving in a stratified fluid. *J. Fluid Mech.* **254**, 1–21.

DALLARD, T. & BROWAND, F.K. 1993 The growth of large scales at defect sites in the plane mixing layer. *J. Fluid Mech.* **247**, 339–368.

DALLARD, T. & SPEDDING, G.R. 1993 2-D wavelet transforms: generalisation of the Hardy space and application to experimental studies. *EUR. J. MECH. B-FLUID* **12** (1), 107–134.

DALZIEL, S.B., HUGHES, G.O. & SUTHERLAND, B.R. 1998 Synthetic Schlieren. In *Proc. 8th Int. Symp. on Flow Visualization*. Citeseer.

DALZIEL, S.B., HUGHES, G.O. & SUTHERLAND, B.R. 2000 Whole-field density measurements by synthetic Schlieren. *Exp. Fluids* **28** (4), 322–335.

DAVIS, P. A. & PELTIER, W. R. 1979 Some characteristics of the Kelvin-Helmholtz and resonant overreflection modes of shear instability and of their interaction through vortex pairing. *J. Atmos. Sci.* **36**, 2394–2412.

DELISI, D.P. & ORLANSKI, I. 1975 On the role of density jumps in the reflexion and breaking of internal gravity waves. *J. Fluid Mech.* **69** (03), 445–464.

DIAMESSIS, P.J., DOMARADZKI, J.A. & HESTHAVEN, J.S. 2005 A spectral multidomain penalty method model for the simulation of high Reynolds number localized incompressible stratified turbulence. *J. Comp. Phys.* **202** (1), 298–322.

DIAMESSIS, P.J. & REDEKOPP, L.G. 2006 Numerical investigation of solitary internal wave-induced global instability in shallow water benthic boundary layers. *Journal of Physical Oceanography* **36**, 784–812.

DIAMESSIS, P. J., GURKA, R. & LIBERZON, A. 2010*a* Spatial characterization of vortical structures and internal waves in a stratified turbulent wake using proper orthogonal decomposition. *Phys. Fluids* **22**, 086601.

DIAMESSIS, P. J., SPEDDING, G.R. & DOMARADZKI, A. J. 2010*b* Similarity scaling and vorticity structure in high reynolds number stably stratified turbulent wakes. Accepted for publication in *J. Fluid Mech.*

DILLON, T.M. 1984 The energetics of overturning structures: Implications for the theory of fossil turbulence. *J. Phys. Oceanogr.* **14** (3), 541–549.

DOHAN, K. & SUTHERLAND, BR 2003 Internal waves generated from a turbulent mixed region. *Phys. Fluids* **15**, 488.

DOHAN, K. & SUTHERLAND, B. R. 2005 Numerical and laboratory generation of internal waves from turbulence. *Dyn. Atmos. Oceans* **40**, 43–56.

DOMMERMUTH, D.G., ROTTMAN, J.W., INNIS, G.E. & NOVIKOV, E.A. 2002 Numerical simulation of the wake of a towed sphere in a weakly stratified fluid. *J. Fluid Mech.* **473**, 83–101.

DOUGHERTY, J. 1961 The anisotropy of turbulence at the meteor level. *J. Atmos. Terrest. Phys* **21**, 210.

DRAZIN, PG 1977 On the instability of an internal gravity wave. *Proceedings of the Royal Society of London. Series A, Mathematical and Physical Sciences* pp. 411–432.

DURRAN, D.R. 1990 Mountain waves and downslope winds. *Meteorological Monographs* **23** (45), 59–81.

DURRAN, D.R. 1999 *Numerical methods for wave equations in geophysical fluid dynamics*. Springer Verlag.

ELIASSEN, A. & PALM, E. 1961 *On the transfer of energy in stationary mountain waves*. Geofysike Publikationer.

EMBID, P.F. & MAJDA, A.J. 1998 Low Froude number limiting dynamics for stably stratified flow with small or finite Rossby numbers. *Geophysical & Astrophysical Fluid Dynamics* **87** (1), 1–50.

FARGE, M. 1992 Wavelet transforms and their applications to turbulence. *Ann. Rev. Fluid Mech.* **24** (1), 395–458.

FINCHAM, A.M., MAXWORTHY, T. & SPEDDING, G.R. 1996 Energy dissipation and vortex structure in freely decaying, stratified grid turbulence. *Dynamics of Atmospheres and Oceans* **23** (1-4), 155–169.

FINNIGAN, J. J., EINAUDI, F. & FUA, D. 1984 The interaction between an internal gravity wave and turbulence in the stably-stratified nocturnal boundary layer. *J. Atmos. Science* **41**, 2409–2436.

FLYNN, M.R. & SUTHERLAND, B.R. 2004 Intrusive gravity currents and internal gravity wave generation in stratified fluid. *J. Fluid Mech.* **514**, 355–383.

FRITTS, D. C. 1982 The transient critical-level interaction in a Boussinesq fluid. *J. Geophys. Res.* **87**, 7997–8016.

GABOR, D. 1946 Theory of communication. *J. Inst. Elec. Eng.* **93** (III), 429–457.

GARRETT, C. & KUNZE, E. 2006 Internal tide generation in the deep ocean. *Ann. Rev. Fluid Mech.* **39** (1), 57.

GARRETT, C. & MUNK, W. 1972 Space-time scales of internal waves. *Geophysical & Astrophysical Fluid Dynamics* **3** (1), 225–264.

GARRETT, C. & MUNK, W. 1975 Space-time scales of internal waves: A progress report. *J. Geophys. Res.* **80**, 291–297.

GIBSON, C.H. 1980 Fossil temperature, salinity, and vorticity turbulence in the ocean. In *Marine turbulence: proceedings of the 11th International Liège Colloquium on Ocean Hydrodynamics*, p. 221. Elsevier Science & Technology.

GIBSON, C.H. 1982 Alternative interpretations for microstructure patches in the thermocline. *J. Phys. Oceanogr.* **12** (4), 374–383.

GIBSON, C.H. 1986 Internal waves, fossil turbulence, and composite ocean microstructure spectra. *J. Fluid Mech.* **168**, 89–117.

GIBSON, C. H., NABATOV, V. & OZMIDOV, R. 1993 Measurements of turbulence and fossil turbulence near Ampere seamount. *Dyn. Atmos. Oceans* **19**, 175–204.

GILREATH, H.E. & BRANDT, A. 1985 Experiments on the generation of internal waves in a stratified fluid. *AIAA J.* **23**, 693–700.

GOSTIAUX, L., DIDELLE, I, MERCIER, S. & DAUXOIS, T. 2007 A novel internal waves generator. *Experiments in Fluids* **58**, 123–130.

GOTTLIEB, D. & HESTHAVEN, J.S. 2001 Spectral methods for hyperbolic problems. *J. Comput. Appl. Math.* **128** (1-2), 83–131.

GOURLAY, M.J., ARENDT, S.C., FRITTS, D.C. & WERNE, J. 2001 Numerical modeling of initially turbulent wakes with net momentum. *Phys. Fluids* **13**, 3783.

GUERMOND, J.L. & SHEN, J. 2003 Velocity-correction projection methods for incompressible flows. *S.I.A.M. J. Numer. Anal.* **41** (1), 112–134.

GURLEY, K. & KAREEM, A. 1999 Applications of wavelet transforms in earthquake, wind and ocean engineering. *Engng. Structures* **21** (2), 149–167.

HESTHAVEN, J.S. 1997 A stable penalty method for the compressible Navier-Stokes equations. II: One-dimensional domain decomposition schemes. *S.I.A.M. J Sci. Comput.* **18** (3), 658–685.

HESTHAVEN, J.S. & GOTTLIEB, D. 1996 A Stable Penalty Method for the Compressible Navier–Stokes Equations: I. Open Boundary Conditions. *S.I.A.M. J Sci. Comput.* **17**, 579.

HOLTON, J.R., HAYNES, P.H., MCINTYRE, M.E., DOUGLAS, A.R., ROOD, R.B. & PFISTER, L. 1995 Stratosphere-troposphere exchange. *Reviews of Geophysics* **33** (4), 403–440.

HOPFINGER, E.J., FLOR, J.B., CHOMAZ, J.M. & BONNETON, P. 1991 Internal waves generated by a moving sphere and its wake in a stratified fluid. *Exp. Fluids* **11** (4), 255–261.

HURLEY, D. G. & KEADY, G. 1997 The generation of internal waves by vibrating elliptic cylinders. Part 2. Approximate viscous solution. *J. Fluid Mech.* **351**, 119–138.

ISRAELI, M. & ORSZAG, S.A. 1981 Approximation of radiation boundary conditions. *J. Comp. Phys.* **41** (1), 115–135.

ITSWEIRE, E.C., HELLAND, K.N. & VAN ATTA, C.W. 1986 The evolution of grid-generated turbulence in a stably stratified fluid. *J. Fluid Mech.* **162**, 299–338.

ITSWEIRE, E.C., KOSEFF, J.R., BRIGGS, D.A. & FERZIGER, J.H. 1993 Turbulence in stratified shear flows: Implications for interpreting shear-induced mixing in the ocean. *Journal of Physical Oceanography* **23** (7), 1508–1522.

JACOBITZ, F.G., ROGERS, M.M. & FERZIGER, J.H. 2002 Waves in turbulent stably-stratified shear flow. In *Proceedings of the Summer Program*, p. 257.

JAVAM, A., IMBERGER, J. & ARMFIELD, S. W. 2000 Numerical study of internal wave-caustic and internal wave-shear interactions in a stratified fluid. *J. Fluid Mech.* **415**, 89–116.

JAVAM, A. & REDEKOPP, L. G. 1998 The transmission of spatially-compact internal wave packets through a critical level. *Dyn. Atmos. Oceans* **28**, 127–138.

JONES, W.L. & HOUGHTON, D.D. 1971 The coupling of momentum between internal gravity waves and mean flow: A numerical study. *Journal of the Atmospheric Sciences* **28** (4), 604–608.

JONES, W. L. & HOUGHTON, D. D. 1972 The self-destructing internal gravity wave. *J. Atmos. Science* **29**, 844–849.

KARNIADAKIS, G.E., ISRAELI, M. & ORSZAG, S.A. 1991 High-order splitting methods for the incompressible Navier-Stokes equations. *J. Comp. Phys.* **97** (2), 414–443.

KEELER, R.N., BONDUR, V.G. & GIBSON, C.H. 2005 Optical satellite imagery detection of internal wave effects from a submerged turbulent outfall in the stratified ocean. *J. Geophys. Res.* **32**, 1–5.

KIYA, M. & ABE, Y. 1999 Turbulent elliptic wakes. *J. Fluids. Struct.* **13** (7-8), 1041–1067.

KLEMP, J.B. & LILLY, D.K. 1978 Numerical simulation of hydrostatic mountain waves. *J. Atmos. Sci.* **35** (1), 78–107.

KOOP, C.G. 1981 A preliminary investigation of the interaction of internal gravity waves with a steady shearing motion. *J. Fluid Mech.* **113**, 347–386.

KOOP, C.G. & MCGEE, B. 1986 Measurements of internal gravity waves in a continuously stratified shear flow. *J. Fluid Mech.* **172**, 453–480.

LELONG, M.P. & DUNKERTON, T.J. 1998 Inertia–gravity wave breaking in three dimensions. Part I: Convectively stable waves. *Journal of the atmospheric sciences* **55**, 2473–2488.

LI, H. & NOZAKI, T. 1995 Wavelet analysis for the plane turbulent jet (analysis of large eddy structure). *JSME Int. J. B.* **38** (4), 525–531.

LIGHTHILL, J. 1978 *Waves in fluids*. Cambridge Univ Pr.

LILLY, D.K., BASSETT, G., DROEGEMEIER, K. & BARTELLO, P. 1998 Stratified turbulence in the atmospheric mesoscales. *Theoretical and Computational Fluid Dynamics* **11** (3), 139–153.

LIN, C.-L., FERZIGER, J. K., KOSEFF, J. R. & MONISMITH, S. G. 1993 Simulation and stability of two-dimensional internal gravity waves in a stratified shear flow. *Dyn. Atmos. Oceans* **94**, 325–366.

LIN, J.T. & PAO, Y.H. 1979 Wakes in stratified fluids. *Annual Review of Fluid Mechanics* **11**, 317–338.

LIN, Q., LINDBERG, W.R., BOYER, D.L. & FERNANDO, H.J.S. 1992 Stratified flow past a sphere. *J. Fluid Mech.* **240**, 315–354.

LINDEN, P. F. 1975 The deepening of a mixed layer in a stratified fluid. *J. Fluid Mech.* **71** (02), 385–405.

LOMBARD, P.N. & RILEY, J.J. 1996 On the breakdown into turbulence of propagating internal waves. *Dynamics of Atmospheres and Oceans* **23** (1-4), 345–355.

LONG, S.R., LAI, R.J., HUANG, N.E. & SPEDDING, G.R. 1993 Blocking and trapping of waves in an inhomogeneous flow. *Dyn. Atmos. Oceans* **20** (1-2), 79–106.

LUMLEY, J.L. 1964 The spectrum of nearly inertial turbulence in a stably stratified fluid. *J. Atmos. Sci.* **21**, 99–102.

MAXWORTHY, T. 1980 On the formation of nonlinear internal waves from the gravitational collapse of mixed regions in two and three dimensions. *Journal of Fluid Mechanics* **96** (01), 47–64.

MENEVEAU, C. 1991 Analysis of turbulence in the orthonormal wavelet representation. *J. Fluid Mech.* **232**, 469–520.

MEUNIER, P., DIAMESSIS, P.J. & SPEDDING, G.R. 2006 Self-preservation in stratified momentum wakes. *Phys. Fluids* **18**, 106601.

MILES, J.W. 1971 Internal waves generated by a horizontally moving source. *Geophysical & Astrophysical Fluid Dynamics* **2** (1), 63–87.

MORLET, J. & GROSSMAN, A. 1984 Decomposition of Hardy functions into square integrable wavelets of constant shape. *S.I.A.M. J. Math. Anal.* **15**, 723–736.

MOUM, J.N., HEBERT, D., PAULSON, C.A. & CALDWELL, D.R. 1992 Turbulence and internal waves at the equator. Part I: Statistics from towed thermistors and a microstructure profiler. *J. Phys. Oceanogr.* **22** (11), 1330–1345.

MOWBRAY, D. E. & RARITY, B. S. H. 1967 A theoretical and experimental investigation of the phase configuration of internal waves of small amplitude in a density stratified liquid. *J. Fluid Mech.* **28**, 1–16.

MUNK, W. & WUNSCH, C. 1998 Abyssal recipes II: energetics of tidal and wind mixing. *Deep-Sea Research Part I* **45** (12), 1977–2010.

MUNROE, J.R. & SUTHERLAND, B.R. 2008 Generation of internal waves by sheared turbulence: experiments. *Environ. Fluid Mech.* **8** (5), 527–534.

ORLANSKI, I. & BRYAN, K. 1969 Formation of the thermocline step structure by large-amplitude internal gravity waves. *Journal of Geophysical Research* **74** (28), 6975–6983.

ORSZAG, S.A. & PAO, Y.H. 1974 Numerical computation of turbulent shear flows. *Adv. Geophys* **18**, 224–236.

OZMIDOV, R.V. 1965 On the turbulent exchange in a stably stratified ocean. *Izv. Acad. Sci. USSR, Atmos. Oceanic Phys* **1**, 853–860.

PAWLAK, G., MACCREADY, P., EDWARDS, K.A. & MCCABE, R. 2003 Observations on the evolution of tidal vorticity at a stratified deep water headland. *Geophys. Res. Lett.* **30** (24), Art. No. 2234.

PEACOCK, T., ECHEVERRI, P. & BALMFORTH, N. J. 2008 An experimental investigation of internal tide generation by two-dimensional topography. *J. Phys. Oceanogr.* **38** (1), 235–242.

PEAT, K.S. & STEVENSON, T.N. 1975 Internal waves around a body moving in a compressible density-stratified fluid. *J. Fluid Mech.* **70** (04), 673–688.

PHAM, H.T., SARKAR, S. & BRUCKER, K.A. 2009 Dynamics of a stratified shear layer above a region of uniform stratification. *J. Fluid Mech.* **630**, 191–223.

POPE, S. B. 2000 *Turbulent flows*. Cambridge,UK: Cambridge Univ Pr.

REYNOLDS, W. C. & HUSSAIN, A. K. M. F. 1972 The mechanics of an organized wave in turbulent shear flow. part 3. theoretical models and comparisons with experiments. *J. Fluid Mech.* **54**, 263–288.

RILEY, J.J. & LELONG, M.P. 2000 Fluid motions in the presence of strong stable stratification. *Annual review of fluid mechanics* **32** (1), 613–657.

RILEY, J.J., METCALFE, R.W. & WEISSMAN, M.A. 1981 Direct numerical simulations of homogeneous turbulence in density-stratified fluids. In *AIP Conference Proceedings*, , vol. 76, p. 79.

ROBEY, H.F. 1997 The generation of internal waves by a towed sphere and its wake in a thermocline. *Phys. Fluids* **9**, 3353.

ROTUNNO, R., GRUBISIC, V. & SMOLARKIEWICZ, P. K. 1999 Vorticity and potential vorticity in mountain wakes. *J. Atmos. Sci.* **56** (16), 2796–2810.

SCHOOLEY, A.H. & STEWART, R.W. 1963 Experiments with a self-propelled body submerged in a fluid with a vertical density gradient. *J. Fluid Mech.* **15** (01), 83–96.

SCINOCCA, J. F. & SHEPHERD, T. G. 1992 Nonlinear wave-activity conservation laws and hamiltonian structure for the two-dimensional anelastic equations. *J. Atmos. Science* **49**, 528.

SLINN, D. N. & RILEY, J. J. 1998*a* A model for the simulation of turbulent boundary layers in an incompressible stratified flow. *J. Comp. Phys.* **28**, 127–138.

SLINN, D. N. & RILEY, J. J 1998*b* Turbulent dynamics of a critically reflecting internal gravity wave. *Theor. Comput. Fluid Dyn.* **11**, 281–303.

SMYTH, W.D. & MOUM, J.N. 2000 Anisotropy of turbulence in stably stratified mixing layers. *Physics of Fluids* **12**, 1343.

SMYTH, W. D. & MOUM, J. N. 2001 *3D turbulence*. In *Encyclopedia of Ocean Sciences*. Academic Press.

SPEDDING, G.R. 2002*a* Vertical structure in stratified wakes with high initial Froude number. *J. Fluid Mech.* **454**, 71–112.

SPEDDING, G.R., BROWAND, F.K., BELL, R. & CHEN, J. 2000 Internal waves from intermediate, or late-wake vortices. In *Stratified Flows I - Fifth International Symposium* (ed. R. Pieters & N. Yonemitsu GA Lawrence), , vol. 1, pp. 113–118. University of British Columbia, Vancouver.

SPEDDING, G.R., BROWAND, F.K., HUANG, N.E. & LONG, S.R. 1993 A 2-D complex wavelet analysis of an unsteady wind-generated surface wave field. *Dyn. Atmos. Oceans* **20** (1-2), 55–77.

SPEDDING, G. R. 1997*a* The evolution of initially turbulent bluff-body wakes at high internal Froude number. *J. Fluid Mech.* **337**, 283–301.

SPEDDING, G. R. 1997*b* Vortex wakes in stably stratified fluids. In *Proceedings of the IUTAM Symposium on Simulation and Identification of Organized Structures in Flows*. Lyngby, Denmark: Kluwer.

SPEDDING, G. R. 2001 Anisotropy in turbulence profiles of stratified wakes. *Phys. Fluids* **13** (8), 2361–2372.

SPEDDING, G. R. 2002*b* The streamwise spacing of adjacent coherent vortices in stratified wakes. *Phys. Fluids* **14**, 3820–3828.

SPEDDING, G. R., BROWAND, F. K. & FINCHAM, A. M. 1996*a* The long-time evolution of the initially turbulent wake of a sphere in a stable stratification. *Dyn. Atmos. Oceans* **23**, 171–182.

SPEDDING, G. R., BROWAND, F. K. & FINCHAM, A. M. 1996*b* Turbulence, similarity scaling and vortex geometry in the wake of a towed sphere in a stably stratified fluid. *J. Fluid Mech.* **314**, 53–103.

STAQUET, C. 2005 Internal gravity waves in geophysical fluids. In *Environmental Stratified Flows* (ed. S. Sarkar & V. Armenio), , vol. 479, pp. 75–132. CISM, Udine: Springer.

SUTHERLAND, B.R., CAULFIELD, C.P. & PELTIER, W.R. 1994 Internal gravity wave generation and hydrodynamic instability. *J. Atmos. Sci.* **51** (22), 3261–3280.

SUTHERLAND, B.R., DALZIEL, S.B., HUGHES, G.O. & LINDEN, PF 99 Visualization and measurement of internal waves by synthetic Schlieren. Part 1. Vertically oscillating cylinder. *J. Fluid Mech.* **390**, 93–126.

SUTHERLAND, B.R. & LINDEN, P.F. 1998 Internal wave excitation from stratified flow over a thin barrier. *J. Fluid Mech.* **377**, 223–252.

SUTHERLAND, B. R. 1996 Internal gravity wave radiation into weakly stratified fluid. *Phys. Fluids* **8**, 430–441.

SUTHERLAND, B. R. 2001 Finite-amplitude internal wavepacket dispersion and breaking. *J. Fluid Mech.* **429**, 343–380.

SUTHERLAND, B. R. 2005 Internal wave propagation. In *Modern Applied Mathematics* (ed. J. C. Misra), pp. 372–422. New Delhi: Narosa Press.

SUTHERLAND, B. R. 2006*a* Internal wave instability: Wave-wave versus wave-induced mean flow interactions. *Phys. Fluids* **18**, 074107.

SUTHERLAND, B. R. 2006*b* Weakly nonlinear internal gravity wavepackets. *J. Fluid Mech.* **569**, 249–258.

TAYLOR, J.R. & SARKAR, S. 2007 Internal gravity waves generated by a turbulent bottom Ekman layer. *J. Fluid Mech.* **590**, 331–354.

TENNEKES, H. & LUMLEY, J. L. 1972 *A first course in turbulence*. The MIT press.

THORPE, SA 1981 An experimental study of critical layers. *J. Fluid Mech.* **103**, 321–344.

THORPE, S.A. 2005 *The turbulent ocean*. Cambridge Univ Pr.

THORPE, S. A. 2001 On the reflection of internal wave groups from sloping topography. *J. Phys. Oceanogr.* **31**, 3121–3126.

TOMCZAK, M. 1988 Island wakes in deep and shallow water. *J. Geophys. Res.* **93** (C5), 5153–5154.

TOWNSEND, A. A. 1959 Temperature fluctuations over a heated horizontal surface. *J. Fluid Mech.* **5** (02), 209–241.

TOWNSEND, A. A. 1965 Excitation of internal waves by a turbulent boundary layer. *J. Fluid Mech.* **22** (02), 241–252.

TOWNSEND, A. A. 1968 Excitation of internal waves in a stably-stratified atmosphere with considerable wind-shear. *J. Fluid Mech.* **32** (01), 145–171.

TRAUTH, M.H. 2010 *MATLAB® Recipes for Earth Sciences*. Springer.

TURNER, J.S. 1980 *Buoyancy effects in fluids*. Cambridge Univ Pr.

VOISIN, B. 1991 Internal wave generation in uniformly stratified fluids. Part 1. Green's function and point sources. *J. Fluid Mech.* **231**, 439–480.

VOISIN, B. 1994 Internal wave generation in uniformly stratified fluids. Part 2. Moving point sources. *J. Fluid Mech.* **261**, 333–374.

WIJESEKERA, H.W. & DILLON, T.M. 1991 Internal waves and mixing in the upper equatorial Pacific Ocean. *J. Geophys. Res.* **96** (C4), 7115–7125.

WINTERS, K. B. & D'ASARO, E. A. 1989 Two-dimensional instability of finite amplitude internal gravity wave packets near a critical level. *J. Geophys. Res.* **94**, 12709–12719.

WINTERS, K. B. & D'ASARO, E. A. 1994 Three-dimensional wave instability near a critical level. *J. Fluid Mech.* **272**, 255–284.

XUE-QUAN, E. & HOPFINGER, E.J. 1986 On mixing across an interface in stably stratified fluid. *J. Fluid Mech.* **166**, 227–244.

ZAVOL'SKII, N.A. & ZAITSEV, A.A. 1984 Development of internal waves generated by a concentrated pulse source in an infinite uniformly stratified fluid. *J. Appl. Mech. Tech.* **25** (6), 862–867.

ZIKANOV, O. & SLINN, D. N. 2001 Along-slope current generation by obliquely incident internal waves. *J. Fluid Mech.* **445**, 235–261.